

**STRUCTURAL, MAGNETIC,
OPTICAL AND ELECTRONIC
PROPERTIES OF TRANSITION
METAL COMPOUNDS AND
SEMICONDUCTORS**

**THESIS SUBMITTED FOR THE DEGREE OF
DOCTOR OF PHILOSOPHY (SCIENCE)**

IN

PHYSICS(THEORETICAL)

BY

SAIKAT DEBNATH

**DEPARTMENT OF PHYSICS
UNIVERSITY OF CALCUTTA**

APRIL, 2015

Acknowledgments

Working through my Ph. D. tenure has been a wonderful journey and it gives me immense pleasure to express my heartiest gratitude towards all the people who have made this journey possible. I met several people, developed skills, both academic and non-academic and now it is time to bid adieu from S. N. Bose Centre. First and foremost, I would like to thank my supervisor Prof. Priya Mahadevan for her continuous encouragement, motivation and support to carry out my thesis. This thesis would not have finished without your guidance and help. Your valuable suggestions, prompt comments and patience to correct my writing have been a great help. I always have admired your dedication, organization skills and the ability to pay attention to every student despite each of us working on diverse topics. I have learnt immensely from you which will surely help my future research career.

Working in a vibrant group like PMG (self explanatory) never let me feel that I was away from my home. Discussions, group presentations which used to start with me almost always, tea club discussions, evening walk, frequent dinner outing, all together kept me busy and I am really going to miss them. Ruma, Shishir and Basu, you trio were friend, philosopher, guide and partners in crime till the end of this journey. I am glad to have you in this journey. I would like to thank Bipul da for your help in the very early days at SNB. Never mentioned before, I used to try to keep my working folders as clean as you maintained but never achieved. Thanks to Abhinav da and Hirak da for those light moments (few years, to be precise) we spent together and Kapil for teaching, how to maintain the harmony between personal and professional life. How can I forget Ashis da? I can remember the night you waited for hours outside of your quarter to pick me up and your hospitality was beyond expectation. Thanks to Ravi also. Thanks to Poonam, Sagar, Jaydeep and Arka for being such obedient juniors.

Life at SNB was full of joyous moments and thanks to Ruma², Debashish, Surajit, Tilak, Dilip, Bipul, Santu, Rajasree, TG, Sing da, Jena da, Agarwal da, Rajib da, Rajiv da and Gola da for making it enjoyable, warm and complete. I would like to acknowledge the help I got from computer centre of SNB, especially from Mr. Abhijit Ghosh, Mr. Abhijit Roy, Mr. Sagar De, Mr. Sanjoy Choudhury and Mr. Bijoy Pramanik. This thesis would not have completed without the computing facility I got from PMG, ATHENA, AMRU, UNANST, HPC, CRAY, PHOTON and my very personal ENIACi7. I would acknowledge their support. Thanks to all academic, non-academic members and vigilant security guards of SNB. SNB mess, completely monitored by the active students should be acknowledge graciously.

I would like to acknowledge Dr. Marjana Lezaic and Dr. Ersoy Sasioglu for their guidance and help during my visit to Forschungszentrum Jülich GmbH.

CSIR is acknowledged for the scholarship which I got to carryout my research work.

I take the opportunity to express my gratitude to my affectionate parents. My father has always inspired me with his dedication and I have learnt patience from my mother. Their silent sacrifice and encouragement stimulated me to pursue an academic career. I show my respect to my elder brother for nurturing me to grow as what I am today. Last but not least, I would like to thank Payel formally, for being such wonderful and supportive beloved throughout this journey.

Saikat Debnath

S. N. Bose National Centre for Basic Sciences

April 2015

**Dedicated
To My Parents**

Contents

List of Figures	viii
List of Tables	xvi
1 Introduction	1
2 Methodology	18
2.1 Solution to Many Body Hamiltonian	18
2.2 Beyond Hartree-Fock: Density Functional Theory	23
2.2.1 The Kohn-Sham Equations	25
2.2.2 Exchange-Correlation Functional	26
2.2.3 Local Density Approximation (LDA)	27
2.2.4 Generalized Gradient Approximation (GGA)	28
2.2.5 Plane Wave Pseudopotential Method	29
2.2.6 Projector Augmented Wave (PAW) Method	32

2.2.7	Flow Chart of a DFT Calculation	33
2.3	Maximally Localized Wannier Function	34
3	The Role of Passivants on the Stoichiometry of CdSe and GaAs Nanocrystals	40
3.1	Introduction	40
3.2	Methodology	43
3.3	Results and Discussions	48
3.4	Conclusion	57
4	Optical Transition in Mn doped Semiconducting Nanocrystals	64
4.1	Introduction	64
4.2	Methodology	66
4.3	Results and Discussions	68
4.4	Conclusion	76
5	Ultrathin Films of CdS and the Polar Catastrophe Model	79
5.1	Introduction	79
5.2	Methodology	81
5.3	Results and Discussions	84
5.4	Conclusion	95

6	Orbital Ordering Driven Magnetism in Fe Intercalated TaS₂	99
6.1	Introduction	99
6.2	Methodology	101
6.3	Results and Discussions	103
6.4	Conclusion	113
7	Engineering Polar Distortion in SrTcO₃	118
7.1	Introduction	118
7.2	Methodology	121
7.3	Results and Discussions	122
7.4	Conclusion	133
8	Metallic Antiferromagnetic State in Electron Doped NaOsO₃	136
8.1	Introduction	136
8.2	Methodology	139
8.3	Results and Discussions	142
8.3.1	Electronic Structure Analysis	142
8.3.2	Magnetic Structure Analysis	148
8.4	Conclusion	154
	List of Publications	157

List of Figures

2.1	Flowchart of the DFT electronic structure calculation	34
2.2	Maximally localized Wannier function of one of the Fe dz^2 orbital in Fe intercalated TaS ₂	36
3.1	Structure generation procedure for non-stoichiometric and stoichiometric NCs of GaAs and CdSe. (a) Non-stoichiometric structures were generated by adding concentric layers of cations and anions. (b) Stoichiometric structures were generated by truncating spheres from supercell.	46
3.2	Different surfaces considered for the zinc blende structures. . .	47
3.3	Variation of the formation energy per atom for the passivated NCs of GaAs and CdSe as a function of volume for the non-stoichiometric and stoichiometric NCs under cation-rich (panels a and c) and anion-rich (panels b and d) conditions. Radii of two largest, relaxed NCs have been shown inside the panel a) and c). Ga and Se atom lie at the centre of GaAs and CdSe NCs respectively. The type of atom that forms the outermost layer in the case of the non-stoichiometric NCs has been indicated. This has appeared in Ref. 37.	49

3.4	Variation of the formation energy per atom for the unpassivated binary NCs of GaAs and CdSe as a function of volume for the non-stoichiometric and stoichiometric crystals under cation-rich (panel a and c) and anion-rich (panel b and d) conditions. Radii of two largest, relaxed NCs have been shown inside the panel a) and c). Ga and Se atom lie at the centre of GaAs and CdSe NCs respectively. The type of atom that forms the outermost layer in the case of the non-stoichiometric NCs has been indicated. This has appeared in Ref. 37.	51
3.5	(a) If the interaction strength between cation and passivant is stronger than the interaction strength between cation and anion, a cation rich surface is favoured. (b) Stronger interaction between cation and anion leads to an uncontrolled growth of NC.	52
3.6	The Se p projected partial density of states ($l=4$, non-stoichiometric and passivated NC) for a Se atom at (a) the core as well as at the surface having (b) double and (C) single coordination with Cd atoms. The zero of energy corresponds to the valence band maximum. This has appeared in Ref. 37.	54
3.7	The Cd s projected partial density of states ($l=5$, non-stoichiometric and passivated NC) for a Cd atom (a) in the first layer as well as at the surface having (b) triple, (c) double and (d) single coordination with the Se atoms. The zero of energy corresponds to the valence band maximum. This has appeared in Ref. 37.	55
4.1	Relaxed non-stoichiometric NC of $\text{MnZn}_{47}\text{Cd}_{48}\text{S}_{57}$	67

4.2	Hund's splitting and crystal field splitting in tetrahedral environment. d-d transition energy has been calculated from their values.	69
4.3	Density of states corresponding to Mn d states in Mn doped NC alloys. Two inequivalent cationic doping positions were chosen while constructing the structures.	70
4.4	Crystal structure of a representative unit cell of Mn doped CdS.	71
4.5	Spin and orbital projected density of states of Mn d and S p states in $\text{MnCd}_{31}\text{S}_{32}$	72
4.6	Bonding and anti-bonding levels coming from interaction between Mn d and S p.	73
4.7	Charge density plot within an energy window of 0.5 eV below the Fermi level shows the covalency between Mn d and S p states.	73
4.8	Spin and orbital projected density of states of Mn d and Se p states in $\text{MnCd}_{31}\text{Se}_{32}$	74
4.9	Optical transition energy in Mn doped (a)CdS and (b)Mn doped CdSe, calculated from the energy eigenvalues at the gamma point.	75
5.1	(a)Initial wurtzite fragment of the structure and the (b) planar structure after geometrical relaxations.	82

5.2	Two possible buckling configurations in the monolayer of CdS are shown. (a) In configuration 1, anions can be placed in the plane above, below and intermediate planes. (b) In configuration 2, anions can be placed in plane above and below only.	82
5.3	Phonon dispersion of planar monolayer of CdS. Mode softening through out the Brillouin zone signifies the dynamical instability of such structure. Resulting force acting on S ion, corresponding to M and K points are shown in the inset. . . .	85
5.4	(a) Buckled monolayer structure of CdS. Anions denoted by U and D are in the planes above and below respectively of the plane formed by Cd. Separation between U and D planes are shown separately. (b) Frustration in the buckled hexagonal structure is shown.	86
5.5	Phonon dispersion of planar monolayer of CdS under 2% biaxial strain. Structure is found to be dynamically stable from its phonon dispersion analysis.	88
5.6	Total energy comparisons between two different configurations. Configuration 2 is found to have lower energy near relevant region. Completely relaxed structure is found to have 6 meV/f.u. lower energy than the Configuration 2.	89
5.7	(a) Chiral bilayer and (b) Achiral bilayer of CdS.	91
5.8	Phonon dispersion of chiral bilayer of CdS. Removable phonon instability near gamma point is shown in the inset.	92

5.9	Band dispersion of chiral bilayer of CdS. Crystal field splitting at gamma point has fairly reduced from the monolayer limit but still higher than the bulk value.	93
5.10	Onsite energies of S p states referenced to the Cd s states determined from a fitting of the ab-initio band structure to a tight binding model.	94
5.11	Local electrostatic potential plot for different structures.	95
6.1	Different magnetic configurations of Fe intercalated TaS ₂ structures.	102
6.2	Crystal structure of Fe _{0.25} TaS ₂ . Separation between different atoms have been shown along with 2h block of TaS ₂ network.	103
6.3	Charge density close to the fermi level is confined within TaS ₂ layer. Significant contribution from Ta d and S p states is evident.	104
6.4	Charge density for the states close to 1.5 eV below the Fermi energy in the minority spin channel.	105
6.5	(a)Fe and (b)Ta d orbital projected density of states for ferromagnetic Fe _{0.25} TaS ₂ calculated for U=4 eV.	106
6.6	S p orbital projected density of states for ferromagnetic Fe _{0.25} TaS ₂ calculated for U=4 eV.	107
6.7	Two different doping sites for Fe _{0.25} TaS ₂	108
6.8	Fe d orbital projected partial density of states for AFM1 structure of Fe _{0.50} TaS ₂ calculated for U=4 eV on Fe. The Ta d _{z²} projected contribution is shown in the bottom most panel.	110

6.9	Bonding and antibonding levels originating from interaction between Fe d_z^2 and Ta d_z^2 at (a) low Fe doping and at (b) high Fe doping concentration.	110
6.10	(a) Fe d orbital projected partial density of states for $\text{Fe}_{0.25}\text{TaS}_2$ calculated for $U=2$ eV. (b) Onsite energies for Fe d_z^2 and Ta d_z^2 levels for $U=2$ eV and 4 eV.	112
7.1	Monolayer and bilayer heterostructures of $\text{SrTcO}_3/\text{BaTiO}_3$ have been generated from the bulk supercell of BaTiO_3 grown along the c direction	123
7.2	Spin and orbital projected DOS of Tc d states with t_{2g} symmetry in monolayer heterostructure of $\text{BaTiO}_3/\text{SrTcO}_3$	126
7.3	Spin and orbital projected DOS of Tc d states with t_{2g} symmetry in bulk structure.	126
7.4	Spin and orbital projected DOS of Tc d states with t_{2g} symmetry in bilayer heterostructure of $\text{BaTiO}_3/\text{SrTcO}_3$	130
7.5	Different hopping strengths in different directions lead to an AFE1 structure.	131
7.6	Different types of distortions in bilayer HS. Movement of Tc ions from the ideal position has been indicated with arrows.	132
8.1	Structure of $\text{Mg}_{0.25}\text{Na}_{0.75}\text{OsO}_3$	139
8.2	Different collinear AFM configurations.	140
8.3	Os d orbital and spin projected DOS in NaOsO_3 within ab initio calculation with $U= 1$ eV on Os.	143

8.4	Spin	polarized	
	atom projected partial DOS for $Mg_{0.028}Na_{0.972}OsO_3$ within		
	the ab initio calculation with $U=1$ eV on Os.		144
8.5	Variation of magnetic stabilization energy of G-AFM with dif-		
	ferent doping concentrations.		145
8.6	Os 5d orbital and spin projected DOS for $NaOsO_3$,		
	$Mg_{0.25}Na_{0.75}OsO_3$ and $Mg_{0.50}Na_{0.50}OsO_3$. Fermi energy has		
	been indicated with dashed line to clarify the rigid band shift		
	with doping.		146
8.7	Os 5d orbital and spin projected DOS for $Mg_{0.50}Na_{0.50}OsO_3$		
	in various antiferromagnetic configurations.		147
8.8	Spin wave dispersion of $NaOsO_3$, $Mg_{0.25}Na_{0.75}OsO_3$ and		
	$Mg_{0.50}Na_{0.50}OsO_3$		149
8.9	Spin wave dispersion of $NaOsO_3$ and results fitted with clas-		
	sical Heisenberg model.		150
8.10	(a) Neighbours corresponding to first four exchange interac-		
	tion terms. (b) Heisenberg exchange interaction parameters		
	of $NaOsO_3$ as a function of nearest neighbours.		151
8.11	(a) Spin wave dispersion of $Mg_{0.25}Na_{0.75}OsO_3$ and results fitted		
	with classical Heisenberg model. (b) Exchange interaction pa-		
	rameters of $Mg_{0.25}Na_{0.75}OsO_3$ as a function of nearest neighbours.		152
8.12	(a) Only AFM interaction possible in undoped $NaOsO_3$		
	whereas there are both FM and AFM component in (b) elec-		
	tron doped $NaOsO_3$		153

List of Tables

3.1	Approximate radii, number of atoms with different coordinations, and fraction of single and double coordinated atoms in A centered binary NCs of type A_mB_n as a function of the number of layers l	45
3.2	Formation energies corresponding to different passivated as well as unpassivated surfaces of CdSe.	54
3.3	Surface coordination numbers corresponding to atoms on different surfaces.	56
5.1	Polarization of two monolayers of ZnO and CdS corresponding to a fragment of the bulk wurtzite unit cell as well as the polarization for one monolayer of relaxed buckled CdS.	90
6.1	Relative energy of different magnetic configurations in meV as a function of Coulomb interaction strength for $Fe_{0.25}TaS_2$ as well as $Fe_{0.50}TaS_2$	112
7.1	Born effective charges of different atoms calculated for a cubic unit cell of $SrTcO_3$ as a function of volume.	124

7.2	Polar distortions in BaTiO ₃ /SrTcO ₃ heterostructure. Tc-O bond lengths along c direction have been tabulated for mono-layer as well as bilayer structure.	129
-----	---	-----

Chapter 1

Introduction

Ever since the invention of transistor [1, 2], semiconducting materials have become the work horse of modern day electronics. The range of electrical resistivity in these materials varies over orders of magnitude and the ability to tune them accordingly is key to any digital electronic device. Miniaturization and the constant effort to fit more number of transistors in smaller integrated circuits has led to the reduction in their physical dimension. This has led to the study of the physics of low dimension materials. At this low dimensional regime they behave very differently from the bulk limit and the strong dependence of physical properties on size has very significant technological implications. This coupled with the ease of fabrication and processing, makes this class of materials promising building blocks for materials with designed functionalities. For example, the band gap in CdS nanocrystals(NCs) can be tuned with the change of diameter only which is not possible in bulk. A change of diameter from 13 Å to 39 Å [3] results in a change of band gap from 4.5 eV to 2.5 eV respectively. This enormous tunability of physical properties has significant technological implications in the field of light emitting diodes(LED), switches, solar cells and other electronic devices. Light

emission in LED arises from the recombination of electrons and holes and the color of the light is solely dependent on the energy band gap of semiconductors. To mention some of the achievements, LED made from CdSe NCs can be tuned to emit light within red to yellow spectrum [4] with the variation of NCs diameter. White LED, based on ultra-small CdSe NCs [5] have shown excellent color characteristics. These advancements in the field of LED are sure to impact the existing lighting and display industry. Energy harvesting and the use of NCs for very efficient solar cells is another field of utmost interest. Overall energy conversion efficiency of traditional solar cells are very poor and strategic attempt to improve it [6] by channeling excess photon energy normally lost to heat into usable free energy have been made. This ability to control the properties in such NCs requires a competency to control the uniformity of size, shape, composition, crystal structure and surface stoichiometry and the knowledge of growth mechanism are of great importance.

While early studies on semiconducting NCs made use of particles embedded in glass matrices [7,8], they are now commonly grown as colloids suspended in solution. A typical synthesis to prepare NCs involves choosing molecular precursors, solvents and surfactants/passivating ligands using optimized reaction conditions causing the atoms to self-assemble into NCs [9]. Surfactants are introduced during the growth of NCs to arrest their growth leading to NCs of a desired size. While the main purpose of introducing these passivating ligands remains to control the growth of NCs but they have been found to influence the properties of resulting NCs as well. This emerges as a consequence of their binding with the surface atoms. Work by Nag et al. [10] has shown the way to thermodynamically stabilize both zincblende and wurtzite phase of CdS NCs. This was achieved by properly choosing passivating ligands which helps to fine tune the surface energy and thus pre-

ferring one type of geometry over the other. In another work, a novel route to the synthesis of CdSe NCs have been achieved [11] with the proper choice of passivating ligands. Optical transition in II-VI NCs have been tuned [12] with the help of surface functionalization. Moreover magnetism has been induced [13] in case of thiol capped gold NCs which arises because of the strong interaction between the surface atoms and the capping ligands. In **Chapter 3** considering the example of binary semiconductors CdSe and GaAs, we go onto investigate the role of passivants in controlling the stoichiometry of NCs. We find that the strong interaction between the passivants and surface atoms could result in the growth of highly non-stoichiometric NCs. This emerges from the fact that polar surfaces have more neighbours with the passivating ligands than non-polar surfaces. This leads to a stronger interaction between the passivants and the surface atoms which could dictate the surface stoichiometry.

With this understanding of the role of passivant on the growth mechanism of semiconducting NCs we went on to explore the route of doping to exploit optical properties of these nano materials. Doping is a well known route to introduce allowed energy states within the band gap region. Room temperature can thermally ionize the dopant states and thus creates free carriers in the conduction or valence bands. Dopants can also modify the band structure and thus can tune various properties of the host material. This idea has been carried forward for the case of semiconducting nano materials and constitutes one of the most active research fields of today. But unlike doping bulk semiconductors, many of the efforts of incorporating impurities in semiconducting NCs have failed due to the effect known as self-purification [14, 15] process. However the issue has been addressed with the help of binding energy associated with different morphological surfaces and a novel route of doping [15] has been proposed. Choice of dopant materials is another concern

as the properties of the doped semiconducting NCs often solely depend on the properties of the dopant energy levels. Transition metal ions with localized, magnetic and essentially atomic like character are often the first choice as they offer a wide range of properties to be tuned. Considering the example of Co doped CdSe NCs, experimentalists have observed [16] an enhancement of magnetic super-exchange between Co^{+2} dopant ions in the confined system. Interaction between the magnetic ion and the exciton in Mn doped CdTe NCs have been exploited [17,18] to manipulate the quantum state of an individual spin by optical or electrical polarized carriers. Thus information can be written on the spin state of a single Mn ion in a semiconducting NCs using an orientation process. Another aspect which has drawn huge interest is the extraordinarily bright photoluminescence shown by these doped NCs. Mn doped semiconducting NCs are admittedly the foremost system that has been explored so far. Mn d states are usually found to be unaffected by the size of the host NCs and wide range of tunability of the emission that one requires for the technological applications are very limited [19,20]. But recent spatially resolved optical emission results by Hazarika et. al. [21] have suggested that the energy levels of each manganese ion are influenced by the surrounding environment. Mn ions residing near the surface experience more distorted ligand field compared to those residing near the core of the NC. Thus any emission from Mn ions doped near the center differs from ions near the surface of the nano-particles and one can attain wide emission spectrum by doping at various inequivalent sites in the host. Despite this, one finds that a transition between Mn levels is invariant from the core of the NCs and does not depend on the host, suggestive of a strongly atomic character of the transition. In **Chapter 4**, considering the case of Mn doping in semiconducting NCs we have shown that optical transition from the core of NCs is independent of their local environment. Analysis of the density

of states(DOS) coming from Mn and nearby host anionic sites reveal that there are substantial interaction between them. However the interactions are normalized in such a way that the relative position of the effective transition levels remain fixed leading to very atomic like transition energy.

The successful exfoliation of graphene [22] has propelled the growth of semi-conducting physics, especially the area of two dimensional layered materials. Properties like quantum Hall effect [23], presence of mass-less Dirac fermions [24,25], very high electrical [26] and thermal conductivity [27], optical transparency [28,29] and remarkably strong surface, have made graphene the most studied two dimensional material. But being a zero band gap material, it is not suitable for controlling the electrical conductivity. Band gap can be opened in the patterned [30] as well as bilayer structures [31] but at a cost of a huge reduction in electron mobility [32]. The constant endeavour of tuning the electrical conductivity, optical properties, mechanical stability etc. has driven the discovery of other layered materials like molybdenum disulfide (MoS_2). MoS_2 is a transition metal dichalcogenide which forms bulk crystals of two-dimensional layers stacked in the vertical direction. This is very similar in form to graphene and express diverse electronic and optical properties that differs from those in bulk. Bulk MoS_2 is an indirect bandgap material with a band gap of 1.2 eV whereas monolayer of MoS_2 is a direct band gap material with an enhanced intrinsic band gap of 1.8 eV [33]. Being a direct band gap material it can couple optical and electrical properties [34] which is not possible with silicon in a single transducer. Moreover heterostructures of these materials have already shown to couple different degrees of freedom. As an example heterostructures of graphene and MoS_2 has already been explored [35] as a multifunctional photo-responsive memory devices. Hexagonal BN (h-BN) is another member of this group and is the best known substrate for graphene based system for its very sim-

ilar lattice constant and atomically smooth surface. It is a layered material with weak van der Waals interaction between the layers. Bandgap is found to be 5.97 eV [36] and thus have a potential application as deep ultraviolet light emitter. Fabrication of two dimensional monolayer of h-BN through the controlled energetic electron irradiation [37] and chemical vapour deposition on Cu foil [38] has already been achieved. To date, experiments have not successfully measured the opto-electronic properties but due to the broken symmetry of the sublattice it is expected to be insulating and could also be another potentially important material for novel electronic device fabrication. Epitaxially grown Ge films on Si substrates have been found to be another important material for Ge-on-Si microelectronics [39] due to high carrier mobility. Ge-on-Si is a promising building block for a variety of applications for Si based photonic systems [40]. Moreover a general route to grow epitaxial layer of two dimensional nano materials on top of layered hybrid perovskite has been proposed [41] which has opened a new playground for modern quantum device fabrication. With the advent of scientific progress and control to the experimental precision this list is getting populated very quickly and monolayer zinc oxide(ZnO) is one new member of this group. It has been shown considering the example of ZnO that thinner films with wurtzite structure while grown along (0001) direction remove the electric polarization by adopting a graphitic like structure [42,43] in which the atoms are in threefold coordination. The question in **Chapter 5** we ask is up to what thickness are polar structures stabilized in covalent semiconductors such as CdS. Using experimental in-plane lattice constant, we find that a buckled structure with a finite dipole moment is favoured at the monolayer limit. This is because the Coulomb interactions between the electrons on Cd and S atoms are large in the graphitic phase. The system overcomes this by buckling and elongating the Cd-S bonds. Alternately a 2% biaxial tensile

strain is found to stabilize a rare graphitic phase in one monolayer of CdS. In the bilayer limit a more three dimensional non-polar chiral structure is found to be favoured in the absence of any strain. Thus though one can have slightly polar structures in the monolayer limit of CdS, the dipole moment is found to build up with thickness forcing non polar structures to be the norm.

Abundant availability of transition metal compounds with magnetic properties inspired our scientific endeavor from the dawn of the society. One of the first references to the spontaneous magnetic properties of lodestone [44] which is nothing but oxide of iron, was made around 6th century B.C. Intense experimental as well as theoretical research has explored properties like high temperature superconductivity [45, 46], charge [47–49], orbital [50, 51] and spin ordering [49, 50], multiferroic properties [52–54], metal insulator transition [55, 56], ability to form complex oxides etc. apart from magnetism [57, 58]. Thus, when recent research showed that in addition to the composition and arrangement of atoms in materials, dimensionality also plays a crucial role in determining fundamental properties [22], transition metal compounds [59] become one obvious choice for exploring. In **Chapter 6** we considered one less-investigated interesting layered transition metal compound, TaS₂. It is metallic and non-magnetic in nature. Fe intercalation in this material introduces very diverse magnetic properties and one has both ferromagnetic(FM) as well as anti-ferromagnetic(AFM) structures depending on the doping concentration [60, 61]. Additionally one finds a very large magneto-crystalline anisotropy associated with Fe_{0.25}TaS₂ [62], which makes it useful for switching applications. These layered magnetic materials could be a cheap alternative to magnetic layered heterostructures. While an RKKY model has earlier been used [63] to explain the observed magnetism, analogous to the well studied problem of nonmagnetic metal-magnetic metal

heterostructures, in the present system we find strong interaction between Fe dz^2 states and the Ta dz^2 states. At low concentrations the pathway for electrons on Fe to hop through Ta results in a FM alignment of Fe spins. Fe also donates electrons to the system, behaving like a +2 entity. With increasing Fe concentration, the Ta dz^2 states get filled up, removing the FM channel. Additionally the in plane Fe atoms come closer resulting in anti-ferromagnetism being favoured.

Multiferroic materials [64] with spontaneous magnetization and polarization is another promising candidate for advanced devices. However the fact that long range magnetic order requires finite d count with localized electrons but experimental evidences show that large ferroelectric polarizations are primarily found in d^0 systems, is responsible for the scarcity of such multiferroic materials [65,66]. There are examples of multiferroic materials but the electric polarization associated with such structures are way smaller than found in ferroelectric materials($0.17 \mu C/cm^2$ in $LuMnO_3$ [67] compared to $26 \mu C/cm^2$ in $BaTiO_3$ [68]). One proposed route to achieve multiferroic material was to search for perovskites in which magnetism and ferroelectricity are driven independently by the different cationic sites [69,70]. However the significance of coupling two different degrees of freedom is lost in such mechanism. Recently band insulators have been explored as potential multiferroic materials [71]. The reason being that first order Jahn-Teller distortions are quenched as a result of absence of any orbital degeneracy. Consequently, the lowest order distortions are second order in nature which are usually found to be polar. In **Chapter 7** we consider the example of a recently synthesized high Neel temperature material, $SrTcO_3$ [72,73]. We find it to have significantly enhanced Born effective charge at the O and Tc sites, though no polar distortion is found to be favoured at the bulk limit. Introducing two monolayers of $SrTcO_3$ between $BaTiO_3$, a ferroelectric material, we find that

polar distortions are stabilized in the SrTcO₃ layer. The substrate merely provides the required strain. This is verified by subjecting the substrate to an additional 2% biaxial strain where we find that while the substrate loses its ferroelectricity, the SrTcO₃ layer has its ferroic distortions. We then ask about the microscopic considerations which allow polar distortions to be stabilized. Within our calculations we have explored the role of quantum confinement, Born-effective charge and breaking of the inversion symmetry to stabilize the polar distortions in such heterostructure. Adding another TcO₂ layer results in the distortions in the two TcO₂ layers to be out of phase. Our analysis shows that there is an asymmetry associated with the hopping strength along two opposite out-of-plane directions. While the movement of Tc ion in one direction results in a gain in total energy, there is loss in energy while the movement is in opposite direction. This mechanism has been shown to explain the polar distortions in such structure.

Band model was simple and successful to describe insulating and metallic state in most of the materials. So, it was a surprise when the report of de Boer and Verwey [74] showed the presence of several insulating transition metal oxides such as NiO, with partially filled d electrons which were expected to be metallic according to the band model. It was the first instance when the band model failed and the importance of other effects have been since realized. Mott and Peierls [75] came up with the idea that strong Coulomb repulsion between electrons could be responsible for such insulating materials and paved the path for widely studied metal insulator transition(MIT) for strongly correlated materials. The properties of the MIT, so far, have been most extensively studied for d-electron systems [56] and transition metal compounds especially perovskite oxides have been the preferred choice always. Insulator driven by correlation effects in these materials is categorized as Mott insulators [55] or charge transfer insulators [76] and the Hubbard

model [77] and its extended form are often used to describe the MIT in such materials. Within the Hubbard model, MIT can be understood as a competition between the localizing and the delocalizing effects and a material becomes insulating when the localizing effect surpasses the delocalizing effect. This description can also detail the presence of several 3d insulating transition metal compounds and the scarcity of such materials in the 4d or 5d series. There is another type of MIT driven by magnetic correlation effects and is operative at the magnetic transition temperature. Slater successfully addressed the issue [78] with the argument that anti-ferromagnetic (AFM) order with neighboring spin oppositely aligned, occurs at the MIT temperature. This creates an opposite periodic potential on each nearest neighbour which results in an energy gap in the modified magnetic Brillouin zone. Despite this, there was no experimental evidence until recently magnetically driven MIT have been observed in 5d transition metal compound NaOsO_3 [79]. AFM order driven by the nesting of the Fermi surface plays an important role in gap opening in these materials and should be strictly operative at the half filling of the band. In **Chapter 8** we have asked the question about the scenario beyond half filling. With the slightest amount of electron doping in the half filled band we are able to stabilize a structure which is metallic and AFM in nature. AFM order in this material is found to be more robust than expected and we are able to stabilize AFM metallic state even at 50% doping concentration. We further have analyzed magnetism in the parent and the doped structures with the help of Heisenberg model and contributions from different superexchange pathways have been discussed.

Bibliography

- [1] APS News This month in Physics History, November 17-December 23, 1947: Invention of the First Transistor, www.aps.org/publications/apsnews/200011/history.cfm
- [2] John Bardeen, William Shockley, Walter Brattain, Invention of the Transistor-Bell Laboratories, <http://bit.ly/1argCJX>.
- [3] T. Vossmeier , L. Katsikas , M. Giersig , I. G. Popovic , K. Diesner , A. Chemseddine , A. Eychmueller and H. Weller, *J. Phys. Chem.*,**98**, 7665 (1994).
- [4] V. L. Colvin, M. C. Schlamp and A. P. Alivisatos, *Nature*, **370**, 354 (1994).
- [5] M. A. Schreuder, K. Xiao, I. N. Ivanov, S. M. Weiss and S. J. Rosenthal, *Nano Lett.*, **10**, 573 (2010).
- [6] M. C. Hanna1 and A. J. Nozik, *J. Appl. Phys.*, **100**, 074510 (2006).
- [7] N. F. Borrelli, D.W. Hall, H. J. Holland, D. W. Smith, *J. Appl. Phys.*, **61**, 5398 (1987).
- [8] J. Warnock and D. D. Awschalom, *Phys. Rev. B*, **32**, 5529 (1985).
- [9] Y. Yin and A. P. Alivisatos, *Nature*, **437**, 664 (2005).

- [10] A. Nag, A. Hazarika, K. V. Shanavas, S. M. Sharma, I. Dasgupta and D. D. Sarma, *J. Phys. Chem. Lett.*, **2**, 706 (2011).
- [11] J. Jasieniak, C. Bullen, J. van Embden, P. Mulvaney, *J. Phys. Chem. B*, **109**, 20665 (2005).
- [12] O. Chen, Y. Yang, T. Wang, H. Wu, C. Niu, J. Yang and Y. C. Cao, *J. Am. Chem. Soc.*, **133**, 17504 (2011).
- [13] P. Crespo, R. Litran, T. Rojas, M. Multigner, J. De la Fuente, J. Sanchez-Lopez, M. Garcia, A. Hernando, S. Penades, A. Fernandez, *Phys. Rev. Lett.*, **93**, 87204 (2004).
- [14] G. M. Dalpian and J. R. Chelikowsky, *Phys. Rev. Lett.*, **96**, 226802 (2006).
- [15] S. C. Erwin, L. Zu, M. I. Haftel, A. L. Efros, T. A. Kennedy and D. J. Norris, *Nature*, **436**, 91 (2005).
- [16] K. M. Hanif, R. W. Meulenberg and G. F. Strouse, *J. Am. Chem. Soc.*, **124**, 11495 (2002).
- [17] L. Besombes, Y. Leger, L. Maingault, D. Ferrand and H. Mariette, *Phys. Rev. Lett.*, **93**, 207403 (2004).
- [18] M. Goryca, T. Kazimierzuk, M. Nawrocki, A. Golnik, J.A. Gaj and P. Kossack, *Phys. Rev. Lett.*, **103**, 087401 (2009).
- [19] N. Pradhan and X. Peng, *J. Am. Chem. Soc.*, **129**, 3339 (2007).
- [20] R. Zeng, T. Zhang, G. Dai and B. Zou, *J. Phys. Chem. C*, **115**, 3005 (2011).
- [21] A. Hazarika, A. Layek, S. De, A. Nag, S. Debnath, P. Mahadevan, A. Chowdhury and D.D. Sarma, *Phys. Rev. Lett.*, **110**, 267401 (2013). 1,

- [22] K. S. Novoselov, A. K. Geim, S. V. Morozov, D. Jiang, Y. Zhang, S. V. Dubonos, I. V. Grigorieva, A. A. Firsov, *Science*, **306**, 666 (2004).
- [23] Yuanbo Zhang, Yan-Wen Tan, Horst L. Stormer and Philip Kim, *Nature*, **438**, 201 (2005).
- [24] K. S. Novoselov, A. K. Geim, S. V. Morozov, D. Jiang, M. I. Katsnelson, I. V. Grigorieva, S. V. Dubonos and A. A. Firsov, *Nature*, **438**, 197 (2005).
- [25] Xu Du, Ivan Skachko, Fabian Duerr, Adina Luican and Eva Y. Andrei, *Nature*, **462**, 192 (2009).
- [26] K.I. Bolotin, K.J. Sikes, Z. Jiang, M. Klima, G. Fudenberg, J. Hone, P. Kim and H.L. Stormer, *Solid State Commun.*, **146**, 351 (2008).
- [27] A. A. Balandin, S. Ghosh, W. Bao, I. Calizo, D. Teweldebrhan, F. Miao and C. N. Lau, *Nano Lett.*, **8**, 902 (2008).
- [28] A. B. Kuzmenko, E. van Heumen, F. Carbone, and D. van der Marel, *Phys. Rev. Lett.*, **100**, 117401 (2008).
- [29] D. E. Sheehy and J. Schmalian, *Phys. Rev. B*, **80**, 193411 (2009).
- [30] M. Y. Han, B. Ozyilmaz, Y. Zhang and P. Kim, *Phys. Rev. Lett.*, **98**, 206805 (2007).
- [31] Y. Zhang, Tsung-Ta Tang, C. Girit, Z. Hao, M. C. Martin, A. Zettl, M. F. Crommie, Y. R. Shen and F. Wang, *Nature*, **459**, 820 (2009).
- [32] M. Y. Han, B. Ozyilmaz, Y. Zhang and P. Kim, *Phys. Rev. Lett.*, **98**, 206805 (2007).
- [33] K. F. Mak, C. Lee, J. Hone, J. Shan and T. F. Heinz, *Phys. Rev. Lett.*, **105**, 136805 (2010).

- [34] O. Lopez-Sanchez, D. Lembke, M. Kayci, A. Radenovic and A. Kis, Nature Nanotech., **8**, 497 (2013).
- [35] K. Roy, M. Padmanabhan, S. Goswami, T. P. Sai, G. Ramalingam, S. Raghavan and A. Ghosh, Nature Nanotech., **8**, 826 (2013).
- [36] Y. Kubota, K. Watanabe, O. Tsuda, T. Taniguchi, Science, **317**, 932 (2007).
- [37] C. Jin, F. Lin, K. Suenaga and S. Iijima, Phys. Rev. Lett., **109**, 195505 (2009).
- [38] K. K. Kim, A. Hsu, X. Jia, S. M. Kim, Y. Shi, M. Hofmann, D. Nezich, J. F. Rodriguez-Nieva, M. Dresselhaus, T. Palacios and J. Kong, Nano Lett., **12**, 161 (2011).
- [39] M. L. Lee, E. A. Fitzgerald, M. T. Bulsara, M. T. Currie and A. Lochtefeld, J. Appl. Phys., **97**, 011101 (2005).
- [40] R. Soref, Nature Photonics, **4**, 495 (2010).
- [41] Hai-Xin Lin, L. Chen, De-Yu Liu, Zhi-Chao Lei, Y. Wang, Xiao-Shan Zheng, B. Ren, Zhao-Xiong Xie, G. D. Stucky and Zhong-Qun Tian, J. Am. Chem. Soc., **137**, 2828 (2015).
- [42] C. L. Freeman, F. Claeysens and N. L. Allan, Phys. Rev. Lett., **96**, 066102 (2006).
- [43] C. Tusche, H. L. Meyerheim and J. Kirschne, Phys. Rev. Lett., **99**, 026102 (2007).
- [44] Hurlbut, C. Searle, W. E. Sharp, E. S. Dana, Dana's minerals and how to study them. John Wiley and Sons. 96 (1998).

- [45] J. G. Bednorz and K. A. Muller, <http://bit.ly/1IZFhRx>.
- [46] E. Dagotto, *Rev. Mod. Phys.*, **66**, 763 (1994).
- [47] E. J. W. Verway, *Nature*, **144**, 327 (1939).
- [48] Y. Tomioka, T. Okuda, Y. Okimoto, A. Asamitsu, H. Kuwahara and Y. Tokura, *Journal of Alloys and Compounds*, **326**, 27 (2001).
- [49] C. N. R. Rao, *J. Phys. Chem. B*, **104**, 5877 (2000).
- [50] T. Mizokawa and A. Fujimori, *Phys. Rev. B*, **56**, 493R (1997).
- [51] T. Hotta, *Reports on Progress in Physics*, **69**, 2061 (2006).
- [52] S. Dong and Jun-Ming Liu, *Mod. Phys. Lett. B*, **26**, 1230004 (2012).
- [53] Y. Tokunaga, N. Furukawa, H. Sakai, Y. Taguchi, Taka-hisa Arima and Y. Tokura, *Nature Mat.*, **8**, 558 (2009).
- [54] I. A. Sergienko and E. Dagotto, *Phys. Rev. B*, **73**, 094434 (2006).
- [55] N. F. Mott, *Rev. Mod. Phys.*, **40**, 677 (1968).
- [56] M. Imada, A. Fujimori and Y. Tokura, *Rev. Mod. Phys.*, **70**, 1039, (1998).
- [57] K. Yosida, *Theory of Magnetism*, Springer-Verlag (1998).
- [58] D. C. Jiles, *Introduction to Magnetism and Magnetic Materials*, Routledge Chapman and Hall (1998).
- [59] S. J. Moon, H. Jin, K. W. Kim, W. S. Choi, Y. S. Lee, J. Yu, G. Cao, A. Sumi, H. Funakubo, C. Bernhard and T. W. Noh, *Phys. Rev. Lett.*, **101**, 226402 (2008).

- [60] M. Eibshutz, S. Mahajan, F. J. DiSalvo, G. W. Hull, and J. V. Waszczak, *J. Appl. Phys.* **52**, 2098 (1981).
- [61] H. Narita, H. Ikuta, H. Hinode, T. Uchida, T. Ohtani, and M. Wakihara, *J. Solid State Chem.* **108**, 148 (1994).
- [62] Y. J. Choi, S. B. Kim, T. Asada, S. Park, Weida Wu, Y. Horibe, and S-W. Cheong, *EPL* **86**, 37012 (2009).
- [63] K. T. Ko, Kyoo Kim, Sung Baek Kim, H. D. Kim, J. Y. Kim, B. I. Min, J.H. Park, F.H. Chang, H. J. Lin, A. Tanaka, and S. W. Cheong, *Phys. Rev. Lett.* **107**, 247201 (2011).
- [64] H. Schmid, *Ferroelectrics*, **162**, 317 (1994).
- [65] A. Filippetti and N. A. Hill, *Phys. Rev. B*, **65**, 195120 (2002).
- [66] N. A. Hill, *J. Phys. Chem. B*, **104**, 6694 (2000).
- [67] Y. S. Chai, Y. S. Oh, L. J. Wang, N. Manivannan, S. M. Feng, Y. S. Yang, L. Q. Yan, C. Q. Jin and Kee Hoon Kim, *Phys. Rev. B*, **85**, 184406 (2012).
- [68] H. H. Wieder, *Phys. Rev. B*, **99**, 1161 (1955).
- [69] R. Ramesh and N. A. Spaldin, *Nature Materials*, **6**, 21 (2007).
- [70] D. I. Khomskii and G. A. Sawatzky, *Solid State Commun.*, **102**, 87 (1997).
- [71] S. Bhattacharjee, E. Bousquet and Philippe Ghosez, *Phys. Rev. Lett.*, **102**, 117602 (2009).
- [72] E. E. Rodriguez, F. Poineau, A. Llobet, B. J. Kennedy, M. Avdeev, G. J. Thorogood, M. L. Carter, R. Seshadri, D. J. Singh and A. K. Cheetham, *Phys. Rev. Lett.*, **106**, 067201 (2011).

- [73] G. J. Thorogood, M. Avdeev, M. L. Carter, B. J. Kennedy, J. Ting and K. S. Wallwork, *Dalton Trans.*, **40**, 7228 (2011).
- [74] J. H. de Boer and E. J. W. Verwey, *Proc. Phys. Soc.*, **49**, 59 (1937).
- [75] N. F. Mott and R. Peierls, *Proc. Phys. Soc.*, **49**, 72 (1937).
- [76] J. Kunes, V. I. Anisimov, S. L. Skornyakov, A. V. Lukoyanov and D. Vollhardt, *Phys. Rev. Lett.*, **99**, 156404 (2007).
- [77] J. Hubbard, *Proc. R. Soc. Lond. A*, **276**, 238 (1963).
- [78] J. C. Slater, *Phys. Rev.*, **82**, 538 (1951).
- [79] Y. G. Shi, Y. F. Guo, S. Yu, M. Arai, A. A. Belik, A. Sato, K. Yamaura, E. Takayama-Muromachi, H. F. Tian, H. X. Yang, J. Q. Li, T. Varga, J. F. Mitchell and S. Okamoto, *Phys. Rev. B(R)*, **80**, 161104 (2009).

Chapter 2

Methodology

2.1 Solution to Many Body Hamiltonian

Materials in their different forms are made of atoms which on the other hand are made of positively charged protons, negatively charged electrons and neutral neutrons. Arrangement of these atoms in a regular fashion in repeated units lead to the crystalline structure which one usually encounters in material science. The regular periodicity that one finds here leads to simplifications in the properties of materials. There are also materials in which the ordering is not periodic. Electrostatic interactions between these charged particles are responsible for all diverse properties that they show. In principle, the problem of electromagnetically interacting particles can be described by time independent many body Schrödinger equation of the form of $H\Psi(R, r) = E\Psi(R, r)$ and the exact many body Hamiltonian for such a system can be represented by

$$H = - \sum_i \frac{\hbar^2}{2m_e} \nabla_{\mathbf{r}_i}^2 - \sum_I \frac{\hbar^2}{2M_I} \nabla_{\mathbf{R}_I}^2 - \sum_{i,I} \frac{Z_I e^2}{|\mathbf{R}_I - \mathbf{r}_i|} + \sum_{i>j} \frac{e^2}{|\mathbf{r}_i - \mathbf{r}_j|} + \sum_{I>J} \frac{Z_I Z_J e^2}{|\mathbf{R}_I - \mathbf{R}_J|} \quad (2.1)$$

where $\nabla_{\mathbf{r}_i}^2$ and $\nabla_{\mathbf{R}_I}^2$ are Laplacians containing second order derivatives with respect to electronic and ionic coordinates respectively. m_e and M_I denote mass of the individual electron at position r_i and mass of nucleus at the position R_I respectively. $Z_I e$ is the charge of the nucleus. First two terms in the right hand side describe the kinetic energies of electrons and nuclei respectively. The last three terms denote the Coulomb interaction between nucleus-electron, between different electrons and between two different nuclei respectively. Despite its simplicity, the solution of the many body Schrödinger equation is very difficult due to the presence of coupled electron-electron Coulomb interaction terms and the Hamiltonian cannot be solved exactly beyond the hydrogen atom for technical limitations. In order to find an acceptable solution with sufficient accuracy to describe the diverse properties materials exhibit one can impose various approximations at different levels.

The first and the simplest approximation that one can make is to neglect the kinetic energy of the nuclei. This approximation is based on the idea that the mass of the nucleus is much heavier than that of electron (1836 times) and thus they are expected to move much slower than electrons and any electronic properties can be calculated by assuming ions to be fixed to a position. This simple yet powerful approximation is famously known as the Born-Oppenheimer (BO) approximation [1] . Within this approximation ions are assumed to be fixed in a position, the interactions between ions can be assumed to be constant and is known as Madelung energy [2]. So, under the BO approximation the Hamiltonian can be written as

$$H = - \sum_i \frac{\hbar^2}{2m_e} \nabla_{\mathbf{r}_i}^2 - \sum_{i,I} \frac{Z_I e^2}{|\mathbf{R}_I - \mathbf{r}_i|} + \sum_{i>j} \frac{e^2}{|\mathbf{r}_i - \mathbf{r}_j|} + E_{mad} \quad (2.2)$$

The first term in the R.H.S denotes the electronic kinetic energy of electrons. The effect of nuclei on the electrons is included in the second term and is generally called external potential ($V_{ion}(\mathbf{r}_i)$). Third term is electronic Coulomb interaction and the last one is constant Madelung energy.

The simplest approximation that one can employ is the Hartree approximation. According to this approximation, electrons are assumed to be independent and interact only via a mean field Coulomb interaction developed by all other electrons. The many body wave function for such system can be found in terms of product of single electron wave functions.

$$\Psi(\mathbf{r}_1, \mathbf{r}_2, \dots) = \psi_1(\mathbf{r}_1)\psi_2(\mathbf{r}_2)\dots \quad (2.3)$$

Where $\psi_i(\mathbf{r}_i)$ is the single electron state. Single electron Hamiltonian is given by the independent electron Hamiltonian of the form of $\hat{h}(\mathbf{r}_i, \mathbf{p}_i) = -\frac{\hbar^2}{2m_e} \nabla_{\mathbf{r}_i}^2 - \sum_I \frac{Z_I e^2}{|\mathbf{R}_I - \mathbf{r}_i|} + e^2 \sum_{i \neq j} \langle \psi_j | \frac{1}{|\mathbf{r}_i - \mathbf{r}_j|} | \psi_j \rangle$ and total energy is

$$E = \sum_i \langle \psi_i | \frac{-\hbar^2}{2m_e} \nabla_{\mathbf{r}_i}^2 + V_{ion}(\mathbf{r}) | \psi_i \rangle + e^2 \sum_{i>j} \langle \psi_i \psi_j | \frac{1}{|\mathbf{r}_i - \mathbf{r}_j|} | \psi_i \psi_j \rangle \quad (2.4)$$

where the single electron Hartree equation becomes

$$\left[\frac{-\hbar^2}{2m_e} \nabla_{\mathbf{r}_i}^2 + V_{ion}(\mathbf{r}) + e^2 \sum_{i \neq j} \langle \psi_j | \frac{1}{|\mathbf{r}_i - \mathbf{r}_j|} | \psi_j \rangle \right] \psi_i(\mathbf{r}) = \varepsilon_i \psi_i(\mathbf{r}) \quad (2.5)$$

From the expression of single electron Hartree equation, it is evident that any arbitrary state ψ_i can be determined if all other states ψ_j are known

completely. In practice, this self-consistent problem can be solved iteratively until desired accuracy is reached. In order to describe the fermionic nature which is not included in the Hartree approximation, many body wave functions have to be properly antisymmetrized. This can be satisfied by forming suitable basis states given by Slater determinant [3].

$$\Psi(\mathbf{r}_1, \mathbf{r}_2, \dots) = \frac{1}{\sqrt{N!}} \sum_i (-1)^i \prod_{k=1}^N \psi_k(\mathbf{r}_{k_i}) \quad (2.6)$$

where N is the total number of electrons. This method is known as Hartree-Fock [3] approximation. For the simplest case of two body problem, Slater determinant takes the form of,

$$\Psi(\mathbf{r}_1, \mathbf{r}_2) = \frac{1}{\sqrt{2}} [\psi_1(\mathbf{r}_1)\psi_2(\mathbf{r}_2) - \psi_2(\mathbf{r}_1)\psi_1(\mathbf{r}_2)] \quad (2.7)$$

Now the joint probability for finding particle one in position \mathbf{r}_1 and particle two in position \mathbf{r}_2 is

$$\begin{aligned} |\Psi(\mathbf{r}_1, \mathbf{r}_2)|^2 &= \frac{1}{2} [|\psi_1(\mathbf{r}_1)|^2 |\psi_2(\mathbf{r}_2)|^2 + |\psi_2(\mathbf{r}_1)|^2 |\psi_1(\mathbf{r}_2)|^2 - \\ &\quad \psi_1^*(\mathbf{r}_1)\psi_2^*(\mathbf{r}_2)\psi_1(\mathbf{r}_2)\psi_2(\mathbf{r}_1) - \\ &\quad \psi_1^*(\mathbf{r}_2)\psi_2^*(\mathbf{r}_1)\psi_1(\mathbf{r}_1)\psi_2(\mathbf{r}_2)] \end{aligned}$$

where $|\psi_1(\mathbf{r}_1)|^2$ and $|\psi_1(\mathbf{r}_2)|^2$ are the probability of finding particle one at \mathbf{r}_1 and particle two at \mathbf{r}_2 . For $\mathbf{r}_1 = \mathbf{r}_2 = \mathbf{r}$, we find that the joint probability is vanishing. Thus the formulation of Hartree-Fock method has already taken into account of the effect that two electrons cannot occupy the same position. The one electron Hamiltonian for the i^{th} particle can now be written as

$$H_{HF} = \left[-\frac{\hbar^2}{2m_e} \nabla_{\mathbf{r}_i}^2 + V_{ion}(\mathbf{r}_i) + V_i^H(\mathbf{r}_i) + V_i^x \right] \quad (2.8)$$

where

$$V_i^H(\mathbf{r}_i) = e^2 \sum_{j \neq i} \int \frac{|\psi_j(\mathbf{r}_j)|^2}{|\mathbf{r}_i - \mathbf{r}_j|} d\mathbf{r}_j \quad (2.9)$$

and

$$V_i^x \psi_i(\mathbf{r}_i) = - \sum_{j \neq i} \psi_i(\mathbf{r}_i) \int \psi_j^*(\mathbf{r}_j) \frac{e^2}{|\mathbf{r}_i - \mathbf{r}_j|} \psi_i(\mathbf{r}_j) d\mathbf{r}_j \quad (2.10)$$

are known as Hartree potential and exchange potential respectively. The exchange term describes the effect of exchange interaction between electrons and is different for each state ψ_i . It is instructive to try to write this term in the form of $V_i \psi_i$. To do this, we introduce the concept of single particle and total densities as

$$\rho_i(\mathbf{r}) = |\psi_i(\mathbf{r})|^2 \quad (2.11)$$

and

$$\rho(\mathbf{r}) = \sum_i \rho_i(\mathbf{r}) \quad (2.12)$$

In terms of density, Hartree potential takes the form of

$$V_i^H(\mathbf{r}) = e^2 \sum_{j \neq i} \int \frac{\rho_j(\mathbf{r}')}{|\mathbf{r} - \mathbf{r}'|} d\mathbf{r}' = e^2 \int \frac{\rho(\mathbf{r}') - \rho_i(\mathbf{r}')}{|\mathbf{r} - \mathbf{r}'|} d\mathbf{r}' \quad (2.13)$$

Similarly single particle exchange density can be written as

$$\rho_i^X(\mathbf{r}, \mathbf{r}') = \sum_{j \neq i} \frac{\psi_i(\mathbf{r}') \psi_i^*(\mathbf{r}) \psi_j(\mathbf{r}) \psi_j^*(\mathbf{r}')}{\psi_i(\mathbf{r}) \psi_i^*(\mathbf{r})} \quad (2.14)$$

and exchange potential as

$$V_i^X(\mathbf{r}) = -e^2 \int \frac{\rho_i^X(\mathbf{r}, \mathbf{r}')}{|\mathbf{r} - \mathbf{r}'|} d\mathbf{r}' \quad (2.15)$$

Hartree-Fock potential is thus given by

$$V_i^{HF}(\mathbf{r}) = e^2 \int \frac{\rho(\mathbf{r}')}{|\mathbf{r} - \mathbf{r}'|} d\mathbf{r}' - e^2 \int \frac{\rho_i(\mathbf{r}') + \rho_i^X(\mathbf{r}, \mathbf{r}')}{|\mathbf{r} - \mathbf{r}'|} d\mathbf{r}' \quad (2.16)$$

which gives rise to Hartree-Fock density $\rho_i^{HF}(\mathbf{r}, \mathbf{r}')$. Total electron electron interaction potential in terms of Hartree-Fock density is given by

$$V_i^{HF}(\mathbf{r}) = e^2 \int \frac{\rho(\mathbf{r}') - \rho_i^{HF}(\mathbf{r}, \mathbf{r}')}{|\mathbf{r} - \mathbf{r}'|} d\mathbf{r}' \quad (2.17)$$

The exchange term is extremely difficult to derive in practice because it takes into account all the interactions between all electrons in the system. Consequently, Hartree-Fock method is computationally expensive.

2.2 Beyond Hartree-Fock:

Density Functional Theory

Apart from the wave function based method that we have already discussed, another effective way of solving the many body Hamiltonian is density functional theory (DFT) based method. As the name suggests, one deals with the density of the ground state electron distribution instead of the wave function. All ground state properties of the many body problem are then expressed as the functional of the ground state electron density. Success of the DFT approach is based on the success of Hohenberg and Kohn theorem [4] and the derivation of a set of equations by Kohn and Sham [5] in the mid 1960s. According to Hohenberg-Kohn theorem the ground state properties of many

electrons system can be uniquely determined by a single electron density. Though the original Hohenberg and Kohn theorems were formulated only for non-degenerate ground states in the absence of a magnetic field but they have now been generalized [6] and can be applied for degenerate system as well.

The first Hohenberg-Kohn theorem [4] states that the external potential $V_{ext}(\mathbf{r})$ and hence the total energy is a unique functional of a single electron density $n(\mathbf{r})$. Thus

$$E[n(\mathbf{r})] = \int n(\mathbf{r})V_{ext}(\mathbf{r})d\mathbf{r} + F[n(\mathbf{r})] \quad (2.18)$$

where $F[n(\mathbf{r})]$ is an unknown functional of a single electron density $n(\mathbf{r})$. The problem of N electrons with $3N$ degrees of freedom thus reduces to the problem of one electron with three degrees of freedom only. This huge simplification by Hohenberg-Kohn theorem gives the ability to deal with larger systems.

Second Hohenberg-Kohn theorem states that the ground state energy can be obtained variationally. The single electron density which minimizes the total energy is the exact ground state density. So, variationally we can achieve a density $n(\mathbf{r})$ such that $E[n'(\mathbf{r})] > E[n(\mathbf{r})]$ for all $n'(\mathbf{r})$. This density is the exact single electron density which mimics the many body electron density that we started with. Thus within the framework of DFT the intractable problem of N coupled electrons in an external potential is reduced to a tractable single electron in an effective potential problem.

2.2.1 The Kohn-Sham Equations

Kohn and Sham separated $F[n(\mathbf{r})]$ into three distinct parts so that the functional $E[n(\mathbf{r})]$ becomes

$$E[n(\mathbf{r})] = T_s[n(\mathbf{r})] + \frac{1}{2} \int \int \frac{n(\mathbf{r})n(\mathbf{r}')}{|\mathbf{r} - \mathbf{r}'|} d\mathbf{r}d\mathbf{r}' + E_{xc}[n(\mathbf{r})] + \int n(\mathbf{r})V_{ext}(\mathbf{r})d\mathbf{r} \quad (2.19)$$

where $T_s[n(\mathbf{r})]$ is defined as the kinetic energy of a non-interacting electron gas with density $n(\mathbf{r})$,

$$T_s[n(\mathbf{r})] = -\frac{1}{2} \sum_i \int \psi_i^*(\mathbf{r})\nabla^2\psi_i(\mathbf{r})d\mathbf{r} \quad (2.20)$$

where we have taken \hbar and m_e as unity and T_s is not the kinetic energy of the real system. Equation 1.19 also defines the exchange correlation energy functional. As the total number of electrons in a closed system is fixed, we obtain

$$\frac{\delta}{\delta n(\mathbf{r})} \left[E[n(\mathbf{r})] - \mu \int n(\mathbf{r})d\mathbf{r} \right] = 0 \quad (2.21)$$

$$or \quad \frac{\delta E[n(\mathbf{r})]}{\delta n} = \mu \quad (2.22)$$

This equation can now be written in terms of effective potential as

$$\frac{\delta T_s[n(\mathbf{r})]}{\delta n(\mathbf{r})} + V_{eff}(\mathbf{r}) = \mu \quad (2.23)$$

where

$$V_{eff}(\mathbf{r}) = V_{ext}(\mathbf{r}) + \int \frac{n(\mathbf{r}')}{|\mathbf{r} - \mathbf{r}'|} d\mathbf{r}' + V_{xc}(\mathbf{r}) \quad (2.24)$$

$$\text{and } V_{xc}(\mathbf{r}) = \frac{\delta E_{xc}[n(\mathbf{r})]}{\delta n(\mathbf{r})} \quad (2.25)$$

To find the ground state energy E_0 and the ground state density n_0 , the one electron Schrödinger equation

$$\left(-\frac{1}{2}\nabla_i^2 + V_{eff}(\mathbf{r}) - \varepsilon_i \right) \psi_i(\mathbf{r}) = 0 \quad (2.26)$$

should be solved self consistently with

$$n(\mathbf{r}) = \sum |\psi_i(\mathbf{r})|^2 \quad (2.27)$$

2.2.2 Exchange-Correlation Functional

In the simplest form the idea of correlation can be described from the definition of the joint probability density of finding one particle at position \mathbf{r}_a with the other particle at \mathbf{r}_b . If these two particles are correlated then the probability of finding one particle at a certain position depends on the presence of the other particle at another position. Thus for a correlated system of particles, the joint probability cannot be defined as the product of the individual probability densities. On the other hand, exchange interaction is purely quantum mechanical effect between identical particles. This effect is due to the property of wave functions of indistinguishable particles subjected to exchange symmetry. For Fermions, the total wave functions change their sign when two particles exchange their coordinates whereas for Bosons they do not change. The idea of exchange and correlation is already there in the Hartree-Fock treatment of the many electron problem where wave function is approximated in the form of a single Slater determinant of single particle orbitals. The electron-electron interaction energy consists of a classical

electrostatic part and the remainder which is the exchange energy. The remaining difference between the Hartree-Fock energy and the total energy is defined as the correlation energy.

For any practical use of the density functional theory, we must know the exact form of the exchange-correlation functional. However the exact form is not known and may not be calculated exactly for any real system. Different levels of approximations are made to take care of the exchange-correlation functional. The quality of any DFT calculation thus solely depends on the quality of the approximation that one employs during the formation of potential functional. Several successful approximations have so far been designed and they can be categorized according to their level of complexity.

2.2.3 Local Density Approximation (LDA)

The simplest yet one of the most popular approximation to the exchange-correlation functional is the local density approximation (LDA) which assumes that the exchange correlation energy solely depends on the value of the electronic density at that real space point. Thus the total exchange-correlation energy of the system can be written as

$$E_{xc}^{LDA}[\rho] = \int \rho(\mathbf{r}) \epsilon_{xc}^{homo} d\mathbf{r} \quad (2.28)$$

where ϵ_{xc}^{homo} is the exchange-correlation energy per particle of a homogeneous electron gas of density ρ . In practice, exchange (E_x) and correlation (E_c) parts are calculated separately. The exchange term takes the simple analytic form with the approximation that the exchange energy in a system where the density is not homogeneous can be obtained by applying homogeneous electron gas results point-wise leading to the form

$$E_x^{LDA}[\rho] = -\frac{3}{4} \left(\frac{3}{\pi} \right)^{\frac{1}{3}} \int \rho(\mathbf{r})^{\frac{4}{3}} d\mathbf{r} \quad (2.29)$$

The correlation energy term is more complicated and cannot be calculated analytically. They are generally obtained by fitting the energies to the many body studies [8]. In modern DFT there are different functional like Perdew-Zunger(PZ) [9], Perdew-Wang(PW) [10], Cole-Perdew(CP) [11], Vosko-Wilk-Nusair(VWN) [12] depending on the fitting algorithm.

By construction, LDA exchange-correlation functional should be valid for slowly varying densities only. But surprisingly it works exceptionally well for both the metallic as well as insulating systems. This can be explained crudely by the systematic error cancellation argument. In a homogeneous system LDA underestimates correlation energy but over estimates exchange functional energy term leading to a good estimation of the overall exchange-correlation energy. Despite its efficiency, recent studies have shown that LDA tends to overestimate cohesive energy by as much as 15-20% and underestimates lattice constants by 2-3% [13]. Apart from these, the problem of underestimation of the band gap [14] and inability to calculate long range van der Waals interactions are also known. Despite all these problems, LDA often is the first choice for several DFT calculations.

2.2.4 Generalized Gradient Approximation (GGA)

Despite the systematic error correction of LDA approach, it is often not a reasonable approximation for the rapidly varying electron densities of most of the materials and the necessity for a better approximation was realized long back. The next improvement one can consider is to take into account

the gradient at each point along with the density at the same position. Such functional of the form of

$$E_{xc}^{GGA}[\rho] = \int \epsilon_{xc} f^{GGA}[\rho(\mathbf{r}), \nabla\rho(\mathbf{r})] d\mathbf{r} \quad (2.30)$$

are known as the GGA functional. As the functional depends on the gradient of electron density as well, it is often called "semi-local" functional. Many properties, like geometries [15], ground state energies [16] and the effect of weakly bonded systems have been calculated with better accuracy than LDA. Depending upon the choice of f^{GGA} several GGA functional have been developed such as Perdew and Wang [10], Becke-Lee-Yang-Parr (BLYP) [17], Perdew, Burke and Ernzerhof(PBE) [18]. Despite all the improvements made, GGA also exhibits a tendency to overestimate lattice parameters [19] and to underestimate band gaps [20] for semiconductors and insulators.

2.2.5 Plane Wave Pseudopotential Method

Applicability of any density functional theory based calculation depends on the quality of the basis set that one setup to construct the single particle wave function. Any orthonormalized set of eigen function Ψ_n^k under a periodic potential can be represented exactly by a linear combination of infinite set of plane wave basis

$$\Psi_n^k(\mathbf{r}) = \sum_{\mathbf{K}} C_{\mathbf{K}} e^{i(\mathbf{k}+\mathbf{K})\cdot\mathbf{r}} \quad (2.31)$$

where \mathbf{K} is the reciprocal lattice vector. Since each basis function is \mathbf{k} dependent, we need a set of infinite \mathbf{k} points to describe the wave function exactly.

In practice this is impossible to work with and some simplification should be made. One can introduce a \mathbf{k} vector \mathbf{k}_{max} , so that $\mathbf{k} < \mathbf{k}_{max}$. Within a free electron model one can think of a characteristic cutoff energy $E_{cut} = \frac{\hbar^2 k_{max}^2}{2m_e}$ and all plane wave states within this sphere of radius \mathbf{k}_{max} are included in this basis set. We can further simplify our construction if we apply the idea that valence electrons actively participate in determining most of the properties of any system. This is the key idea behind the success of the pseudopotential method. The strong Coulomb potential of the nucleus and the effect of tightly bound core electrons are replaced by an effective potential acting on the valence electrons.

First successful implementation of the concept described above was Orthogonalized Plane Wave method (OPW) by Herring in 1940 [21]. The idea was to build valence states using plane waves that are orthogonal to the core states. The OPW states constructed by this formulation is given by

$$\psi_k^{OPW}(\mathbf{r}) = \frac{1}{\rho} \left\{ e^{i\mathbf{k}\cdot\mathbf{r}} - \sum_j \langle u_j | \mathbf{k} \rangle u_j(\mathbf{r}) \right\} \quad (2.32)$$

the condition that $\psi_k^{OPW}(\mathbf{r})$ is orthogonal to each function u_j gives

$$\langle u_j | \mathbf{q} \rangle = - \int u_j(\mathbf{r}) e^{i\mathbf{k}\cdot\mathbf{r}} d\mathbf{r} \quad (2.33)$$

The ability to choose the localized function u_j properly divides $\psi_k^{OPW}(\mathbf{r})$ into a smooth part plus a localized part. This smooth function can be represented conveniently by plane waves. Philips and Kleinman [22] showed that one can construct a smooth valence function $\psi_i^v(\mathbf{r})$ given by

$$\psi_i^v(\mathbf{r}) = \tilde{\psi}_i^v(\mathbf{r}) + \sum_j B_{ij} u_{ij}(\mathbf{r}) \quad (2.34)$$

where ψ_i^v is the valence wave function $\tilde{\psi}_i^v$ is the smooth part and B_{ij} is the orthogonalization coefficient and the original Hamiltonian for the smooth wave function becomes

$$\begin{aligned} H\tilde{\psi}_i^v(\mathbf{r}) &= \left[-\frac{1}{2}\nabla^2 + \tilde{V}(\mathbf{r})\right]\tilde{\psi}_i^v(\mathbf{r}) \\ &= \epsilon_i^v\tilde{\psi}_i^v(\mathbf{r}) \end{aligned}$$

with $\tilde{V} = V + V^R$ where, V is the effective potential for ψ_i^v and V^R is a non local operator with

$$V^R\tilde{\psi}_i^v(\mathbf{r}) = \sum_j (\epsilon_i^v - \epsilon_j^c) \langle \psi_j^c | \tilde{\psi}_i^v \rangle \psi_j^c(\mathbf{r}) \quad (2.35)$$

From the definition V^R is repulsive in nature due to the presence of positive energy term $(\epsilon_i^v - \epsilon_j^c)$. A deeper core state leads to a stronger repulsive potential. Thus \tilde{V} is much weaker than the original potential. This weak potential is known as the pseudo potential. New functions $\tilde{\psi}_i^v$ obey the single particle equation with a modified potential are called pseudo wave functions. They are not orthonormal because the complete function ψ_i^v contains the sum over the core orbitals. Norm-conserving potentials remove this complication by implementing some restrictions. In norm-conserving potentials the all electron (AE) wave function is replaced by a node-less pseudo wave function with the restriction on the pseudo wave function that the integrated charge inside the core radius have to be same for the AE as well as PS wave function. This ensures that the total charge in the core region is correct and the normalized pseudo orbitals is equivalent to the true orbitals outside the core radius.

2.2.6 Projector Augmented Wave (PAW) Method

Pseudo potential method is very efficient to describe valence electron properties. But the information of the full wave function near the core region is completely lost and cannot be obtained. This can influence the calculation of certain properties especially dependent on the core electron information such as hyperfine parameters. Core electron properties can be obtained by augmented plane wave (APW) method. In APW total wave function is divided into two parts. Atom centered augmentation spheres where spherically symmetric partial waves are used and bonding region outside of the sphere spanned by some envelope function. Full wave functions are constructed by matching solutions at the boundary of the augmented sphere. Projector augmented wave (PAW) method, first proposed by Blöchl in 1994 [23] is a more general approach which treats APW and pseudopotential method as special cases. Thus PAW approaches the issue of rapidly oscillating wave function into smooth wave functions which are computationally convenient and provides a way to deal with all electron properties.

As the feature of wave functions are very different in augmented sphere as well as bonding region we need a linear transformation operator to take us from the smooth wave function $|\tilde{\psi}\rangle$ to the all electron wave function $|\psi\rangle$.

$$|\psi\rangle = \tau |\tilde{\psi}\rangle \tag{2.36}$$

All electrons and smooth wave functions differ only near core region. Thus the operator can be written as $\tau = 1 + \sum_R \hat{\tau}_R$ where $\hat{\tau}_R$ is non zero within augmentation sphere Ω only. Inside the sphere pseudo wave function is expanded as $|\tilde{\psi}\rangle = \sum_i |\tilde{\phi}_i\rangle c_i$. We define projector function p_i inside the sphere so that $\langle p_i | \tilde{\phi}_j \rangle = \delta_{ij}$. The all electron partial wave functions are chosen to be solutions of isolated atom Kohn-Sham equation and we can

explicitly write down the transformation as

$$\tau = 1 + \sum_i (|\phi_i \rangle - |\tilde{\phi}_i \rangle) \langle p_i| \quad (2.37)$$

The PAW method combines the above idea with the frozen core approximation. According to frozen core approximation the core states are assumed not to be affected by the environment. Thus the core Kohn-Sham states are taken to be identical to the core states of isolated atoms.

2.2.7 Flow Chart of a DFT Calculation

A typical DFT iterative routine starts with the structural information of the system and the atomic potentials of the constituent atoms. A guess electron density is formed from the linear combination of the individual electron density and the Kohn-Sham equation is set up and diagonalized. Blocked Davidson iteration scheme, residual minimization scheme by direct inversion in the iterative subspace are two of the famous diagonalization subroutines frequently used for such purposes. The system energy is calculated and checked for the convergence set by the user. Usually a convergence energy of 10^{-5} eV is a standard choice. New electron density is calculated from the old one and the Hamiltonian is diagonalized until the convergence criterion is achieved. At this point one can optionally set the routine for structural optimization. For such calculations the force on individual atom is calculated and force convergence criterion is checked. Atoms are moved according to force directions and the new electron density is calculated again for the modified positions of the atoms. Diagonalization subroutine iterate until one achieves energy as well as force convergence simultaneously. At the end of the iteration, one ends up with the ground state energy, single electron density which can be used for further analysis such as calculating density of states

or band dispersion, optimized structure and other physical properties of the system. The flow chart of a standard DFT calculation is shown in the Figure 2.1.

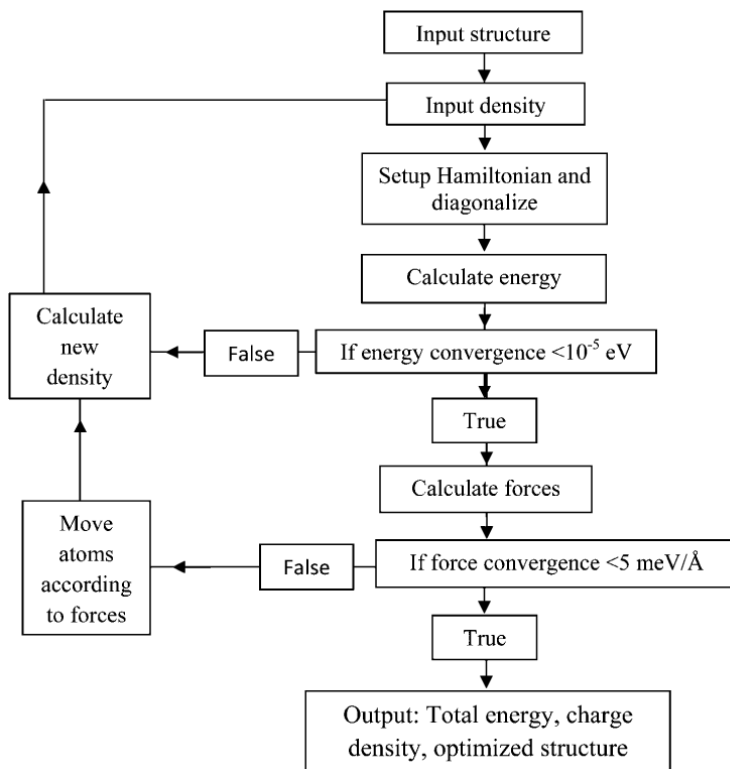


Figure 2.1: Flowchart of the DFT electronic structure calculation

2.3 Maximally Localized Wannier Function

In most of the electronic properties study of solids, the states typically lying within a limited occupied energy range close to the Fermi energy contribute significantly to all the properties under consideration. Tight binding model and Hubbard model are based on this idea in which only a minimal set of energy bands are considered. These models rely on the existence of such

minimal set of spatially localized orbitals spanning the relevant subspace. Wannier representation of localized orbitals is an alternative representation of real space wave functions defined via unitary transformation of the Bloch orbitals and labeled according to the band index n and the lattice translation vector \mathbf{R} . Thus Wannier functions

$$\omega_{n\mathbf{R}}(\mathbf{r}) = \frac{V}{(2\pi)^3} \int_{BZ} \left[\sum_m U_{mn}^{\mathbf{k}} \psi_{m\mathbf{k}}(\mathbf{r}) \right] e^{-i\mathbf{k}\cdot\mathbf{R}} d\mathbf{k} \quad (2.38)$$

where V is the volume of the unit cell, the integral is over the whole Brillouin zone and $U^{\mathbf{k}}$ is an unitary transformation that mixes the Bloch states. Choice of $U^{\mathbf{k}}$ is not unique and different choices lead to different Wannier functions with different spatial extensions. Wannier representation of the electronic structure problem is widely known for its usefulness but the non uniqueness of unitary matrix $U^{\mathbf{k}}$ makes it unsuitable to be applicable for any practical problem. However prescription of Marzari and Vanderbilt [24] gives a practical solution to obtain Maximally Localized Wannier Functions (MLWF) for isolated band structure problem and then extended by Souza et.al [25] for entangled band problem as well. The idea is based on the minimization of real space spread (Ω) of the WF, defined earlier. Ω is defined as

$$\Omega = \sum_n \left[\langle \omega_{n_0}(\mathbf{r}) | r^2 | \omega_{n_0}(\mathbf{r}) \rangle - |\langle \omega_{n_0}(\mathbf{r}) | \mathbf{r} | \omega_{n_0}(\mathbf{r}) \rangle|^2 \right] \quad (2.39)$$

This total spread can be decomposed into a gauge invariant term Ω_I and gauge dependent term $\tilde{\Omega}$. $\tilde{\Omega}$ can further be divided into diagonal and off-diagonal terms.

$$\Omega_I = \sum_n \left[\langle \omega_{n_0}(\mathbf{r}) | r^2 | \omega_{n_0}(\mathbf{r}) \rangle - \sum_{m\mathbf{R}} |\langle \omega_{n\mathbf{R}}(\mathbf{r}) | \mathbf{r} | \omega_{n_0}(\mathbf{r}) \rangle|^2 \right] \quad (2.40)$$

$$\Omega_D = \sum_n \sum_{\mathbf{R} \neq 0} |\langle \omega_{n\mathbf{R}}(\mathbf{r}) | \mathbf{r} | \omega_{n_0}(\mathbf{r}) \rangle|^2 \quad (2.41)$$

$$\Omega_{OD} = \sum_{m \neq n} \sum_{\mathbf{R}} |\langle \omega_{m\mathbf{R}}(\mathbf{r}) | \mathbf{r} | \omega_{n_0}(\mathbf{r}) \rangle|^2 \quad (2.42)$$

For an isolated group of bands Ω_I is invariant under any gauge transformation, so the minimization of $\tilde{\Omega}$ is sufficient for the minimization of Ω . In order to obtain MLWF for entangled bands, method of disentanglement procedure in a subset of energy window is applied. This procedure defines an $N_{\mathbf{k}}$ dimensional Hilbert space $F(\mathbf{k})$ at each \mathbf{k} points so that if $N_{\mathbf{k}} > N$, the aim is to find a subspace $S(\mathbf{k}) \subseteq F(\mathbf{k})$ among all the possible N dimensional subspace of $F(\mathbf{k})$ leading to the smallest Ω_I . Then minimization of $\tilde{\Omega}$ is applied in the subspace $S(\mathbf{k})$ to obtain the maximally localized WF. In Figure 2.2 I have shown maximally localized Wannier function of Fe dz^2 orbital for Fe intercalated TaS_2 structure from one of our calculations.

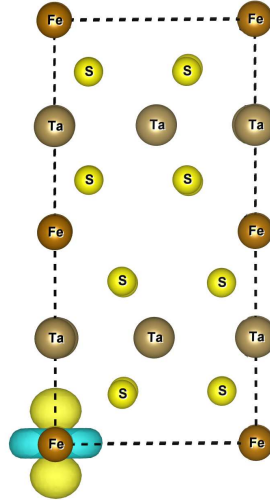


Figure 2.2: Maximally localized Wannier function of one of the Fe dz^2 orbital in Fe intercalated TaS_2 .

Bibliography

- [1] M. Born and R. Oppenheimer, *Annalen der Physik* **389**, 457 (1927).
- [2] C. Kittel, *Introduction to Solid State Physics*, Wiley (1995).
- [3] P. W. Atkins, *Molecular Quantum Mechanics: An Introduction to Quantum Chemistry*, Parts 1-2, Oxford University Press (1977).
- [4] P. Hohenberg and W. Kohn, *Phys. Rev. B* **136** B864 (1964).
- [5] W. Kohn and L. J. Sham, *Phys. Rev.* **140** A1133 (1965).
- [6] G. Vignale and M. Rasolt, *Phys. Rev. Lett.* **59**, 2360 (1987).
M. Levy, *Proceedings of the National Academy of Sciences* **76**, 6062 (1979).
- [7] T. D. Kuhne, M. Krack and M. Parrinello, *J. Chem. Theo. Comput* **5**, 235 (2009).
- [8] M. Gell-Mann and K. A. Brueckner, *Phys. Rev.* **106**, 364 (1957).
D. M. Ceperley and B. J. Alder, *Phys. Rev. Lett.* **45**, 566 (1980).
- [9] J. P. Perdew and A. Zunger, *Phys. Rev. B* **23**, 5048 (1981).
- [10] J. P. Perdew and Y. Wang, *Phys. Rev. B* **45**, 13244 (1992).

- [11] L. A. Cole and J. P. Perdew, Phys. Rev. A **25**, 1265 (1982).
- [12] S. H. Vosko, L. Wilk and M. Nusair, Can. J. Phys. **58**,1200 (1980).
- [13] V. N. Staroverov, G. E. Scuseria, J. Tao, and J. P. Perdew, Phys. Rev. B **69**, 075102 (2004).
- G. I. Csonka, J. P. Perdew, A. Ruzsinszky, P. H. T. Philipsen, S. Lebegue, J. Paier, O. A. Vydrov, and J. G. Angyan, Phys. Rev. B **79**, 155107 (2009).
- J. Harl, L. Schimka and G. Kresse, Phys. Rev. B **81**, 115126 (2010).
- [14] A. Seidl, A. Gorling, P. Vogl and J. A. Majewski, Phys. Rev. B **53**, 3764 (1996).
- [15] J. P. Perdew, K. Burke and M. Ernzerhof, Phys. Rev. Lett. **77**, 3865 (1996).
- [16] B. Hammer, L. B. Hansen and J. K. Norskov, Phys. Rev. B **59**, 7413 (1999).
- [17] A.D. Becke, J. Chem. Phys. **96**, 2155 (1992).
- [18] J. P. Perdew, K. Burke and M. Ernzerhof, Phys. Rev. Lett. **77**, 3865 (1996).
- [19] A. Zoroddu, F. Bernardini, P. Ruggerone and V. Fiorentini, Phys. Rev. B **64**, 045208 (2001).
- [20] H. Xiao, J. Tahir-Kheli and W. A. Goddard, Phys. Chem. Lett. **2**, 212 (2011).
- [21] C. Herring, Phys. Rev. **57**, 1169 (1940).
- C. Herring and A. G. Hill, Phys. Rev. **58**, 132 (1940).

- [22] J. C. Phillips and L. Kleinman, Phys. Rev. **116**, 287 (1959).
- [23] P. E. Blöchl, Phys. Rev. B **50**, 17953 (1994).
- [24] N. Marzari and D. Vanderbilt, Phys. Rev. B **56**, 12847 (1997).
- [25] I. Souza, N. Marzari and D. Vanderbilt, Phys. Rev. B **65**, 035109 (2001).

Chapter 3

The Role of Passivants on the Stoichiometry of CdSe and GaAs Nanocrystals

3.1 Introduction

One finds significantly different properties from the bulk as one approaches the nano regime. This has led to intense research activity in these materials over the past two decades. The strong dependence of physical properties on size, found especially in semiconductors, has significant technological implications and this coupled with the ease of fabrication and processing makes this class of materials promising building blocks for materials with designed functions [1–3]. In the past decade or so, colloidal chemistry route to the synthesis of nano particles has emerged as a popular route to semiconductor nano particles with wide ranging applications [4–6]. An access to a control

This chapter is based on J. Phys. Chem. C, **117**, 21981 (2013).

of the properties requires an ability to control the uniformity of size, shape, composition, crystal structure, surface, magnetic, optical and other properties. Theoretically various aspects of the physics of nano particles/nano crystals(NCs) have been investigated in the past using ab-initio methods which have been quite successful in explaining various experimentally observed phenomena. The self purification of dopants in Si nano particles [7], Mn emission in Mn doped CdS NCs [8], magnetic properties of Fe/Cu codoped ZnO NCs [9], role of dimensionality and quantum confinement in p-type semiconductor Indium Phosphide quantum dots(QDs) [10] are some examples which have been successfully investigated.

A typical synthesis of nano particles consists of three components namely precursors, organic surfactants and solvent(s). Initially precursors decompose in solution or react at relatively high temperatures to form a super-saturation of monomers/dimers/trimers etc. followed by a burst of nucleation centers and the growth of nano particles. A passivant which is usually an organic surfactant is used to prevent an uncontrolled agglomeration of nano particles. These organic molecules attach themselves to the surface of the NCs and prevent agglomeration by means of charge neutralization. They also saturate all surface dangling bonds to prevent any optical transitions involving surface states [11].

The role of the introduced passivants has been seen to be more than just a parameter introduced during the growth of the nano particles to control the size of the NC. Earlier works have found them responsible for non-traditional roles [12–15] which emerge as a consequence of their binding with the surface atoms. In the case of thiolated gold NCs [16], what has been seen is that the strong interaction between the ligand atoms of the passivant and the gold atoms changes the d electron count of the surface atoms, thus inducing a

small magnetic moment. The early work by Peng et al. [17] showed that some of the ligands were found to bind more strongly than others to the cations on the surface. As different surfaces had different number of cations, this led to the growth of highly anisotropic structures with those directions to which fewer passivants were attached growing faster than others. This interaction could also in some cases modify the band gap of the semiconductor [18]. This is because in the ideal case the passivant would interact with the surface atoms and remove band gap states. However, in the case that the interactions were not strong enough, the states would remain in the band gap region, thereby modifying the band gap [18]. The oscillator strengths for the optical transitions associated with such transitions would be drastically reduced compared to the band edge transitions involving atoms from the core region of the NC [19, 20].

Binary semiconductors which belong to III-V and II-VI groups of the periodic table mainly exist in two different phases - wurtzite and zincblende, with the energy difference between them being very small, of the order of few meV [21]. It has been shown that the choice of the passivant as a result of stronger binding to a particular surface could induce a change in the delicate energy balance that determines the favoured crystal structure [12, 13] in these systems. Thus the strong interaction of the ligand has been recognized to lead to modifications of the properties of the NC compared to their bulk counterparts. In this work we go a step further in this direction. Considering a cation at the surface, when confronted with the choice of binding to a passivating ligand and an anion, one finds that it is the strength of the bond that dictates the choice. Atoms at different surfaces however have different coordinations with the atoms of the layer below. A stronger binding with the passivating ligand implies that those surfaces in which the surface atoms form more bonds with the passivating ligands are the ones that are stabilized.

Analyzing few surfaces in the case of zincblende semiconductors, we find that the polar surfaces comprise the more under-coordinated surfaces. As a result, considering the example of CdSe and GaAs, enroute to the bulk limit, we find that the passivating ligands play an important role in controlling the surface stoichiometry and could in turn result in the growth of highly non-stoichiometric NCs.

3.2 Methodology

NCs of GaAs and CdSe were generated preserving the underlying tetrahedral coordination of the bulk zincblende lattice. In one scheme of generation, NCs were generated by considering a central atom and adding one layer at a time. The structure generated for GaAs for the case where four layers were added ($l=4$) is shown in Figure 3.1a. This is generated by considering a Ga atom at the core. The first layer ($l=1$) that is added consists of four As atoms, which are singly coordinated with the Ga atom at the core. The next layer ($l=2$) of twelve Ga atoms are then added and depending on the number of layers, l subsequent layers are added. This scheme of generation led to highly non-stoichiometric NCs as we can see from Table 3.1. While we considered the central atom to be Ga in the case of GaAs, it was taken to be Se in the case of CdSe NCs. In the other scheme of generation of the NCs, spheres of desired radii centered at an atom were cut out from supercells of the zincblende structure. These are shown in Figure 3.1b and the generated NCs are almost stoichiometric as one finds in Table 3.1. In the present case the label l is used to denote the maximum number of layers present in the NC. While we took these NCs as the starting structures for a set of calculations, the surface atoms were passivated with cationic (passivant that attaches to the anion)

and anionic (passivant that attaches to the cation) pseudo-hydrogens with the proper charge to neutralize the charge on the atom [22] for another set of calculations. For instance, considering the example of CdSe, each Cd atom donates 0.5 electron to each CdSe bond. So, a passivant that attaches itself to Cd should have the charge 1.5, so that it has a filled shell after receiving the charge from Cd. Similarly the cationic passivant which attaches itself to Se has a charge of 0.5, so that it has an empty shell after donating the charge to Se. In case of GaAs, we have used cationic and anionic passivants of charges .25e and 1.75e respectively. For a single coordinated (coordination between Ga and As or Cd and Se) surface atom we have used three such passivants, for double coordinated surface atom two such passivants have been used and for triple coordinated atom, one such passivant has been used (Figure 3.1). This methodology of using pseudo-hydrogens has been used extensively and successfully in the literature to explain various effects [8, 9, 23, 24].

As the implementation of density functional theory that we use is for periodic systems, 12 Å of vacuum is introduced in each direction to minimize the interactions between periodic images. Electronic structure calculations were performed within a plane wave pseudo potential implementation of density functional theory as implemented in the Vienna Ab initio Simulation Package code(VASP) [13, 14] using projector augmented wave (PAW) [15] potentials. The potential used for Ga had the Ga d states as a part of the core as this was seen to be adequate earlier [28]. The GGA PW91 [16] approximation for the exchange correlation functional has been used. All calculations were performed at gamma point alone. Full geometrical relaxations were done for all structures until an energy convergence better than 10^{-5} eV was achieved and the atomic force on each atom was less than $5\text{meV}/\text{Å}$. A typical flowchart of such calculation is shown in Figure 2.1. Volume of the relaxed NCs was

	Radii in Å	Number of atoms with coordination		% of single and double coordinated atoms
		1 or 2	3 or 4	
Non Stoichiometric	GaAs			
l=1	2.5	4	1	80
l=2	4.3	12	5	71
l=3	6.0	24	17	59
l=4	8.0	42	41	51
l=5	9.5	60	87	41
Stoichiometric				
l=2	5.1	12	17	41
l=3	5.5	6	29	17
l=4	7.7	24	63	28
l=4	9.3	24	119	17

Table 3.1: Approximate radii, number of atoms with different coordinations, and fraction of single and double coordinated atoms in A centered binary NCs of type A_mB_n as a function of the number of layers l

determined by the convex hull method and radii have been calculated by mapping volume into the formula of a sphere.

For the surface calculations we have chosen the non polar (110) as well as the polar (100), (111) surfaces for the zincblende structure. Slabs consisting of 16 CdSe monolayers were used to mimic the (110) surface while we used 17 CdSe monolayers to mimic (100) and (111) Se surfaces. Vacuum of 12 Å between two periodic images along the growth direction was introduced to minimize the interaction between images. A gamma centered $6 \times 6 \times 1$ K points mesh was used for the surface calculations. The surface calculations

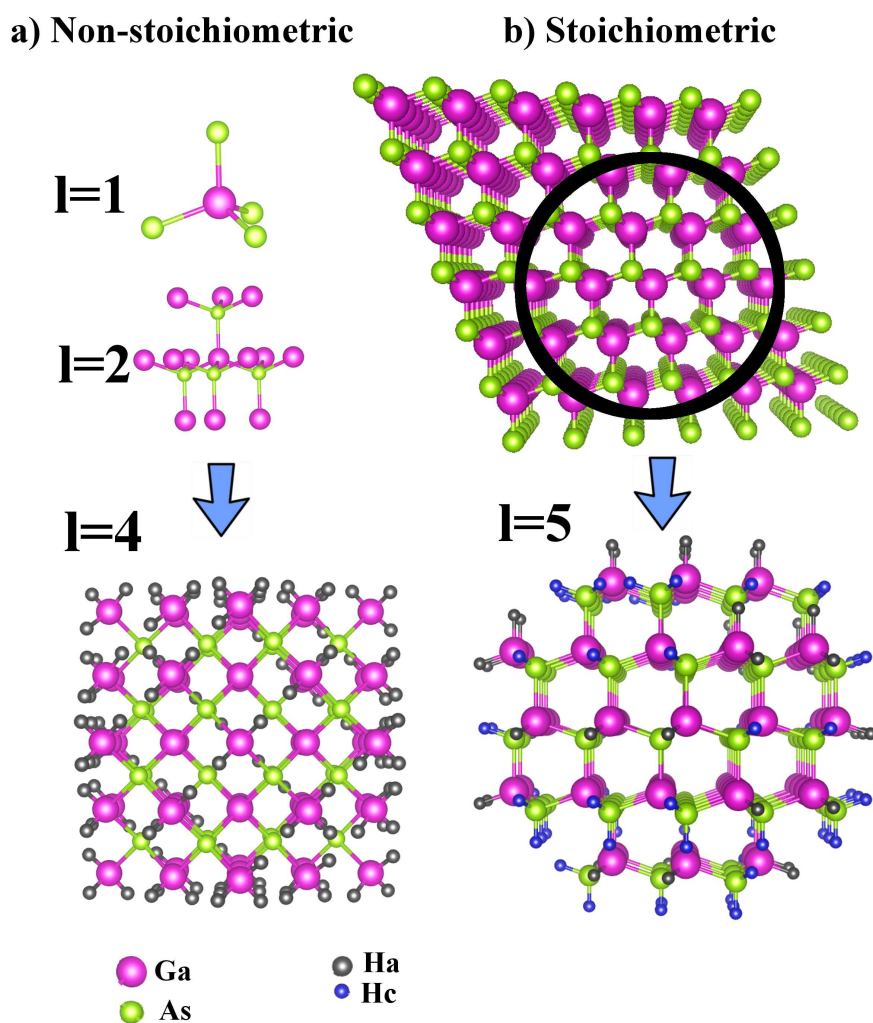


Figure 3.1: Structure generation procedure for non-stoichiometric and stoichiometric NCs of GaAs and CdSe. (a) Non-stoichiometric structures were generated by adding concentric layers of cations and anions. (b) Stoichiometric structures were generated by truncating spheres from supercell.

were performed with pseudo hydrogens with the appropriate charge as used in the case of the NCs. These results were contrasted with those in which no passivant was used.

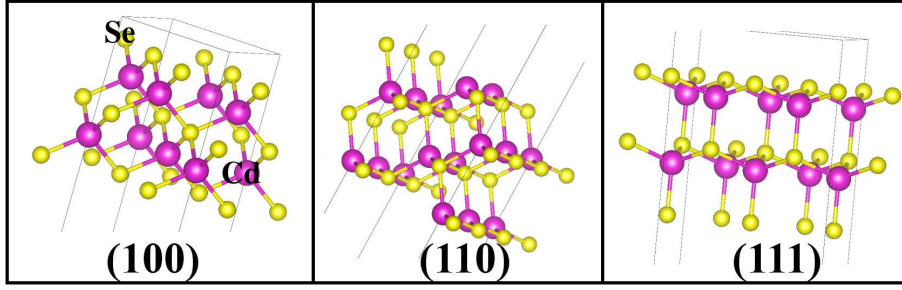


Figure 3.2: Different surfaces considered for the zinc blende structures.

In order to understand the stability of NCs as well as surfaces quantitatively, the formation energy was calculated by the formula

$$\Delta H_f = \frac{1}{m+n} [E(A_m B_n H c_p H a_q) - mE(A) - nE(B) - pE(Hc) - qE(Ha) - m\mu_A - n\mu_B] \quad (3.1)$$

Here, $E(A_m B_n H c_p H a_q)$ is the total energy of the NC or surface consisting of m number of element A, n number of element B and p and q numbers of the two types of pseudo-hydrogen atoms respectively while $E(A)$ and $E(B)$ are the energies of the elements A and B in their most stable bulk structure. $E(Hc)$ and $E(Ha)$ have been evaluated considering a binary molecule formed by the pseudo-hydrogens respectively. As these molecules have different electron counts, we got different energies for $E(Hc)$ and $E(Ha)$. We have considered the orthorhombic structure for Ga [30], rhombohedral structure for As [31] and hexagonal structure for both Cd [32] and Se [33] at their experimental lattice constants to evaluate the energies entering the expression for the formation energy. The chemical potentials μ_A and μ_B are determined by the criterion for stability of the bulk solids.

3.3 Results and Discussions

The underlying tetrahedral coordination of the bulk lattice was preserved while constructing the NCs. This has been observed in experiments [34] that probe the local structure. Further the bond lengths/lattice parameters have been found to be close to the bulk values [4, 35]. The passivated NCs have been found to capture this effect and do not show significant reconstructions [24]. They observed a reduction in bond length of only 1% from their bulk values at the surface of passivated NCs. The candidates chosen for our analysis have equal number of anions and cations in their bulk limit and one of the motivations was to examine whether this remains to be the case even in the nano regime. Two limiting scenarios of non-stoichiometric and stoichiometric NCs were considered as discussed earlier. To compare the relative stability of different structures, we calculated the formation energies per atom in each case. While the oscillatory behaviour in the relative stability for wurtzite vs. zincblende structures have been studied in terms of cohesive energy [36] under relaxations of surface atoms only, we carried out complete structural optimization at each volume in order to find the ground state structure and energy. These quantities were computed for limiting values of the chemical potentials, both cation rich as well as anion rich. This was done to examine if cation rich conditions would favour a cation rich surface. In our calculation we have studied both the experimental limits of excess amount of cations and anions left in the solution.

In order to examine the limiting case of a surface of a NC we consider the non-polar (110) as well as the polar (100) and (111) surfaces of CdSe in the zinc-blende structure(Figure 3.2). Details of surface calculations have been mentioned in the Methodology section. The surface atoms were passivated with pseudo-hydrogens in each case and the formation energy of each surface

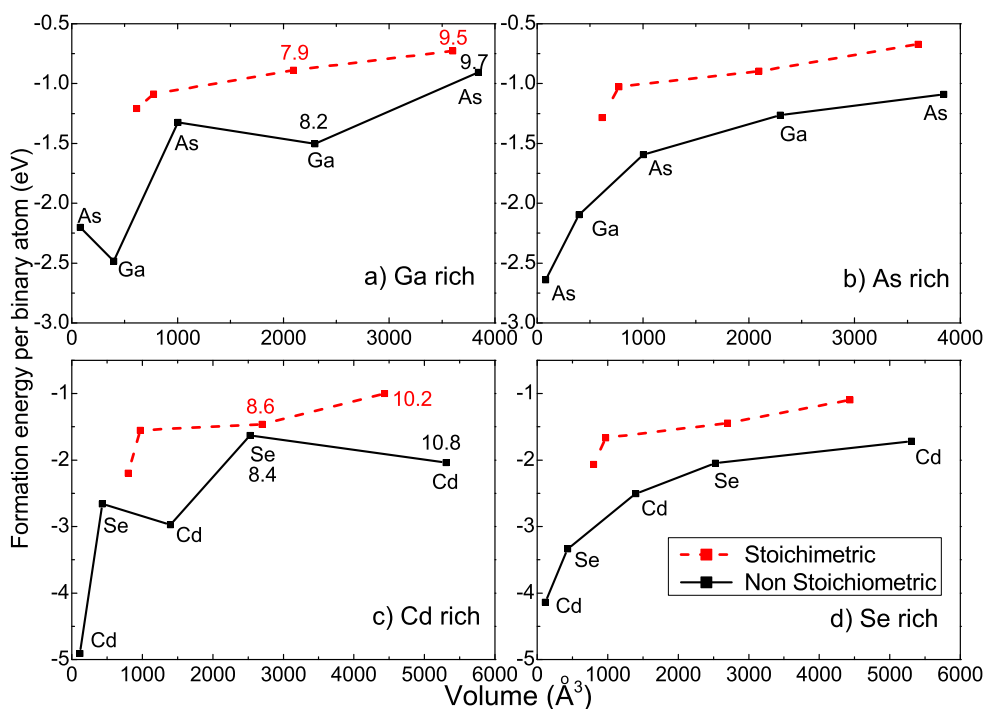


Figure 3.3: Variation of the formation energy per atom for the passivated NCs of GaAs and CdSe as a function of volume for the non-stoichiometric and stoichiometric NCs under cation-rich (panels a and c) and anion-rich (panels b and d) conditions. Radii of two largest, relaxed NCs have been shown inside the panel a) and c). Ga and Se atom lie at the centre of GaAs and CdSe NCs respectively. The type of atom that forms the outermost layer in the case of the non-stoichiometric NCs has been indicated. This has appeared in Ref. 37.

was calculated both with and without the passivating ligands. The formation energies per atom for passivated NCs of CdSe as well as GaAs are plotted in Figure 3.3 as a function of volume. The computed data points have been indicated with symbols and they have been joined with lines to serve as guides to the eye. Black points with solid lines and red points with dashed

lines correspond to the values of formation energy as a function of volume of the NCs for non-stoichiometric and stoichiometric NCs respectively. In both limits, the cation rich as well as the anion rich, one finds that the non-stoichiometric NCs are favoured over the stoichiometric ones. As the crystal size increases, the formation energies tend to become less negative. As a consequence of our definition of formation energy, one would expect the value to be zero at the infinite-sized limit where the bulk semiconductor is formed. These results suggest that as the crystal grows, one can have large deviations from the ideal stoichiometry of the bulk with several configurations Cd_nSe_m or Ga_nAs_m being realizable.

Two very different systems which were chosen for the study show very similar trends, reinforcing our idea about the generality of these results. Again, the choice of the central atom, as we have chosen Se and Ga as the central atom for CdSe and GaAs NCs respectively, does not change the trend of our result. The other limit that we consider is that of unpassivated NCs. Surprisingly, one finds that the stoichiometric NCs (as indicated by red points with dashed lines) are the ones favoured in almost the entire size regime (Figure 3.4 a, b, c, d) that we have studied. There are a few instances when the cation/ anion terminated non-stoichiometric NCs have similar or lower formation energy, but the trend seems to indicate stoichiometric NCs are more favourable in the absence of any passivant. The positive value of the formation energy of unpassivated NC suggests that they are unstable. However the stability could be modified by the presence of solvents, other ions present in the solution and other effects which have not been considered here. This comparison definitely indicates the role being played by passivants.

At this juncture we have compared these two limiting cases as the effect of two competing interactions. One is in between cations and passivants and

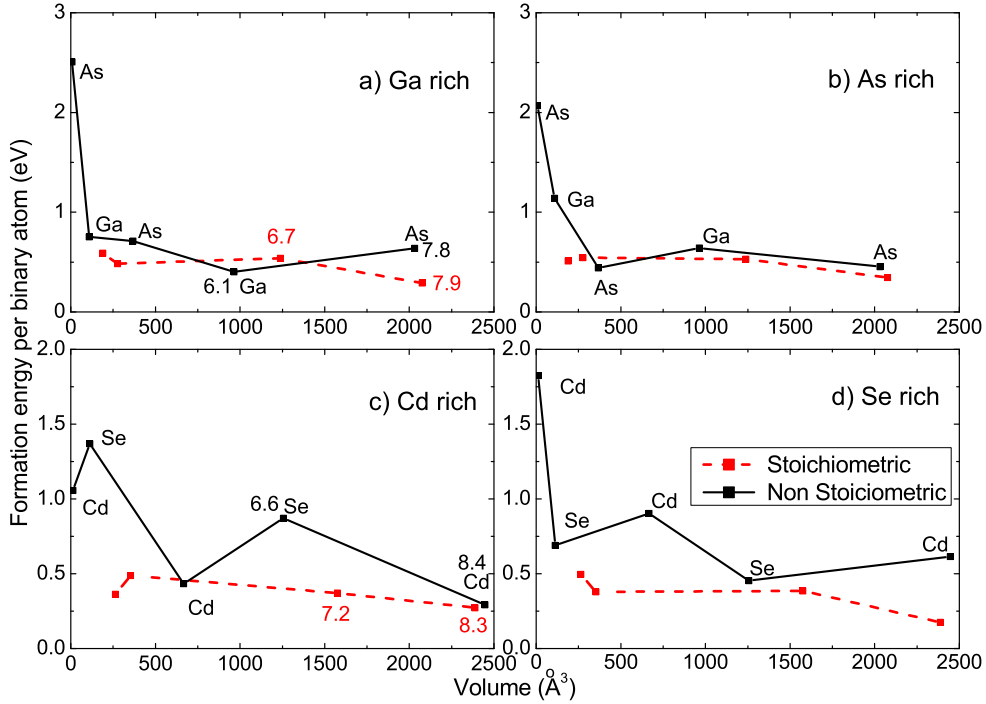


Figure 3.4: Variation of the formation energy per atom for the unpassivated binary NCs of GaAs and CdSe as a function of volume for the non-stoichiometric and stoichiometric crystals under cation-rich (panel a and c) and anion-rich (panel b and d) conditions. Radii of two largest, relaxed NCs have been shown inside the panel a) and c). Ga and Se atom lie at the centre of GaAs and CdSe NCs respectively. The type of atom that forms the outermost layer in the case of the non-stoichiometric NCs has been indicated. This has appeared in Ref. 37.

another is in between cations and anions as shown in the schematic diagram Figure 3.5. While the stronger value of the former interaction leads to a cation rich surface (Figure 3.5a), higher values of the latter interaction leads to an uncontrolled growth of NCs (Figure 3.5b). The question we then went on to ask was what was it about the passivant that allowed the highly non-

stoichiometric crystals to be favoured. One way to examine this is to plot the orbital projected partial density of states for the surface as well as the fully coordinated cations/ anions. This has been plotted for $l=4$, passivated, non-stoichiometric NC of CdSe in Figure 3.6. In panel (Figure 3.6a) the Se p partial density of states has been plotted for the Se atom at the core. Zero in these figures represents the valence band maximum. At the surface, one has Se atoms with different coordination and one finds that the singly coordinated Se atoms have their centroid of the partial density of states deeper (Figure 3.6c) than the two-fold coordinated Se atom at the surface (Figure 3.6b). It should be noted that although we say two-fold coordinated, we mean two-fold coordinated with Cd atoms while the other two bonds are formed with pseudo-hydrogens. The change in the centroid of the Se p partial density of states to deeper energies when the numbers of pseudo-hydrogens/ passivant atoms are more suggests strong interaction between the surface atoms and the passivants.

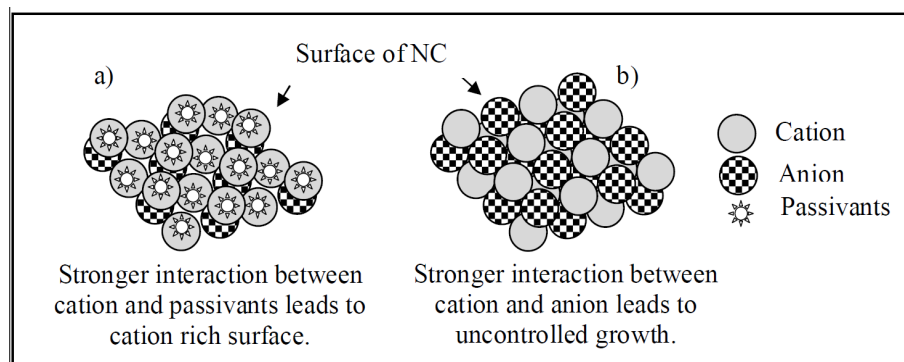


Figure 3.5: (a) If the interaction strength between cation and passivant is stronger than the interaction strength between cation and anion, a cation rich surface is favoured. (b) Stronger interaction between cation and anion leads to an uncontrolled growth of NC.

A similar behaviour of the partial density of states is seen for the Cd atoms also. The Cd s contribution to the partial density of states in the valence band is plotted in Figure 3.7 for the case of $l=5$, non-stoichiometric, passivated CdSe NC. The Cd s partial density of states associated with the layer next to the core of the NC (layer 1 in our nomenclature) is pushed deeper into the valence band depending on the number of passivant atoms coordinated to the surface Cd atom. This suggests similar strong interaction between the Cd atoms and the passivant.

Although the results plotted in Figure 3.6 and Figure 3.7 suggests strong interactions between the surface cations/ anions with the passivants, the question we asked is why should this favour the highly non-stoichiometric NCs over the stoichiometric ones. The answer for this found to be a consequence of the coordination of the surface atoms. The number of atoms with 1, 2, 3 and 4 fold coordination in each of the A_nB_m type of NCs is given in Table 3.1. Additionally the number of 1-fold and 2-fold coordinated A or B type of atoms in each case is given as a percentage of the total number of atoms. The number of under coordinated atoms seems to be significantly larger for the non-stoichiometric NCs than the stoichiometric ones. As we already pointed out that the under coordinated atoms had the centroid of the partial density of states deeper indicating a larger energy gain from the interaction of the surface atoms with the passivants, the non-stoichiometric NCs were favoured for the passivated case considered.

In order to examine this aspect more carefully we considered the (100), (110) and the (111) surfaces of CdSe and calculations for the formation energy were performed both in the presence and absence of passivants. The values are given in Table 3.2.

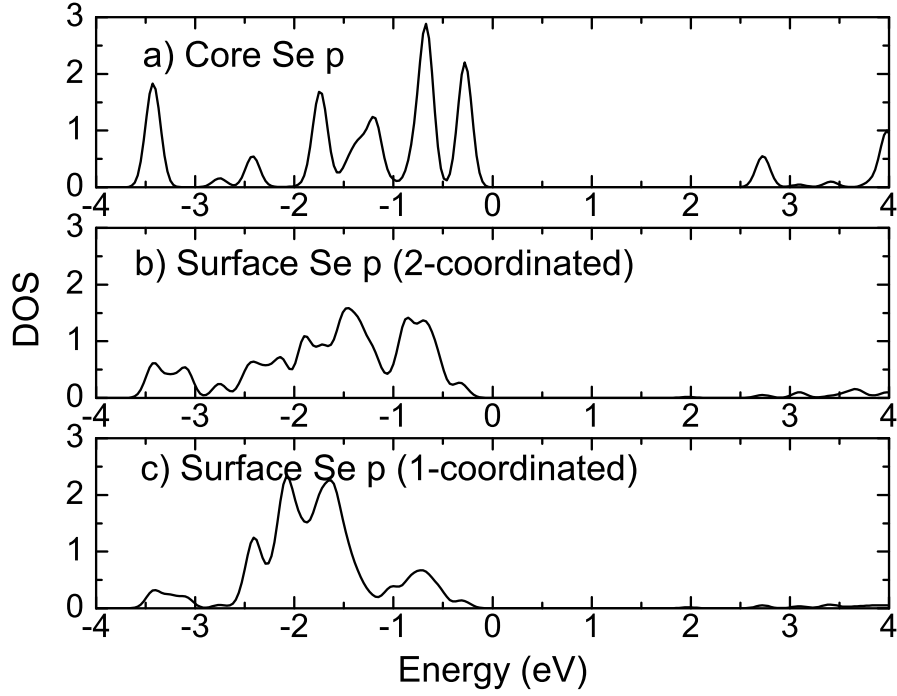


Figure 3.6: The Se p projected partial density of states ($l=4$, non-stoichiometric and passivated NC) for a Se atom at (a) the core as well as at the surface having (b) double and (c) single coordination with Cd atoms. The zero of energy corresponds to the valence band maximum. This has appeared in Ref. 37.

Surface	Passivated	Unpassivated
(100)	-0.520	0.166
(110)	-0.469	0.068
(111)	-0.517	0.070

Table 3.2: Formation energies corresponding to different passivated as well as unpassivated surfaces of CdSe.

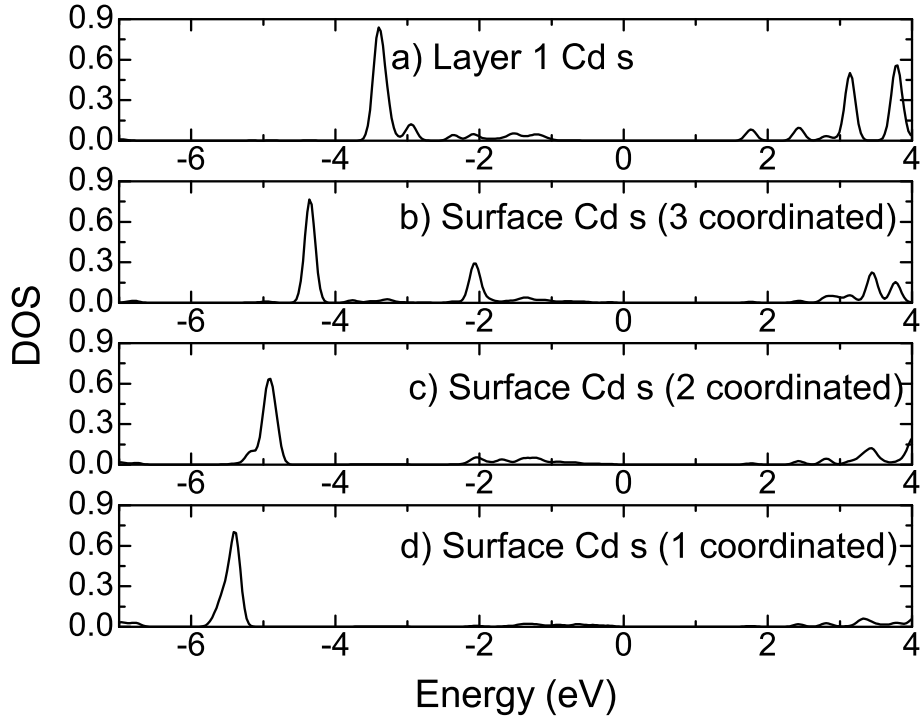


Figure 3.7: The Cd s projected partial density of states ($l=5$, non-stoichiometric and passivated NC) for a Cd atom (a) in the first layer as well as at the surface having (b) triple, (c) double and (d) single coordination with the Se atoms. The zero of energy corresponds to the valence band maximum. This has appeared in Ref. 37.

In every case we find that the passivated surface is stabilized more because of the interaction with the passivants. Further, the interaction with the passivants is found to significantly stabilize the more polar surface (100) and (111). This is consistent with the observations of Soni et al. [20]. The coordination of the surface atom is given in each case for the different surfaces one has for zincblende structures in Table 3.3. The polar surfaces are found

to be significantly under coordinated supporting the result of highly non-stoichiometric surfaces being favoured.

Surface	(100)	(110)	(111)
Coordination #	2	3	1,3

Table 3.3: Surface coordination numbers corresponding to atoms on different surfaces.

The passivants used in the present case are pseudohydrogens which do not have several features that the bulky organic ligands used in experiments have. However, they serve as a guiding principle and suggest that one could use passivants to manipulate the surface stoichiometry. Recent studies [38] have shown that the bulky ligands can be replaced by small inorganic functional groups and the properties of the NCs remain largely unchanged. Further the work by Puzder et al. [39] suggests that a significant part of the binding energy of the passivant with the NC surfaces emerges from the end-element attached to the surface atoms. These observations support the use of small atoms, suggesting that the steric effects associated with larger organic ligands may not play such an important role. Currently one has good passivants only for the cations and not the anions. So, by suitably changing the strength of the passivant, one could have a cation-rich surface which would have a stronger efficiency for band edge optical transitions. Soni et al. [19,20] have studied the coverage of CdSe surfaces in experiments using metal oleate passivants. They find using atomic absorption spectroscopy that the Cd coverage at the surface cannot be increased beyond a point in spite of having a high concentration of Cd precursors. So, the present calculations suggest a possible route of how this could be possible.

3.4 Conclusion

In this work we have shown that passivating ligands introduced during the growth of NCs have a significant role in determining the surface stoichiometry of binary semiconductor NCs. While in the past, their roles had been identified as removing dangling bond states as well as preventing agglomeration of NCs during growth, in this present work we show that the strong interaction between the surface atoms of the NC and the passivant could lead to the passivant determining the surface stoichiometry. Considering two typical examples of binary semiconductors- one, a III V compound, GaAs, while the other, a II VI compound, CdSe, we find that highly non-stoichiometric NCs are favoured in both cases in the presence of strongly interacting passivants. The results are additionally supported by calculated results on various surfaces of CdSe that were considered.

Part of this work is continued from [37] for the completeness.

Bibliography

- [1] A. P. Alivisatos, Semiconductor Clusters, Nanocrystals, and Quantum Dots, *Science*, **271**, 933 (1996).
- [2] A. P. Alivisatos, Perspectives on the Physical Chemistry of Semiconductor Nanocrystals, *J. Phys. Chem.* **100**, 13226 (1996).
- [3] Y. Cui, Q. Wei, H. Park, C. M. Lieber, Nanowire Nanosensors for Highly Sensitive and Selective Detection of Biological and Chemical Species, *Science* **293**, 1289 (2001).
- [4] (a) C. B. Murray, D. J. Norris, M. G. Bawendi, Synthesis and Characterization of Nearly Monodisperse CdE (E = sulfur, selenium, tellurium) Semiconductor Nanocrystallites, *J. Am. Chem. Soc.* **115**, 8707 (1993)
(b) D. V. Talapin, A. L. Rogach, A. Kornowski, M. Haase, H. Weller, Highly Luminescent Monodisperse CdSe and CdSe/ZnS Nanocrystals Synthesized in a HexadecylamineTrioctylphosphine OxideTrioctylphosphine Mixture, *Nano Lett.* **1** 207 (2001).
- [5] X. Michalet, F. F. Pinaud, L. A. Bentolila, J. M. Tsay, S. Doose, J. J. Li, G. Sundaresan, A. M. Wu, S. S. Gambhir, S. Weiss, Quantum Dots for Live Cells, in Vivo Imaging, and Diagnostics, *Science* **307**, 538 (2005).

- [6] N. Tessler, V. Medvedev, M. Kazes, S. Kan, U. Banin, Efficient Near-Infrared Polymer Nanocrystal Light-Emitting Diodes, *Science* **295**, 1506 (2002).
- [7] T. L. Chan, H. Kwak, J. H. Eom, S. B. Zhang, J. R. Chelikowsky, Self-purification in Si Nanocrystals: An Energetics Study, *Phys. Rev. B* **82**, 115421 (2010).
- [8] A. Nag, R. Cherian, P. Mahadevan, A. V. Gopal, A. Hazarika, A. Mohan, A. S. Vengurlekar, D. D. Sarma, Size-Dependent Tuning of Mn²⁺ d Emission in Mn²⁺-Doped CdS Nanocrystals: Bulk vs Surface, *J. Phys. Chem. C* **114**, 18323 (2010).
- [9] R. Viswanatha, D. Naveh, J. R. Chelikowsky, L. Kronik, D. D. Sarma, Magnetic Properties of Fe/Cu Codoped ZnO Nanocrystals, *J. Phys. Chem. Lett.* **3**, 2009 (2012).
- [10] M. M. G. Alemany, L. Tortajada, X. Huang, M. L. Tiago, L. J. Gallego, J. R. Chelikowsky, Role of Dimensionality and Quantum Confinement in p-type Semiconductor Indium Phosphide Quantum Dots, *Phys. Rev. B* **78**, 233101 (2008).
- [11] (a) G. Kalyuzhny, R. W. Murray, Ligand Effects on Optical Properties of CdSe Nanocrystals, *J. Phys. Chem. B* **109**, 7012 (2005), (b) C. Bullen, P. Mulvaney, The Effects of Chemisorption on the Luminescence of CdSe Quantum Dots, *Langmuir* **22**, 3007 (2006).
- [12] A. Nag, A. Hazarika, K. V. Shanavas, S. M. Sharma, I. Dasgupta, D. D. Sarma, Crystal Structure Engineering by Fine-Tuning the Surface Energy: The Case of CdE (E = SSe) Nanocrystals, *J. Phys. Chem. Lett.* **2**, 706 (2011).

- [13] J. Jasieniak, C. Bullen, J. van Embden, P. Mulvaney, Phosphine-Free Synthesis of CdSe Nanocrystals, *J. Phys. Chem. B* **109**, 20665 (2005).
- [14] O. Chen, Y. Yang, T. Wang, H. Wu, C. Niu, J. Yang, Y. C. Cao, Surface-Functionalization-Dependent Optical Properties of IIVI Semiconductor Nanocrystals, *J. Am. Chem. Soc.* **133**, 17504 (2011).
- [15] R. Viswanatha, H. Amenitsch, D. D. Sarma, Growth Kinetics of ZnO Nanocrystals: A Few Surprises, *J. Am. Chem. Soc.* **129**, 4470 (2007).
- [16] P. Crespo, R. Litran, T. Rojas, M. Multigner, J. De la Fuente, J. Sanchez-Lopez, M. Garcia, A. Hernando, S. Penades, A. Fernandez, Permanent Magnetism, Magnetic Anisotropy, and Hysteresis of Thiol-Capped Gold Nanoparticles, *Phys. Rev. Lett.* **93**, 87204 (2004).
- [17] X. Peng, L. Manna, W. Yang, J. Wickham, E. Scher, A. Kadavanich, A. P. Alivisatos, Shape Control of CdSe Nanocrystals, *Nature*, **404**, 59 (2000).
- [18] K. Akamatsu, T. Tsuruoka, H. Nawafune, Band Gap Engineering of CdTe Nanocrystals Through Chemical Surface Modification, *J. Am. Chem. Soc.* **127**, 1634 (2005).
- [19] J. Jasieniak, P. Mulvaney, From Cd-Rich to Se-Rich the Manipulation of CdSe Nanocrystal Surface Stoichiometry, *J. Am. Chem. Soc.* **129**, 2841 (2007).
- [20] U. Soni, S. Sapra, The Importance of Surface in CoreShell Semiconductor Nanocrystals, *J. Phys. Chem. C* **114**, 22514 (2010).
- [21] C. Y. Yeh, Z. W. Lu, S. Froyen, A. Zunger, Predictions and systematizations of the zinc-blendewurtzite structural energies in binary octet compounds, *Phys. Rev. B* **45**, 12130 (1992).

- [22] K. Shiraishi, A New Slab Model Approach for Electronic Structure Calculation of Polar Semiconductor Surface, *J. Phys. Soc. Japan* **59**, 3455 (1990).
- [23] A. Hazarika, A. Layek, S. De, A. Nag, S. Debnath, P. Mahadevan, A. Chowdhury, D. D. Sarma, Ultranarrow and Widely Tunable Mn²⁺-Induced Photoluminescence from Single Mn-Doped Nanocrystals of ZnS-CdS Alloys, *Phys. Rev. Lett.* **110**, 267401 (2013), (b) N. S. Norberg, G. M. Dalpian, J. R. Chelikowsky, D. R. Gamelin, Energetic Pinning of Magnetic Impurity Levels in Quantum-Confined Semiconductors, *Nano Lett.* **6**, 2887 (2006).
- [24] R. Cherian, P. Mahadevan, Size dependence of Lattice Constants of Semiconductor Nanocrystals, *App. Phys. Lett.* **92**, 043130 (2008).
- [25] G. Kresse, J. Furthmuller, Efficient Iterative Schemes for ab initio Total-Energy Calculations Using a Plane-Wave Basis Set, *Phys. Rev. B* **54**, 11169 (1996).
- [26] G. Kresse, J. Furthmuller, Efficiency of ab-initio Total Energy Calculations for Metals and Semiconductors Using a Plane-Wave Basis Set, *Comp. Mat. Sci.* **6**, 15 (1996).
- [27] G. Kresse, D. Joubert, From Ultrasoft Pseudopotentials to the Projector Augmented-Wave Method, *Phys. Rev. B* **59**, 1758 (1999).
- [28] R. Cherian, P. Mahadevan, Bulk and Nanoscale GaN: Role of Ga d States, *Phys. Rev. B* **76**, 075205 (2007).
- [29] J. P. Perdew, Y. Wang, Accurate and Simple Analytic Representation of the Electron-gas Correlation Energy, *Phys. Rev. B* **45**, 13244 (1992).

- [30] B. D. Sharma, J. Donohue, A Refinement of the Crystal Structure of Gallium, *Z. Kristal.* **177**, 293 (1962).
- [31] D. Schiferl, C. S. Barrett, The Crystal Structure of Arsenic at 4.2, 78 and 299K, *J. App. Cryst.* **2**, 30 (1969).
- [32] E. R. Jette, F. Foote, Precision Determination of Lattice Constants, *J. Chem. Phys.* **3**, 605 (1935).
- [33] P. Unger, P. Cherin. The Crystal Structure of Trigonal Selenium, *Inorg. Chem.* **6**, 1589 (1967).
- [34] M. A. Marcus, L. E. Brus, C. Murray, M. G. Bawendi, A. Prasad, A. P. Alivisatos, EXAFS Studies of Cd Chalcogenide Nanocrystals, *Nanostruct. Mat.* **1**, 323 (1992).
- [35] (a) N. Herron, J. C. Calabrese, W. E. Farneth, Y. Wang, Crystal Structure and Optical Properties of $\text{Cd}_{32}\text{S}_{14}(\text{SC}_6\text{H}_5)_{36}\cdot\text{DMF}_4$, a Cluster With a 15 Angstrom CdS Core, *Science* **259**, 1426 (1993), (b) A. C. Carter, C. E. Bouldin, K. M. Kemner, M. I. Bell, J. C. Woicik, S. A. Majetich, Surface Structure of Cadmium Selenide Nanocrystallites, *Phys. Rev. B* **55**, 13822 (1997).
- [36] S. Datta, M. Kabir, T. Saha-Dasgupta, D. D. Sarma, First-Principles Study of Structural Stability and Electronic Structure of CdS Nanoclusters, *J. Phys. Chem. C* **112**, 8206 (2008).
- [37] R. Cherian, Thesis: Structural and Electronic Properties of Semiconductors: Bulk and Nanoscale, University of Calcutta, (2009).
- [38] A. Nag, D. S. Chung, D. S. Dolzhenkov, N. M. Dimitrijevic, S. Chattopadhyay, T. Shibata, D. V. Talapin, Effect of Metal Ions on Photoluminescence, Charge Transport, Magnetic and Catalytic Properties

- of All-Inorganic Colloidal Nanocrystals and Nanocrystal Solids, *J. Am. Chem. Soc.* **134**, 13604 (2012).
- [39] A. Puzder, A. J. Williamson, N. Zaitseva, G. Galli, L. Manna, A. P. Alivisatos, The Effect of Organic Ligand Binding on the Growth of CdSe Nanoparticles Probed by Ab Initio Calculations, *Nano Lett.* **4**, 2361 (2004).

Chapter 4

Optical Transition in Mn doped Semiconducting Nanocrystals

4.1 Introduction

Luminescent semiconducting nanocrystals (NCs) have attracted considerable attention in recent years as potential candidate for light emission diodes. The advantage of these NCs over conventional fluorescent materials is the ability to tune emission energy by changing the NC diameter only. Excellent colour reproduction and very bright emission energy are also the added advantages. But the problem with these NCs is the self absorption of emitted photon [1, 2] by other NCs in the ensemble which leads to drastic fall in the overall emission yield. This problem can be avoided in another type of NCs where the optical emission involves dopant state only [3, 4]. In the excitation process, an electron from the host site is excited first. The energy is then non-radiatively transferred to the dopant state followed by the radiative deexcitation involving dopant states only. However the condition for

such mechanism to work is constrained by the fact that the host band gap should be more than the dopant energy level gap. Undoubtedly Mn doped semiconducting NCs have been examined extensively for such application. But as the radiative transition involves states coming from atomic like Mn d states only, these NCs lack the ability to vary the emission energy with the variation of NCs diameter. Indeed experimental evidences show no or very small tunability [5–8] associated with such transition in Mn doped NCs. Another problem with Mn d emission from such doped NCs is the finding of large spectral width associated with such transition. This is inconsistent with the fact that atomic like 4T_1 - 6A_1 Mn emission should be very sharp in nature. However experimental reports find the line width to be of the order of 200 meV [10]. There are early attempts to explain this ambiguity and it was attributed to the strong coupling between electronic states coming from Mn d levels and acoustic vibration of the host material [10]. However such explanation fails to address the issue of considerably larger spectral width than even found in doped bulk semiconductors [11, 12].

Recently these long standing problems have been addressed successfully. Spatially resolved optical emission data from individual doped NC [9] have shown that a wide range of tunable colours from these Mn doped NCs are also possible. This arises from the fact that the ligand field strength varies at different symmetry inequivalent sites occupied by Mn ions. The significantly distorted ligand field near the surface gives rise to very different transition energy than that from core doped NCs and one can tune emission peak over 370 meV. Contrary to the earlier results they also have found the emission from individual doped NC to be very narrow and the anomaly in the large linewidth was found to arise from the contribution adding up from multiple excitonic sites in the ensemble [9]. Despite all these efforts it remains unclear, why does such Mn emission remain atomic like? Mn d levels are expected to interact

with nearby anionic states and as these interaction strengths change with material one expects different emission energies. However experiments show that the emission is largely independent of the chemical nature of the host NC. In this chapter, with the help of density functional theory calculations we have addressed the issue. Considering doping at two inequivalent cationic sites near the core of NC we are able to capture the experimental findings of invariant transition energy. Moreover we have considered two different host materials CdS and CdSe and substituted one cationic site with Mn ion. Despite of having huge difference in Mn-anion bond lengths in these two systems, emission energies are found to be very similar. Analysis of the density of states(DOS) coming from Mn and nearby host anionic sites reveal that there is substantial interaction between them. However the interaction normalizes in such a way that the relative position of interacting states remain fixed. Moreover there are changes in Hund's coupling strength and crystal field strength with the change of host materials but the magnitude of change in these energetic are very similar which results in the invariant transition energy.

4.2 Methodology

We follow the methodology as detailed in section 3.2 to generate non-stoichiometric passivated NCs of CdS from its wurtzite bulk structure. For present calculations a cation terminated CdS nanocrystal with diameter of 18 Å was generated. 50% cationic sites have been substituted randomly with Zn to form alloy of $\text{Zn}_{48}\text{Cd}_{48}\text{S}_{57}$. One of the cationic positions near the core is chosen and has been substituted with Mn ion to generate doped NC. Figure 4.1 shows our first core doped NC. Two inequivalent cationic positions

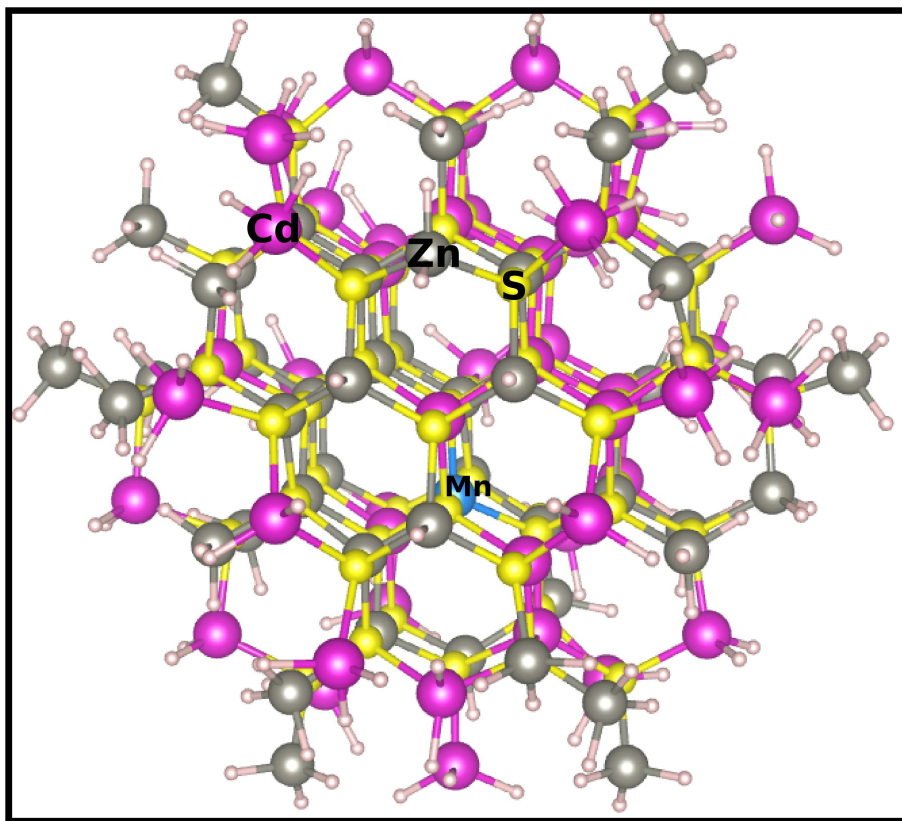


Figure 4.1: Relaxed non-stoichiometric NC of $\text{MnZn}_{47}\text{Cd}_{48}\text{S}_{57}$.

near the core of the NC were considered. First principle electronic structure calculations have been performed with VASP [13,14] which involves a plane-wave projector augmented wave (PAW) [15] implementation of the density functional theory. We have used generalized gradient approximation to the exchange correlation functional [16]. All calculations have been performed at gamma point only. An energy cutoff of 350 eV has been set for the kinetic energy part of the plane waves included in the basis. Internal positions were relaxed until an energy convergence of 10^{-5} eV along with the force convergence of $5 \text{ meV}/\text{\AA}$ achieved. To further analyze the optical transition in the dilute limit we have used bulk supercells of host semiconducting materials and have substituted one cationic position with Mn ion. Two different

semiconductors CdS and CdSe have been chosen to analyze the scenario of doping different host materials with very different Mn-anion bond lengths. All calculation details are similar to the case of earlier calculations however a Monkhorst-Pack k points grid of $6 \times 6 \times 6$ have been used here.

4.3 Results and Discussions

Experimental evidences of optical emission from Mn doped NCs show a well defined peak near 580 nm region [17–20]. This peak is independent of the size and even the chemical nature of host NCs. To explore such optical transition we started with the NCs of CdS. A well-known difficulty of probing optical transition from Mn doped CdS NC is the strong overlap of the emission arising from the surface of the host with the Mn emission. However this can be avoided by the means of forming alloy of ZnS and CdS [9]. To mimic such scenario we have formed non-stoichiometric NCs of $\text{Zn}_{48}\text{Cd}_{48}\text{S}_{57}$ and substituted one cationic position near the core to generate doped NC. The energy minimization leads to a structure where Mn-S bond lengths are found to be 2.33, 2.33, 2.34 and 2.35 Å. Doping in another inequivalent cationic position near the core generates another structure where relaxed Mn-S bond length are found to be 2.34, 2.35, 2.35 and 2.36 Å.

In tetrahedral environment of S ions, Mn d orbital splits into doubly degenerate e and triply degenerate t_2 levels. In the ground state, Mn +2 ion with five unpaired electrons occupy all of the majority spin levels with e and t_2 symmetry and all minority spin channels remain unoccupied. However in the first excited state one electron of the highest occupied t_2 orbitals is transferred to minority spin e electron (this outwardly spin-forbidden transition is allowed because of the finite spin-orbit coupling strength). Such d-d transi-

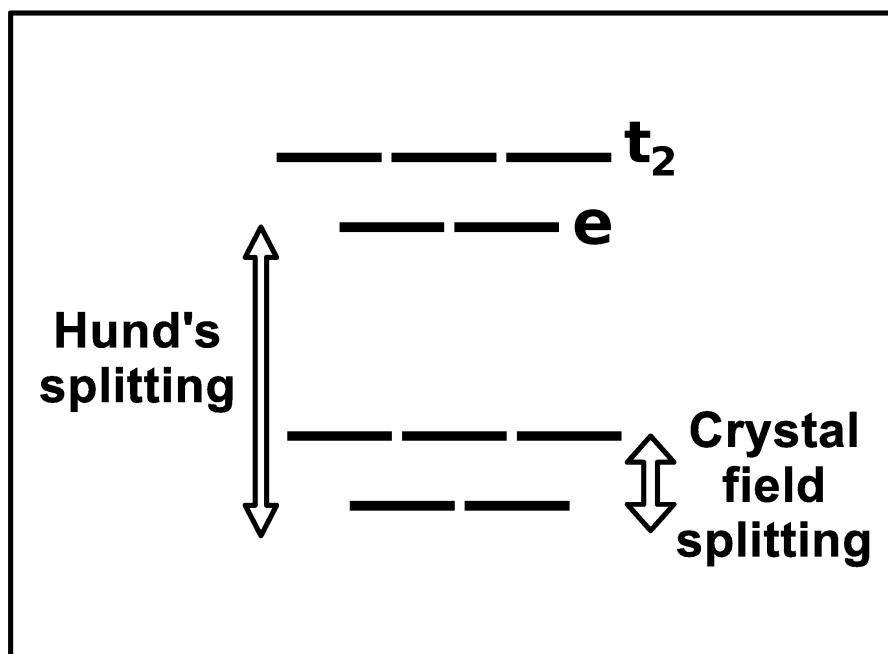


Figure 4.2: Hund's splitting and crystal field splitting in tetrahedral environment. d-d transition energy has been calculated from their values.

tion energy from the first excited state to the ground state can be expressed in terms of Hund's coupling strength(J_h) and crystal field splitting(Δ). As Mn is in high spin state, the splitting between majority and minority energy levels with identical symmetry is given by $4J_h$. Considering the crystal field splitting(Δ) between t_2 and e orbitals, d-d transition energy can be computed as $4J_h - \Delta$. Figure 4.2 explains the transition energy in tetrahedral environment. Any distortion in the local environment should further remove the degeneracy and looking at the DOS contributed by the Mn d states near the Fermi energy, as shown in Figure 4.3, we found a small but finite energy splitting in the t_2 and e levels. Moreover, the splitting in the t_2 states is larger than in the e levels. Despite this additional symmetry removal, the transition energy corresponding to first(Core 1) and second(Core

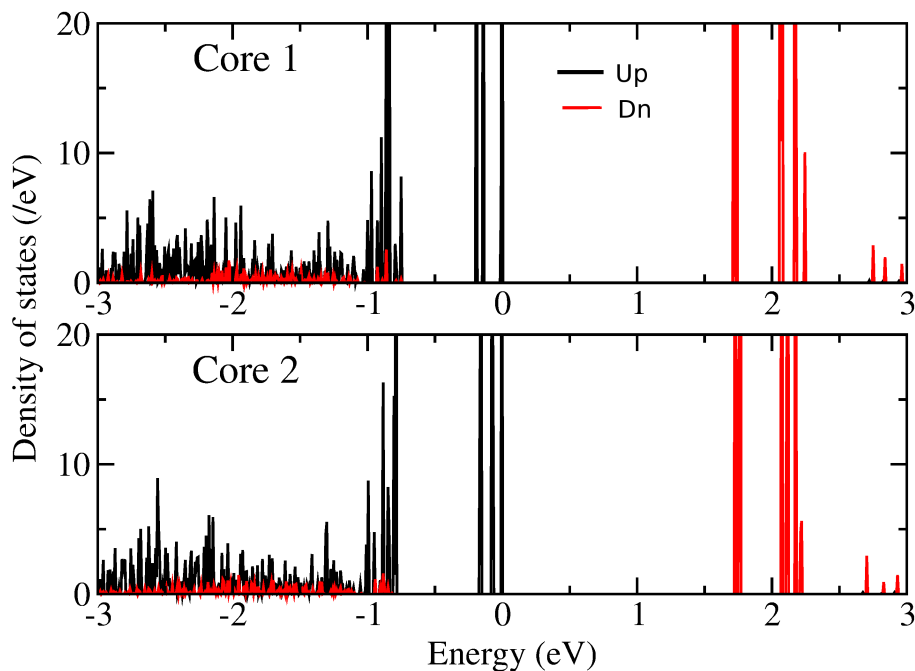


Figure 4.3: Density of states corresponding to Mn d states in Mn doped NC alloys. Two inequivalent cationic doping positions were chosen while constructing the structures.

2) structures are found to be 1.89 eV and 1.90 eV respectively. This invariable transition energy from two inequivalent sites are indicative of an atomic like transition from Mn d states. However very similar bond lengths in two inequivalent positions could be responsible for such similar emission energy.

In the local environment of S ions, one expects finite interaction between Mn d and S p levels and any change in such environment should also reflect in the change in transition energy. To check whether there is any such interaction between Mn and neighbouring anions in the doped structure, we have explored the bulk structure with dilute doping concentration. A supercell comprising of sixty four atoms have been generated and one cationic position has been replaced with Mn atom to form $\text{MnCd}_{31}\text{S}_{32}$. Figure 4.4 shows

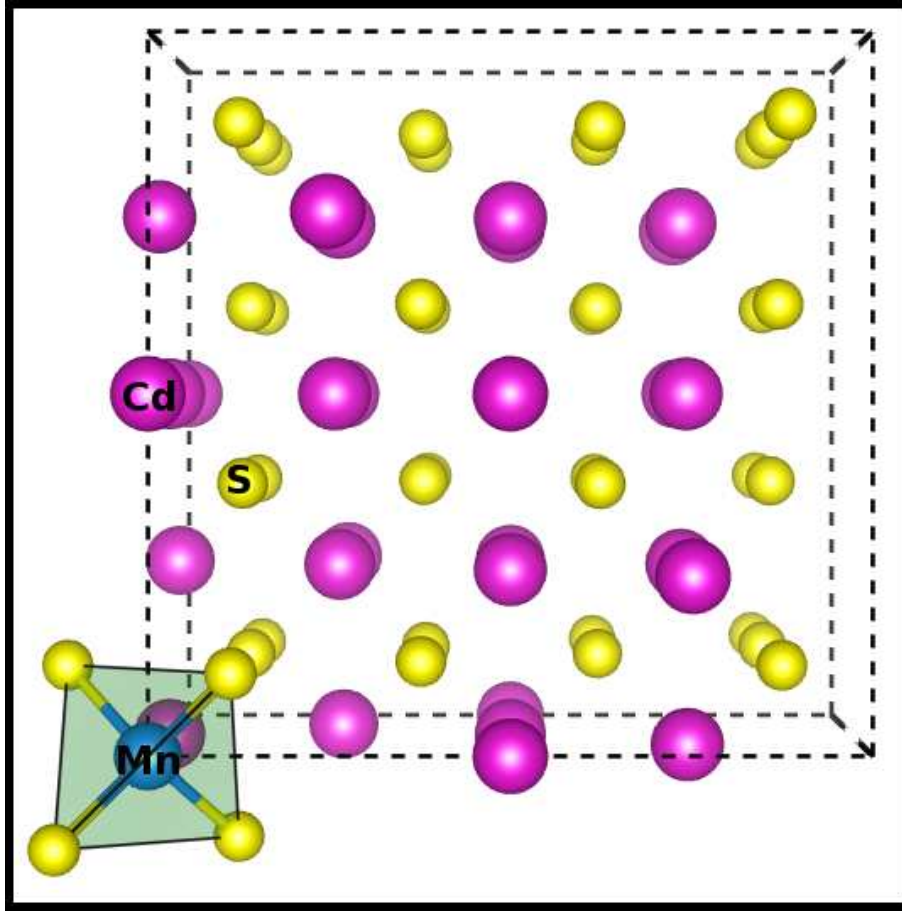


Figure 4.4: Crystal structure of a representative unit cell of Mn doped CdS.

the crystal structure of a representative cell of Mn doped CdS. For simplicity we also have shown the MnS_4 tetrahedra. A complete structural relaxation leads to a structure where Mn-S bond lengths are found to be 2.37 Å. To check the interaction between Mn d and S p states, we have plotted spin and orbital projected DOS for Mn d and S p states in Figure 4.5. Zero in these figures represents the valence band maximum (VBM). Peaks near the VBM are mainly contributed by the Mn d states with t_2 symmetry. However significant hybridization between Mn d and S p induces finite contribution from the S p levels also. In a two band bonding and anti-bonding model, as

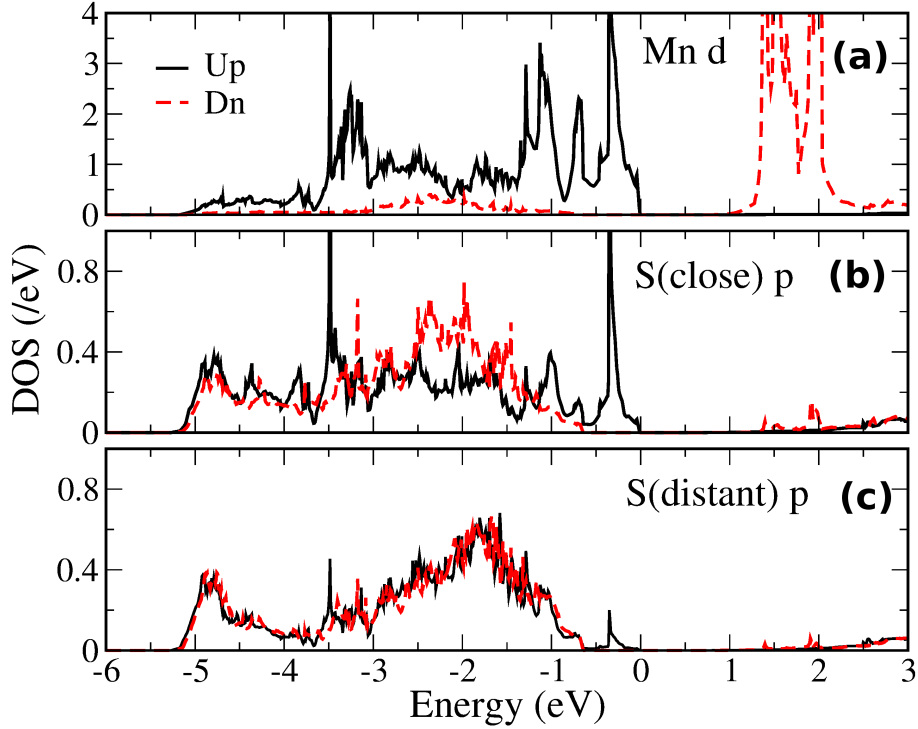


Figure 4.5: Spin and orbital projected density of states of Mn d and S p states in $\text{MnCd}_{31}\text{S}_{32}$.

shown in Figure 4.6, this level can be attributed to the anti-bonding state with major contribution from Mn d levels. The conjugate bonding states are around 3.5 eV below the VBM. Moreover the interaction between Mn d and neighbouring S p majority spin channels induces spin polarization even in the S p states. Further, we have plotted charge density (Figure 4.7) within an energy window of 0.5 eV below the VBM to show the admixing between Mn d and S p states. Comparing the DOS in a distant S atom (shown in panel c of Figure 4.5) we found all these features to be absent and the main contribution lies near 2 eV below the Fermi energy. All these results confirm our prediction about the strong interaction between Mn and neighbouring anions.

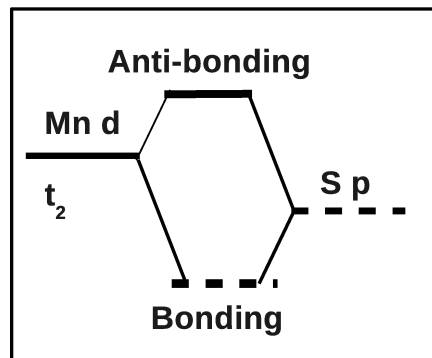


Figure 4.6: Bonding and anti-bonding levels coming from interaction between Mn d and S p.

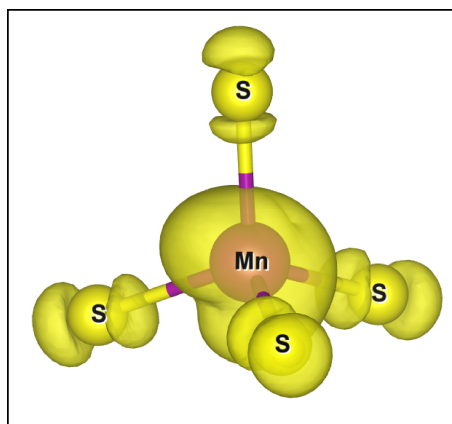


Figure 4.7: Charge density plot within an energy window of 0.5 eV below the Fermi level shows the covalency between Mn d and S p states.

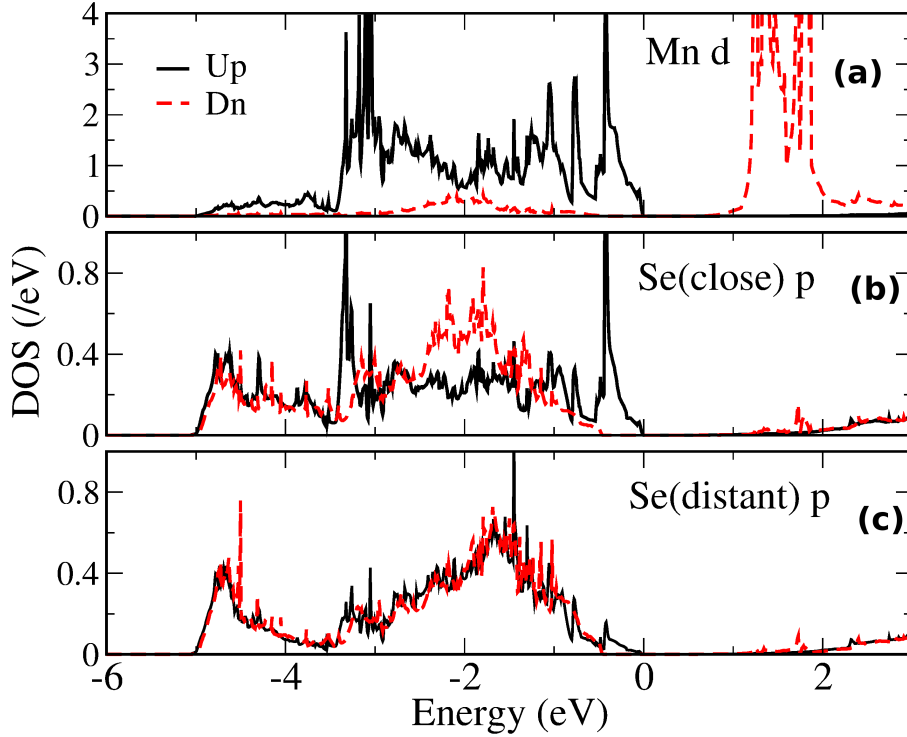


Figure 4.8: Spin and orbital projected density of states of Mn d and Se p states in $\text{MnCd}_{31}\text{Se}_{32}$.

To check the scenario in another tetrahedral environment but with very different Mn-anion bond lengths, we have considered the case of CdSe host material. Similar to the earlier structure a supercell of CdSe consisting of sixty four atoms have been generated and one cationic position has been replaced with Mn to form $\text{MnCd}_{31}\text{Se}_{32}$. In completely relaxed structure, Mn-Se bond lengths are found to be 2.55 \AA which is significantly larger than Mn-S bond lengths in doped CdS. Despite this huge difference in bond lengths, features of the DOS (Figure 4.8) remain unchanged. Main contribution near the VBM is mainly coming from Mn d orbitals with t_2 symmetry and the significant admixing between Mn d and nearby Se p states in the majority spin states are also evident from the DOS. Moreover the relative position

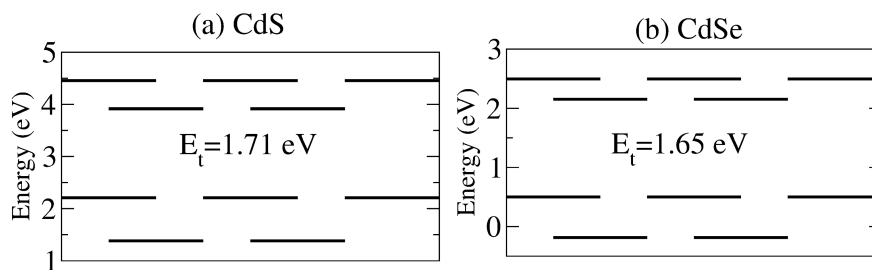


Figure 4.9: Optical transition energy in Mn doped (a)CdS and (b)Mn doped CdSe, calculated from the energy eigenvalues at the gamma point.

of bonding/anti-bonding levels remain fixed, indicating a very similar interaction strength. This result is apparently violating Harrison's scaling law which predicts a decrease in p-d interaction strength with the increase in bond length. However one should note that as one moves from 2p to 3p orbital, the spatial extent of delocalized p orbitals increases further and one can feel the effect of delocalized orbitals from a larger distance. This effect compensates for the change in interaction due to larger bond length and the effective interaction strength remains unaltered.

To arrive at energy level diagrams for Mn 3d levels, eigen vectors corresponding to different eigenvalues at the gamma point have been analyzed for their symmetry. Such level diagram for Mn d levels in doped CdS has been shown in the Figure 4.9(a) with energy plotted along Y axis. Hund's field splitting between levels with e symmetry and the crystal field splitting in the occupied Mn d levels have been found to be 2.51 eV and 0.80 eV respectively. This results in a Mn d transition energy of 1.71 eV in doped CdS structure. A similar energy eigenvalue analysis for Mn d levels in doped CdSe (Figure 4.9(b)) indicates that there are reduction in both Hund's splitting as well as crystal field splitting compared to the earlier case. Hund's field splitting and crystal field splitting are found to be 2.34 eV and 0.69 eV respectively. How-

ever the reduction in both energetic are almost same which results in a very similar transition energy of 1.65 eV.

4.4 Conclusion

We have investigated optical transition in Mn doped semiconducting NCs within density functional theory. Contrary to the earlier belief, we have shown that Mn d levels interact significantly with neighbouring anionic p states leading to occupied bonding and anti-bonding levels. Despite the strong interaction between Mn d and nearby anionic states, the relative positions of these two levels remain independent of local environment. The spatial extension of 3p orbitals are fairly larger than that of 2p orbital. This compensates for the change in interaction due to larger Mn-anion bond lengths and the effective interaction remains unaltered. Moreover, analyzing the Mn d energy level diagram at gamma point, we found a decrease in Hund's field splitting as well as crystal field splitting while going from $\text{MnCd}_{31}\text{S}_{32}$ to $\text{MnCd}_{31}\text{Se}_{32}$. However the change in both energetic are almost same resulting very similar optical transition energy in both the cases.

Bibliography

- [1] A. Nag and D.D. Sarma, J. Phys. Chem. C, **111**, 13641 (2007).
- [2] M. J. Bowers, J. R. McBride and S. J. Rosenthal, J. Am. Chem. Soc., **127**, 15378 (2005).
- [3] R. N. Bhargava, D. Gallagher, X. Hong and A. Nurmikko, Phys. Rev. Lett., **72**, 416 (1994).
- [4] A. A. Bol and A. Meijerink, Phys. Rev. B, **58**, R15997 (1998).
- [5] R. Zeng, T. Zhang, G. Dai and B. Zou, J. Phys. Chem. C, **115**, 3005 (2011).
- [6] A. Nag, R. Cherian, P. Mahadevan, A. V. Gopal, A. Hazarika, A. Mohan, A. S. Vengurlekar and D. D. Sarma, J. Phys. Chem. C, **114**, 18323 (2010).
- [7] N. Pradhan and X. Peng, J. Am. Chem. Soc., **129**, 3339 (2007).
- [8] S. Ithurria, P. Guyot-Sionnest, B. Mahler and Benoit Dubertret, Phys. Rev. Lett., **99**, 265501 (2007).
- [9] A. Hazarika, A. Layek, S. De, A. Nag, S. Debnath, P. Mahadevan, A. Chowdhury and D. D. Sarma, Phys. Rev. Lett., **110**, 267401 (2013).

- [10] R. Beaulac, P.I. Archer, S.T. Ochsenein and D.R. Gamelin, *Adv. Funct. Mater.*, **18**, 3873 (2008).
- [11] D. Langer and S. Ibuki, *Phys. Rev.*, **138**, A809 (1965).
- [12] D.D. Thong and O. Goede, *Phys. Status Solidi B*, **120**, K145 (1983).
- [13] G. Kresse, J. Furthmuller, *Phys. Rev. B*, **54**, 11169 (1996).
- [14] G. Kresse, J. Furthmuller, *Comp. Mat. Sci.*, **6**, 15 (1996).
- [15] G. Kresse and D. Joubert, *Phys. Rev. B*, **59**, 1758 (1999).
- [16] J. P. Perdew, Y. Wang, *Phys. Rev. B*, **45**, 13244 (1992).
- [17] D. J. Norris, A. L. Efros, S. C. Erwin, *Science*, **319**, 1776 (2008).
- [18] N. S. Karan, D. D. Sarma, R. M. Kadam and Narayan Pradhan, *J. Phys. Chem, Lett.*, **1**, 2863 (2010).
- [19] D. J. Norris, N. Yao, F. T. Charnock and T. A. Kennedy, *Nano Lett.*, **1**, 3, (2001).
- [20] S. Acharya, D. D. Sarma, N. R. Jana and N. Pradhan, *J. Phys. Chem. Lett.*, **1**, 485 (2010).

Chapter 5

Ultrathin Films of CdS and the Polar Catastrophe Model

5.1 Introduction

Polar surfaces of oxides have received a lot of interest in recent times, spurred primarily by the good quality of oxide films which allowed unusual physics in this regime to be probed [1–3]. The field started more than thirty years ago with the observation of imperfect interfaces for lattice matched heterovalent semiconductors [4]. It was then realized that the interfaces of polar semiconductors can never be perfect and this is what led to strong intermixing of atoms. More recently with the ability to isolate single monolayers of graphene [5], the field of layered semiconductors has been rejuvenated. The inability to use graphene which is a zero band gap semiconductor in devices as we know them, has pushed the focus towards layered semiconductors such as MoS₂, MoSe₂, WSe₂ [2–5] etc.. Surprisingly, even ionic binary semiconductors which favour the wurtzite structure in the bulk have been found to

exist in the graphitic phase in the few monolayers limit with ZnO [10–12] as an example. This transformation is driven by electrostatic considerations, as even when the films of these materials were grown without any bias for the growth direction, the polar *c*-direction was favoured. This was traced to a transition to a graphitic phase which had no dipole moment associated with it [13]. One is familiar with sp^2 bonded phases among the first row elements and the compounds that they form. The natural question that followed was what happens to compounds formed by later row elements at the few monolayers limit. As structures not often encountered in the bulk are relatively abundant among nano materials [14], would we find examples of graphitic structures here?

In order to examine this aspect, we consider the example of a covalent semiconductor, CdS. As the wavefunction should be more extended here and ionic charge effect considerably less pronounced, the question we asked was whether similar considerations that drove the favoured structures in the ionic limit would be operational here. Interestingly we do find a graphitic phase to be stable for 2% strained monolayer CdS, while the unstrained films favour a buckled structure. Transformation to an sp^2 bonded phase is accompanied by a reduction in the nearest neighbour bond lengths to make up for the lost coordination. However, the shorter bonds lead to increased Coulomb interactions between electrons on Cd and S. The system responds by a buckling of the plane which increases the Cd-S bond lengths. Alternatively the Coulomb repulsion between electrons on nearest neighbour Cd and S atoms can be decreased by subjecting the system to biaxial tensile strain. This increases the Cd-S bond lengths and just 2% strain is found to result in a stable graphitic structure, a rare find among the later row semiconductors. At the bilayer limit and without any strain we find that the structure no longer remains graphitic and the bonding is now more three dimensional and

may be regarded as a step towards the bulk structure. In the case of the ionic semiconductors, the belief was that the transition to the graphitic phase was driven by potential divergence considerations for a polar surface. The buckled monolayer structure has a small dipole moment associated with it. With thickness, the dipole moment will get enhanced and so while polar structures may be realized at the few layers limit, with thickness there is a move to overcome the polar divergence. This results in non-polar structures being favoured beyond a critical thickness which is found to be two monolayers for the more covalent semiconductor CdS.

5.2 Methodology

Monolayers/bilayers of CdS have been generated by truncating two/four monolayers of Cd-S cut out from a bulk wurtzite [15] unit cell growing in the (0001) direction. The in-plane lattice constants (ab plane) have been kept fixed at the bulk experimental values while a vacuum of 20 Å has been introduced in the c-direction between images in the periodic unit cells used in our calculations. This is needed to break the periodicity along the growth direction and thus to discard the interactions between images otherwise present in the method of our calculations. In Figure 5.1 we have shown the initial wurtzite fragment of CdS monolayer structure. One idea of our calculations is to search for possible buckled structure in the monolayer limit and unit cell of two atoms can be insufficient to show any buckling in the structure. Thus, in order to realize buckling in the structures we have used $3\times 3\times 1$ as well as $6\times 6\times 1$ supercells. As will be explained later on this chapter, we have considered two different $3\times 3\times 1$ supercell model structures to understand buckling in the monolayer. While in one structure (Configuration 1 in

Figure 5.2 (a)) anions have been placed periodically in three different planes, in another structure (Configuration 2 in Figure 5.2(b)) they have been placed in two planes only.

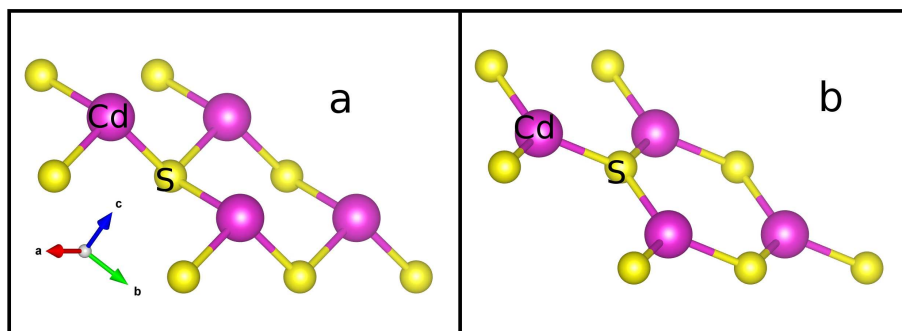


Figure 5.1: (a)Initial wurtzite fragment of the structure and the (b) planar structure after geometrical relaxations.

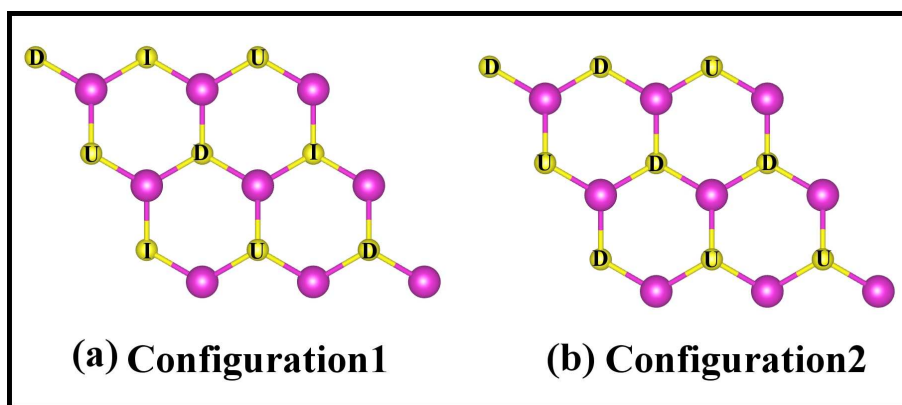


Figure 5.2: Two possible buckling configurations in the monolayer of CdS are shown. (a) In configuration 1, anions can be placed in the plane above, below and intermediate planes. (b) In configuration 2, anions can be placed in plane above and below only.

Ground state energies have been calculated within a plane-wave implementation of density functional theory using projector augmented wave (PAW)

[16, 17] potentials as implemented in Vienna ab-initio Simulation Package (VASP) [15]. We have used the local density approximation (LDA) [22] for the exchange correlation functional. Full geometrical optimization of internal coordinates have been done in absence of any symmetry till an energy convergence of 10^{-5} eV and force convergence of $5 \text{ meV}/\text{\AA}$ have been achieved. For model structures the total energy has been evaluated as a function of a reaction coordinate. All symmetry operations have been switched off during the supercell ground state energy calculations. A dense gamma centered mesh of $16 \times 16 \times 1$ K-points has been used to span the whole Brillouin zone while calculating ground state energies. Dynamical stability of all the derived structures has been investigated by calculating the phonon spectra. Finite displacement method as implemented in the Phonopy code [23] has been used to calculate the force constants and therefore the phonon dispersion. Supercells of $4 \times 4 \times 1$ unit cells of the planar structure with gamma centered mesh of $8 \times 8 \times 1$ k-points have been used to calculate force constants accurately within our density functional theory calculations. The acoustic sum rule has been used to ensure zero phonon frequencies for all three acoustic phonon modes at gamma point. Both chiral as well as achiral structures were considered in the two monolayers limit. Chiral bilayer structures of CdS and CdSe have been generated by truncating two layers of cations and anions from the bulk wurtzite structures. As already mentioned, we have kept the in plane lattice constant fixed to the bulk values but have introduced vacuum along (0001) directions. Achiral structures have been generated from the initial chiral structures and by swapping positions of one cation with anion. All electronic and structural calculations are similar to the calculations done for monolayers. To calculate the polarization, we have used the Berry phase method [24] as implemented in VASP. For further analysis the ab-initio band structure has been mapped onto a tight binding model with Cd s and S s,p

orbitals in the basis. The radial parts of these wavefunction are maximally localized Wannier functions. The VASP to Wannier90 [21, 26] interface has been used for these calculations.

5.3 Results and Discussions

At the outset we took two monolayers of CdS(one layer each of Cd and S) cut out from a wurtzite cell to examine if a graphitic phase was stabilized. Allowing the atoms to relax and lower their energy, we found a barrier-less transformation into the graphitic phase. The graphitic phase was found to be 197 meV/ formula unit (f.u.) lower in energy than the starting wurtzite derived structure. In the bulk wurtzite structure of CdS, each cation and anion are tetrahedrally coordinated with each other and the bonding is found to be sp^3 type. Part of the energy gain in a transformation from a sp^3 bonded structure to a sp^2 bonded one comes from shorter Cd-S bonds. The reduction in bond lengths compensates for lost coordination. These are found to be reduced by 6% from the wurtzite phase. In contrast one found the reduction to be 8% in the case of carbon [5]. As this was a rare occurrence of a graphitic phase in a later row semiconductor, we went on to probe if the structure was dynamically stable. For that we calculated the phonon dispersion considering the planar structure. The calculated phonon dispersion are shown in Figure 5.3.

Mode softening for one of the acoustic phonon modes is found along most of the Brillouin zone. The deepest phonon instabilities at M and K point have been found to arise from the force on S ions trying to move them out of plane(In the inset of Figure 5.3 we have shown the direction of force corresponding to M and K points). The reason that the planar structure

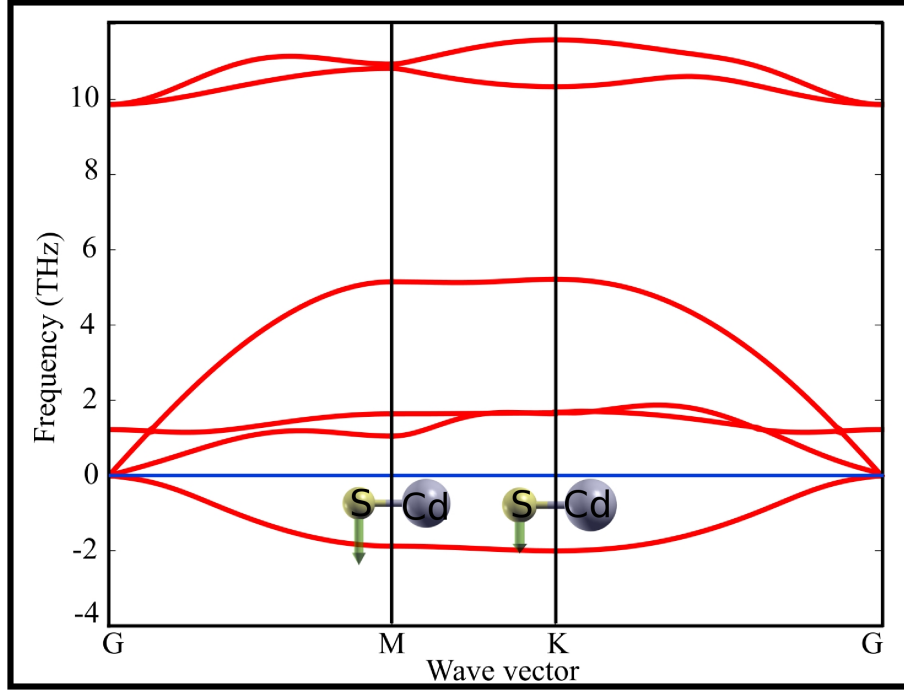


Figure 5.3: Phonon dispersion of planar monolayer of CdS. Mode softening through out the Brillouin zone signifies the dynamical instability of such structure. Resulting force acting on S ion, corresponding to M and K points are shown in the inset.

is unstable is because the system makes up for lost coordination in going from the four fold coordinated wurtzite phase to the three fold coordinated graphitic phase via shortening the Cd-S bonds. However, in contrast to the first row compounds, even at these reduced distances one finds that the Coulomb repulsion between electrons on Cd and those on S is substantial. Considering a $3 \times 3 \times 1$ supercell of CdS and allowing the atoms to move out of plane, one finds that the system gains energy by buckling. The anions move out of the plane formed by the cations in the buckled structure, with them lying in the plane above or the plane below. In the buckled structure one finds that the Cd-S bond lengths have increased to 2.43 \AA as against the

bond length of 2.39 Å found in the planar structure. This buckled structure along with the separation between upper and lower anionic planes has been shown in the Figure 5.4. Anions in the plane above and below the cation plane have been indicated with U and D respectively.

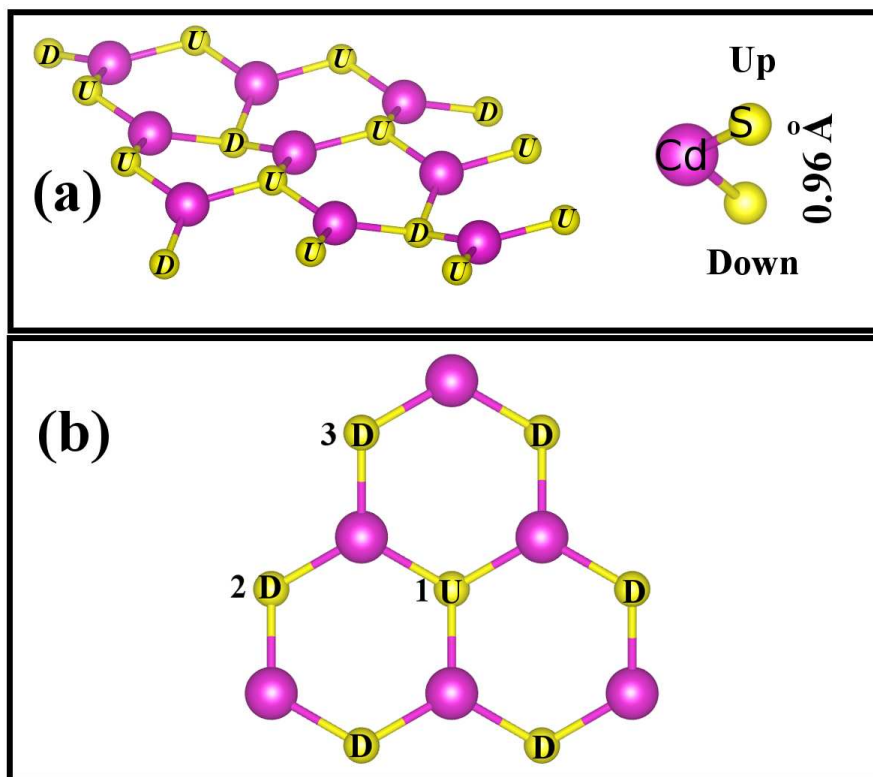


Figure 5.4: (a) Buckled monolayer structure of CdS. Anions denoted by U and D are in the planes above and below respectively of the plane formed by Cd. Separation between U and D planes are shown separately. (b) Frustration in the buckled hexagonal structure is shown.

Movement of anions can be understood from the idea of spatial extension of the wavefunction associated with different orbitals. As a result of the more extended wavefunction of the $3p$ orbitals of sulfur, the Coulomb interactions between anions are also large, although they are second neighbours. In order

to reduce this Coulomb repulsion they move as far away as possible. Thus their separation increases in the buckled structure from the distance of 4.14 Å found in the planar structure to 4.23 Å.

In addition to the reduction in the Coulomb interactions which shows up in the difference in the Hartree energy between the two structures, one also has a gain from sp^3 bonding in the buckled structure. The bond angles between Cd and S are now found to be 116 and 121 degrees, suggesting a mixture of sp^3 and sp^2 bonding. The separation between upper and lower anionic planes is found to be 0.96 Å. As the unit cell was large, we have calculated phonon dispersion at the gamma point only and phonon modes are found to be positive. These results suggest that by increasing the separation between Cd and S atoms, one can reduce the Coulomb interactions between electrons on both atoms. In order to examine if this would stabilize the structure, we calculate phonon dispersion for the planar structure subjected to 2% biaxial strain. Phonon dispersion is shown in Figure 5.5. It is not immediately evident that the structure should be stable as we are reducing the gain from bond formation by expanding the lattice. Surprisingly we find only positive phonon modes, indicating that the structure is stable. So, one has the rare realization of a sp^2 bonded phase for CdS. The phase has earlier been stabilized for first row elements and their compounds.

In order to realize a zero dipole moment for the buckled structure it is evident that we must have equal numbers of U and D sites. Additionally each anion wants to maximize its separation between nearest neighbour anions. This can be achieved if the anions in the upper plane have all of its anionic neighbours in the lower plane. In the buckled hexagonal geometry of CdS this is not possible. Referring to the Figure 5.4(b), anion U indexed by 1 wants to maximize the separation between all anionic neighbours. This can

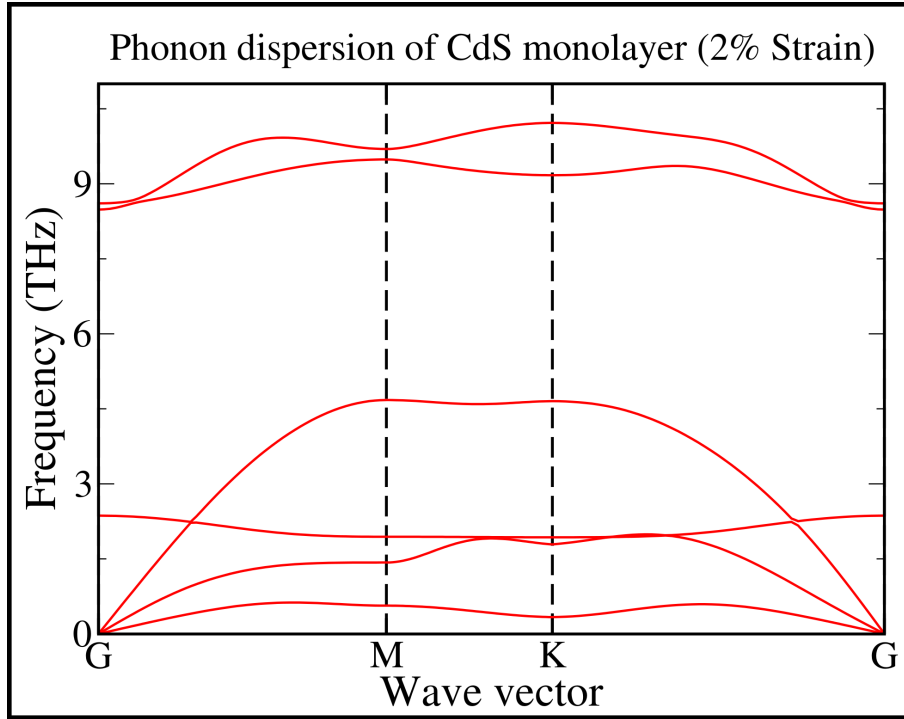


Figure 5.5: Phonon dispersion of planar monolayer of CdS under 2% biaxial strain. Structure is found to be dynamically stable from its phonon dispersion analysis.

be achieved if all of its anionic neighbours sit in the D plane. Thus we should have anions indexed by 1 and 2 in the D plane. But if anion 2 is in D plane, we should have anion 3 in the U plane. Therefore positions of anions in the buckled structure is not well defined. The problem is analogous to finding an anti-ferromagnetic ground state on a triangular lattice where analogous to the U and D sites, one has up and down spins. This is a well studied problem in magnetism and indeed a completely anti-ferromagnetic state is not realizable. In the present problem we have another option for the choice of the anion site. It could occupy a position in the same plane as the cations. We denote this by I. We then consider two configurations 1 and 2 as shown in Figure 5.2. In configuration 1 we have some anions at I site and so we

can satisfy the zero dipole moment requirement. Configuration 2 has more number of atoms in the lower plane(D) than in the upper one and hence has a net dipole moment. Placing the anions in configurations 1 and 2 at different anion separations we find that for all relevant values, configuration 2 has lower energy(Figure 5.6). This indicates that a finite dipole moment would be inevitable for structures of later row compounds. The optimized structure whose ground state energy is shown as a diamond in the same figure is primarily derived from configuration 2 again has a finite dipole moment associated with it.

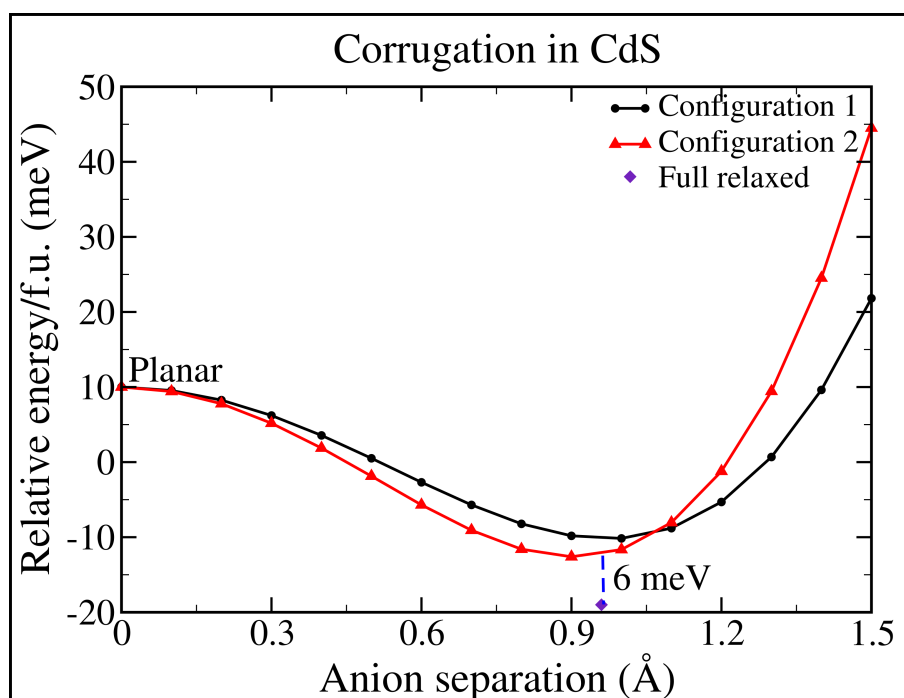


Figure 5.6: Total energy comparisons between two different configurations. Configuration 2 is found to have lower energy near relevant region. Completely relaxed structure is found to have 6 meV/f.u. lower energy than the Configuration 2.

Arranging unit cells with opposite polarization in the ab-plane so that we have a net zero electric polarization again does not lead to a solution which has lower energy. The energy per formula unit for the two buckled structures found at the monolayer limit are not found to be substantially different from each other. The calculated dipole moment per unit volume or the electric polarization are shown in Table 5.1 for monolayers of wurtzite structure of CdS and ZnO. The value for ZnO is found to be larger, consistent with the more ionic nature of the compound. While ZnO favours a graphitic phase which has a zero dipole moment associated with it, CdS is found to favour a buckled graphitic structure which has a small polarization of $3.85 \mu\text{C}/\text{cm}^2$ (Table 5.1). These results suggest that for more covalent materials, at the monolayer limit a structure with a finite dipole can be sustained while for thicker films the only way for these semiconductors to avoid a divergence of the electrostatic potential is to adopt a non-polar structure.

System	Polarization
ZnO wurtzite	$195.82 \mu\text{C}/\text{cm}^2$
CdS wurtzite	$117.52 \mu\text{C}/\text{cm}^2$
CdS buckled	$3.85 \mu\text{C}/\text{cm}^2$

Table 5.1: Polarization of two monolayers of ZnO and CdS corresponding to a fragment of the bulk wurtzite unit cell as well as the polarization for one monolayer of relaxed buckled CdS.

We then went on to consider four monolayers of wurtzite CdS. Allowing the atoms to move and find the minimum energy configuration, we found that the ensuing structure had a zero dipole moment, and was $300 \text{ meV}/\text{f.u.}$ lower in energy than the one monolayer relaxed structure. An unusual structure was realized which could be described as chiral and is shown in the Figure 5.7. Each Cd atom has three S neighbours in the ab plane which are 2.46

Å away. In the z direction, there is a S neighbour which sits above the Cd atom making a bond length of 2.76 Å. Hence this structure represents a step towards the bulk wurtzite structure for CdS with the coordination equal to four.

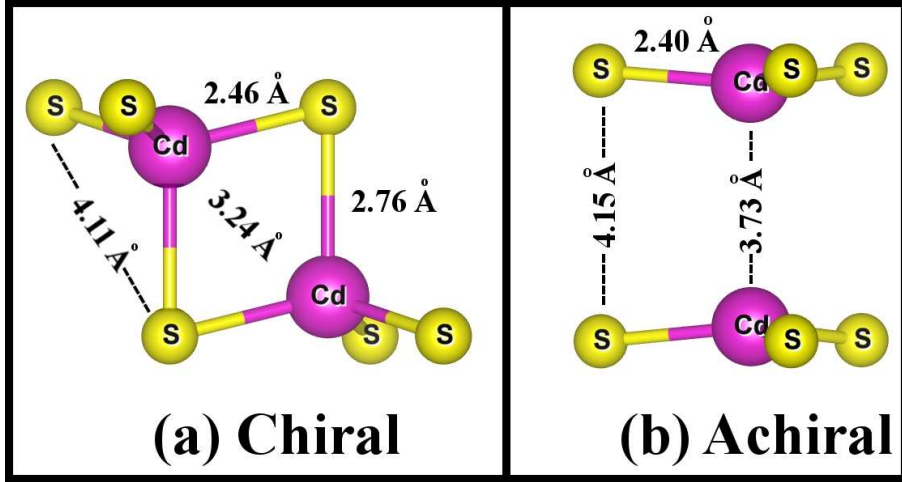


Figure 5.7: (a) Chiral bilayer and (b) Achiral bilayer of CdS.

Examining the energetic which make this configuration favourable, we see that it is both the increased coordination as well as the gain in Coulomb interactions which stabilize this structure. In order to minimize Coulomb interactions between neighbouring atoms, each Cd prefers to have S atom on top in the c direction. This is especially evident when we examine the achiral configuration which is 361 meV higher in energy in which the Cd/S atoms are on top of each other. As the Cd atoms have localized d electrons as a part of the valence band, they prefer to have large separation of 3.73 Å in the achiral structure that they form. Considering In, Ga compounds [27, 28] where the d electrons are deeper, one finds that it is the achiral structure which is favoured. In addition to the weaker Coulomb interactions on the In/Ga atoms, there is also substantial hopping interaction between the atoms. The next question we asked was whether the bilayer chiral structure

which was found to have the lowest energy in our structural optimization was dynamically stable. In order to examine this we have calculated the phonon dispersion along various symmetry directions as shown in Figure 5.8. Other than small regions near Γ points we did not find imaginary phonon modes. These regions of instability are extremely sensitive to the size of the supercell and vanishes as the size of the supercell is increased (shown in inset of Figure 5.8).

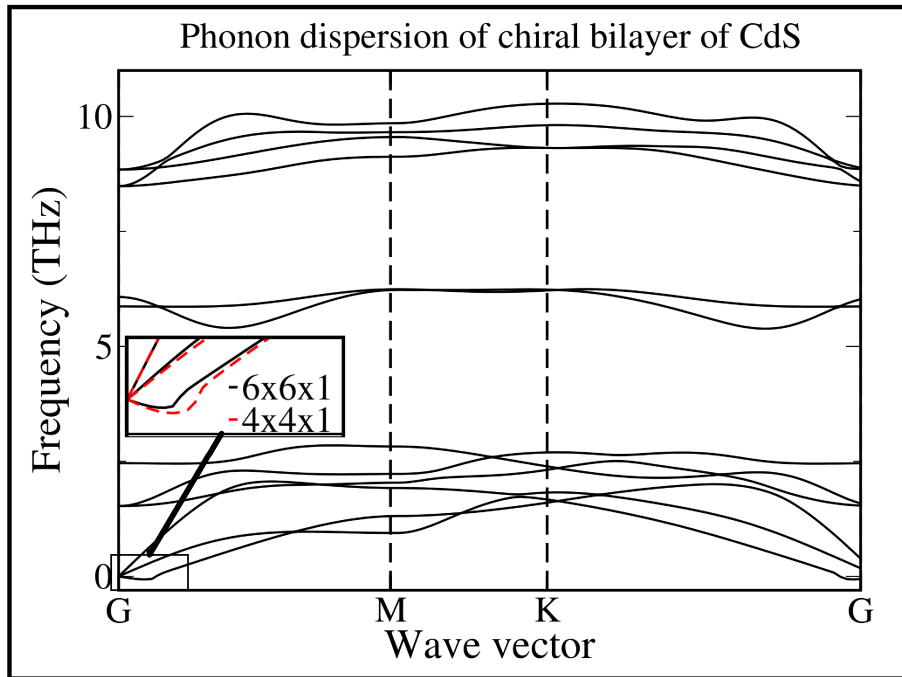


Figure 5.8: Phonon dispersion of chiral bilayer of CdS. Removable phonon instability near gamma point is shown in the inset.

The band dispersion for the bilayer chiral structure has been calculated and is shown in Figure 5.9. The system is found to have a direct band gap of 1.81 eV, with both the VBM as well as the CBM found to occur at the Γ point. There is lifting of degeneracy of the S p orbitals contributing to the valence band maximum. One finds that while p_x and p_y orbitals contribute

to the valence band maximum, the energy level with dominantly p_z character is 396 meV deeper. Degeneracy lifting in bulk wurtzite CdS structure due to the crystal field splitting is found to be of the order of 50 meV and it is thus fairly enhanced in the bilayer structure due to strong localization of the wavefunction as a result of confinement in the z -direction.

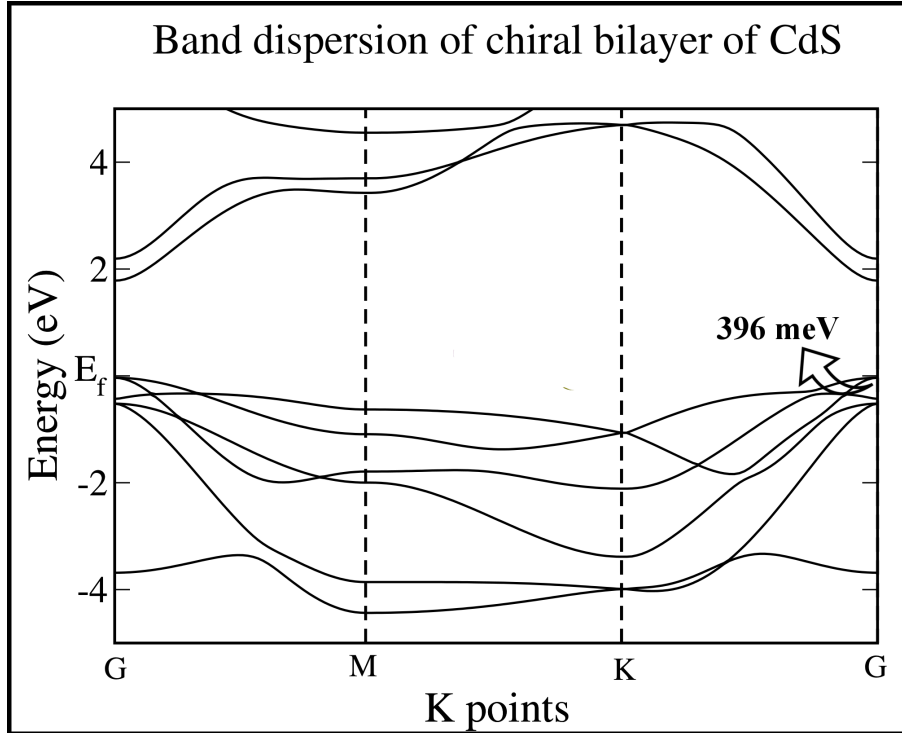


Figure 5.9: Band dispersion of chiral bilayer of CdS. Crystal field splitting at gamma point has fairly reduced from the monolayer limit but still higher than the bulk value.

In order to understand the large stability of the bilayer with respect to the planar structure, we have fitted the ab-initio band to a tight binding model. Maximally localized Wannier functions with the appropriate spherical harmonics are chosen as the basis functions. The bond lengths are similar and so the extracted hopping interaction strengths are expected to be similar.

The onsite energies referenced to the Cd-s orbitals are shown in Figure 5.10 while the S- p_x , p_y orbitals have similar energies for both systems, a huge stabilization of 3.68 eV is found for the S p_z orbital in the bilayer.

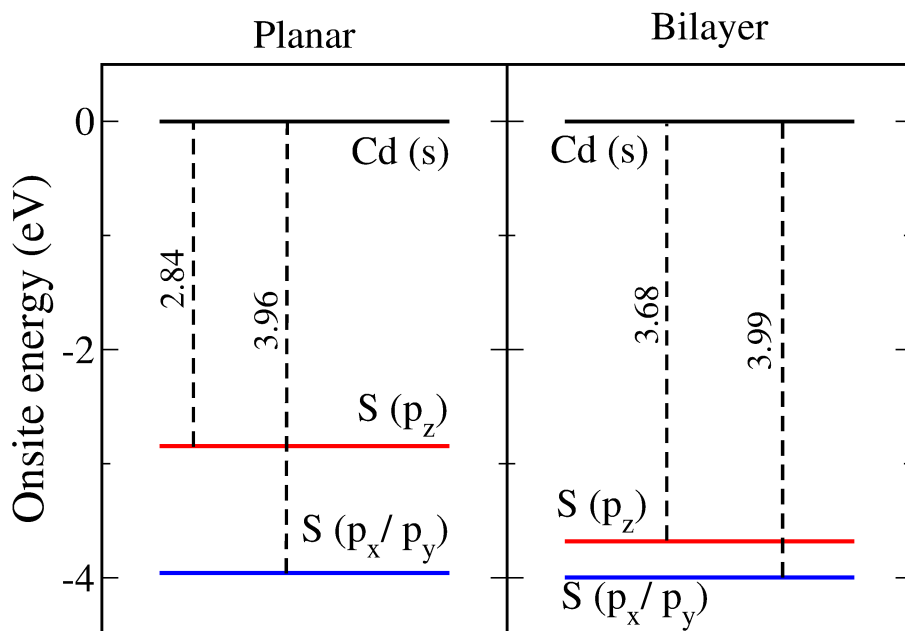


Figure 5.10: Onsite energies of S p states referenced to the Cd s states determined from a fitting of the ab-initio band structure to a tight binding model.

The energy of the S p_z orbital for the monolayer is found to be only 2.84 eV deep. The origin of this stabilization is traced to the strong hopping matrix elements of the S p_z orbital with Cd p_z orbital. This channel of delocalization stabilizes the bilayer over the monolayer structures. There is a priori no reason why the Cd-s levels should be aligned in both the systems. We use the average electrostatic potential in the vacuum region and use that as a reference in both systems. Average electrostatic potential reaches a constant value in the vacuum region and that has been shown in the Figure

5.11. The bilayer energies are found to move deeper and the conclusion derived assuming the Cd-s orbitals are aligned remain.

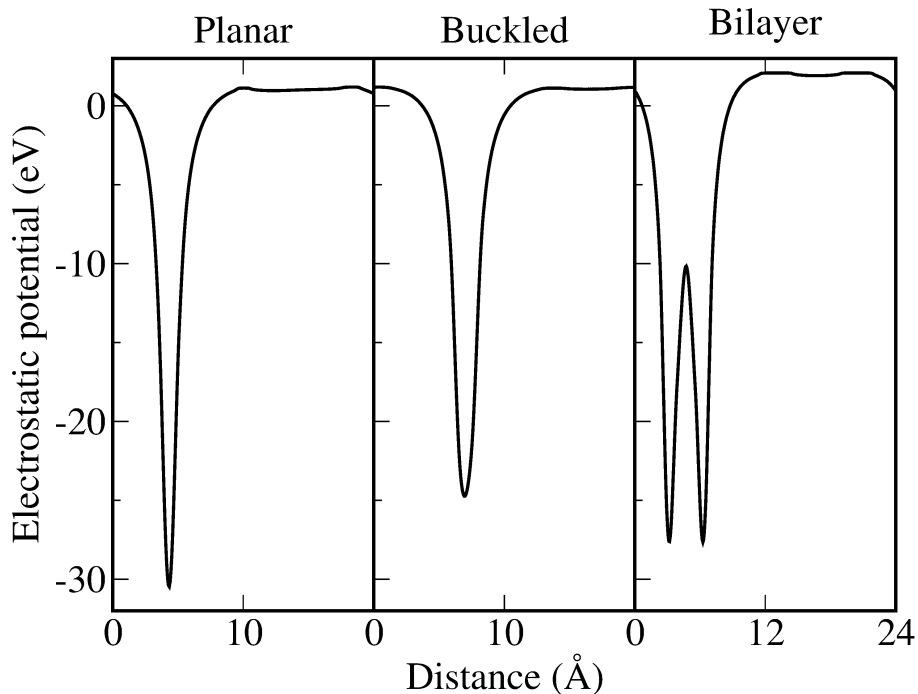


Figure 5.11: Local electrostatic potential plot for different structures.

5.4 Conclusion

We have explored the possibility of forming graphitic phases in ultra thin films of CdS. While the films formed at the experimental lattice constant are found to exhibit buckling, a small biaxial tensile strain is found to stabilize a graphitic phase. While divergence of the electrostatic potential are found to drive the structures favoured for ionic compounds, for more covalent semiconductors a finite though small dipole moment can be sustained at the monolayer limit. This builds up the electrostatic potential with thickness and at the bilayer limit a non-polar structure is strongly favoured.

Bibliography

- [1] A. Ohtomo, D. A. Muller, J. L. Grazul, and H. Y. Hwang, *Nature* **419**, 378 (2002).
- [2] H. Y. Hwang, Y. Iwasa, M. Kawasaki, B. Keimer, N. Nagaosa, and Y. Tokura, *Nature Mat.* **11**, 103 (2012).
- [3] N. Nakagawa, H. Y. Hwang, and D. A. Muller, *Nature Mat.* **5**, 204 (2006).
- [4] W. A. Harrison, E. A. Kraut, J. R. Waldrop, and R. W. Grant, *Phys. Rev. B* **18**, 4402 (1978).
- [5] K. S. Novoselov, A. K. Geim, S. V. Morozov, D. Jiang, Y. Zhang, S. V. Dubonos, I. V. Grigorieva, and A. A. Firsov, *Science* **306**, 666 (2004).
- [6] B. Radisavljevic, A. Radenovic, J. Brivio, V. Giacometti, and A. Kis, *Nat. Nanotechnol.* **6**, 147 (2011).
- [7] Y. Zhang, J. Ye, Y. Matsushashi, and Y. Iwasa, *Nano Lett.* **12**, 1136 (2012).
- [8] Z. Yin, Hai Li, Hong Li, L. Jiang, Y. Shi, Y. Sun, G. Lu, Q. Zhang, X. Chen, and H. Zhang, *ACS Nano* **6**, 74 (2012).

- [9] H. Fang, S. Chuang, T. C. Chang, K. Takei, T. Takahashi, and A. Javey, *Nano Lett.* **12**, 3788 (2012).
- [10] F. Claeysens, C. L. Freeman, N. Allan, Y. Sun, M. N. R. Ashfolda, and J. H. Harding, *Journal of Mater. Chem.* **15**, 139 (2005).
- [11] C. Tusche, H. L. Meyerheim, and J. Kirschner, *Phys. Rev. Lett.* **99**, 026102 (2007).
- [12] B. Rakshit, and P. Mahadevan, *Phys. Rev. Lett.* **107**, 085508 (2011).
- [13] Colin L. Freeman, Frederik Claeysens, Neil L. Allan and John H. Harding, *Phys. Rev. Lett.* **96**, 066102 (2006).
- [14] A. Nag, K. Raidongia, K. P. S. S. Hembram, R. Datta, U. V. Waghmare, and C. N. R. Rao, *ACS Nano* **4**, 1539 (2010).
- [15] Y. Liu, Y. Xu, J.P. Li, B. Zhang, D. Wu and Y.H. Sun, *Mater. Res. Bull.* **41**, 99 (2006).
- [16] H. Takeda, and K. Shiraishi, *Phys. Rev. B* **50**, 14916 (1994).
- [17] B. Aufray, A. Kara, S. Vizzini, H. Oughaddou, C. Leandri, B. Ealet, G. L. Lay, *App. Phys. Lett.* **96**, 183102 (2010).
- [18] G. H. Wannier, *Phys. Rev.* **79**, 357 (1950).
- [19] G. Kresse and D. Joubert, *Phys. Rev. B* **59**, 1758 (1999).
- [20] P. E Blöchl, *Phys. Rev.* **50**, 17953 (1994).
- [21] G. Kresse and J. Furthmüller, *Phys. Rev. B* **54**, 11169 (1996).
- [22] J. P. Perdew, and A. Zunger, *Phys. Rev. B* **23**, 5048 (1981).

- [23] Atsushi Togo, Fumiyasu Oba, and Isao Tanaka, *Phys. Rev. B* **78**, 134106 (2008).
- [24] R. W. Nunes and Xavier Gonze, *Phys. Rev. B* **63**, 155107 (2001).
- [25] A. A. Mostofi, J. R. Yates, Y.-S. Lee, I. Souza, D. Vanderbilt and N. Marzari, *Comput. Phys. Commun.* **178**, 685 (2008).
- [26] C. Franchini, R. Kovacik, M. Marsman, S. Sathyanarayana Murthy, J. He, C. Ederer and G. Kresse, *Journal of Physics: Cond. Matt.* **24**, 235602 (2012).
- [27] V. Zolyomi, N. D. Drummond, and V. I. Falko, *Phys. Rev. B* **89**, 205416 (2014).
- [28] D. V. Rybkovskiy, N. R. Arutyunyan, A. S. Orekhov, I. A. Gromchenko, I. V. Vorobiev, A. V. Osadchy, E. Yu. Salaev, T. K. Baykara, K. R. Allakhverdiev, and E. D. Obraztsova¹, *Phys. Rev. B* **84**, 085314 (2011).

Chapter 6

Orbital Ordering Driven Magnetism in Fe Intercalated TaS₂

6.1 Introduction

The isolation of the first two-dimensional material, graphene [1], has brought the focus on the entire family of layered materials [2–6]. These systems are obvious candidates to probe two-dimensional physics as the weak van der Waal’s coupling between layers allows the facile removal of one or more layers. These materials have been extensively studied in recent times and their application in various devices explored. In this chapter we consider an interesting member of this family of materials, Fe intercalated into TaS₂ layers [7–10]. Depending on the concentration of Fe intercalation, one finds that the system is either ferromagnetic or anti-ferromagnetic [11, 12]. Additionally one finds a very large magneto-crystalline anisotropy associated with Fe_{0.25}TaS₂,

which makes it useful for switching applications. In this work, we explore the evolution of the magnetic properties with intercalation. Prior to the introduction of the Fe atoms, one has only TaS₂ layers which are metallic. This has led to an RKKY [13] model being proposed to explain the magnetism. Originally the model has been used to explain the oscillatory magnetic coupling that one has in magnetic multilayers with nonmagnetic spacers [14], and the present model seems to be in the same direction of thought, though here instead of magnetic multilayers, we have an intercalated layer of Fe atoms. Such a model assumes a spin only interaction between the magnetic atoms and the conduction electrons. While this makes us to anticipate ferromagnetic interactions at some coverage and anti-ferromagnetic interactions at some coverage, analyzing the magnetic phase diagram, it seems that one can divide it into two parts. Up to an Fe concentration of 40%, it is found to be ferromagnetic while it is anti-ferromagnetic above that [11, 12]. This seems to suggest the presence of competing exchange pathways rather than an oscillatory coupling. In order to examine this aspect, we have considered several concentrations and examined the changes in the electronic structure and its effect on the favoured magnetic structure.

Considering the 25% Fe intercalated case, one finds that the Fe d_{z^2} levels are occupied in the minority spin channel while these levels are unoccupied on the Ta sites. For Fe_{0.5}TaS₂ on the other hand one has the minority spin $d_{x^2-y^2}$ orbitals on Fe occupied while d_{z^2} orbitals are empty. At low concentrations the typical Fe-Fe separations are 6 Å and so any coupling between Fe sites is small. However, the topology of the structure is such that it allows hopping between Fe and Ta sites in the z -direction, thereby coupling the d_{z^2} orbitals on both sites. This channel leads to a ferromagnetic alignment of the spins on Fe in the z direction. As Fe donates two electrons to the Ta levels, one finds that with increasing Fe concentration the Ta d_{z^2}

levels get filled up. These levels then move below the Fe d_{z^2} levels with which they interact. As a result the Fe d_{z^2} levels get emptied, and the electron in the minority spin channel on Fe occupies the $d_{x^2-y^2}$ orbitals. The channel of hopping for ferromagnetically coupled Fe atoms is therefore removed. Hence with increasing Fe intercalation we have a transition from ferromagnetism to antiferromagnetism. This picture of the effect of the electronic structure on the magnetism has been verified by artificially changing the character of the highest occupied states on Fe at a particular concentration. This again leads to a crossover from ferromagnetism to antiferromagnetism.

6.2 Methodology

The electronic structure of Fe_xTaS_2 for $x=0.25, 0.33$ and 0.50 was calculated using the Vienna ab-initio simulation package (VASP) [15] which involves a plane-wave projector augmented wave (PAW) [16, 17] implementation of density functional theory. A gamma centered k-points grid of $16 \times 16 \times 8$ has been used with a cutoff energy of 500 eV for the kinetic energy of the plane waves included in the basis. The generalized gradient approximation to the exchange correlation functional has been used [18, 19]. Additional orbital-dependent potentials have been used on Fe within the GGA+U framework using the Dudarev implementation [17]. Unless otherwise stated, the value of U that we have used is 4 eV. Spin orbit(SO) interaction strength is expected to be significant for 5d transition metal compounds thus we incorporated SO corrections for several calculations also. Fe_xTaS_2 form ordered super-lattice for $x=0.25, 0.33$ with lattice parameters $a'=2a_0$ and $a'=\sqrt{3}a_0$ respectively where a_0 is the basic lattice parameter of the TaS_2 array. In the basic 2H structure of TaS_2 , Ta atoms are in trigonal prismatic coordination with S

atoms and Fe on doping occupy some of the high symmetry non-lattice intercalant positions. Lattice parameters were kept fixed at the experimental values [8] while the internal positions were relaxed till the energy convergence of 10^{-5} eV and the force convergence of $5 \text{ meV}/\text{\AA}$ were met. Different magnetic configurations labeled AFM1, AFM2, AFM3 and FM as shown in Figure 6.1 were considered to search for the favoured magnetic ground state. In AFM1 we have Fe spins coupled antiferromagnetically in the ab-plane as well as in the c direction. AFM2 has the Fe spins coupled antiferromagnetically in the ab-plane but coupled ferromagnetically in the c direction. AFM3 has the spins coupled ferromagnetically in the ab-plane but coupled antiferromagnetically in the c direction and FM is ferromagnetic configuration. Analysis of the ab-initio band structure was carried out by mapping onto a tight-binding model with Fe d, S p and Ta d_z^2 , $d_{x^2-y^2}$ and d_{xy} orbitals in the basis and maximally localized Wannier functions [21] as the radial parts using the VASP to Wannier interface [22].

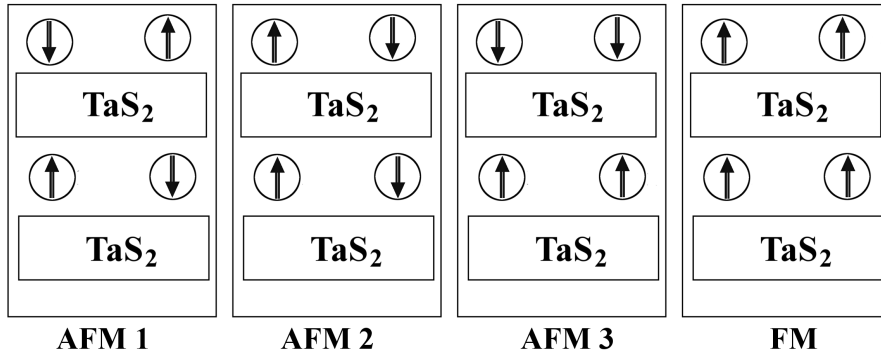


Figure 6.1: Different magnetic configurations of Fe intercalated TaS_2 structures.

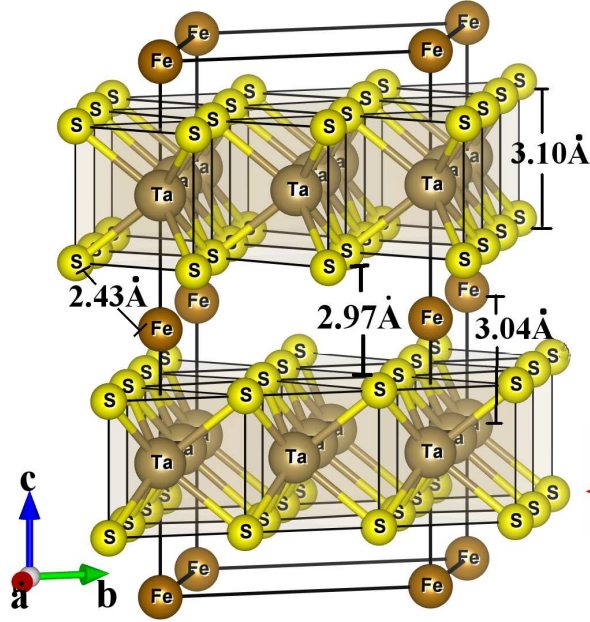


Figure 6.2: Crystal structure of $\text{Fe}_{0.25}\text{TaS}_2$. Separation between different atoms have been shown along with 2h block of TaS_2 network.

6.3 Results and Discussions

The structure of $\text{Fe}_{0.25}\text{TaS}_2$ is given in Figure 6.2. In the parent 2H hexagonal structure, two different TaS_2 layers are stacked in ABAB fashion. Ta is in trigonal prismatic coordination with S. Fe upon intercalation occupies certain high symmetry non lattice sites. As is evident from the figure, one has two layers of TaS_2 separated by a distance of 2.97 Å. This is believed to result in a weak van der Waal's interaction between two TaS_2 layers. Fe-Fe separation in the ab plane is 6.61 Å and it is 6.04 Å along the c direction. Separation between Fe-Ta and Fe-S are 3.04 Å and 2.43 Å respectively. Though we have not shown in the figure, Fe occupies vacant in-plane non lattice sites between two TaS_2 layers upon additional doping. As an example, in-plane

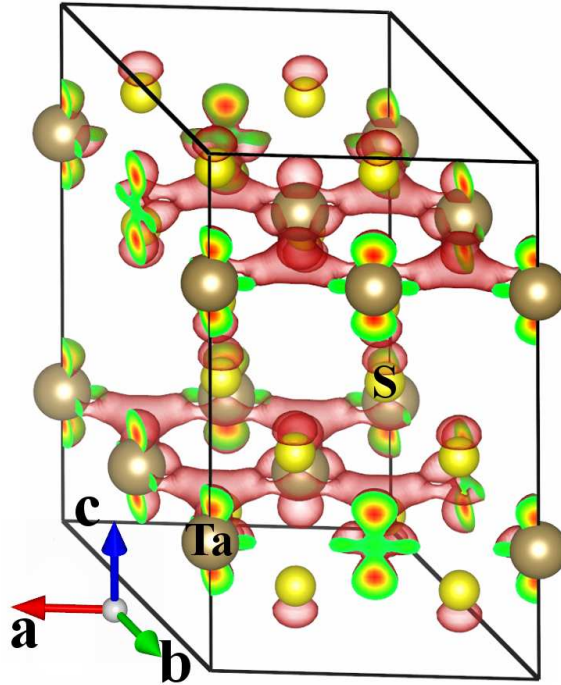


Figure 6.3: Charge density close to the fermi level is confined within TaS_2 layer. Significant contribution from Ta d and S p states is evident.

Fe-Fe separation reduces to 3.31 \AA while out of plane separation remains the same in case of $\text{Fe}_{0.50}\text{TaS}_2$.

The TaS_2 layers are nonmagnetic as well as metallic and examining the charge density at the fermi level, one finds that the conduction is confined primarily to the two-dimensional TaS_2 layers. The occupation of non-lattice sites by the intercalated Fe atoms, coupled with the fact that the atoms occupy the region between two TaS_2 layers has led to a picture where the charge and orbital degrees of freedom of the electrons on the Fe site may be ignored and only the spin degree of freedom needs to be considered. The spins on the Fe

atom interact with the conduction electrons associated with the metallic TaS₂ layer and this RKKY-type interaction is believed to mediate magnetism.

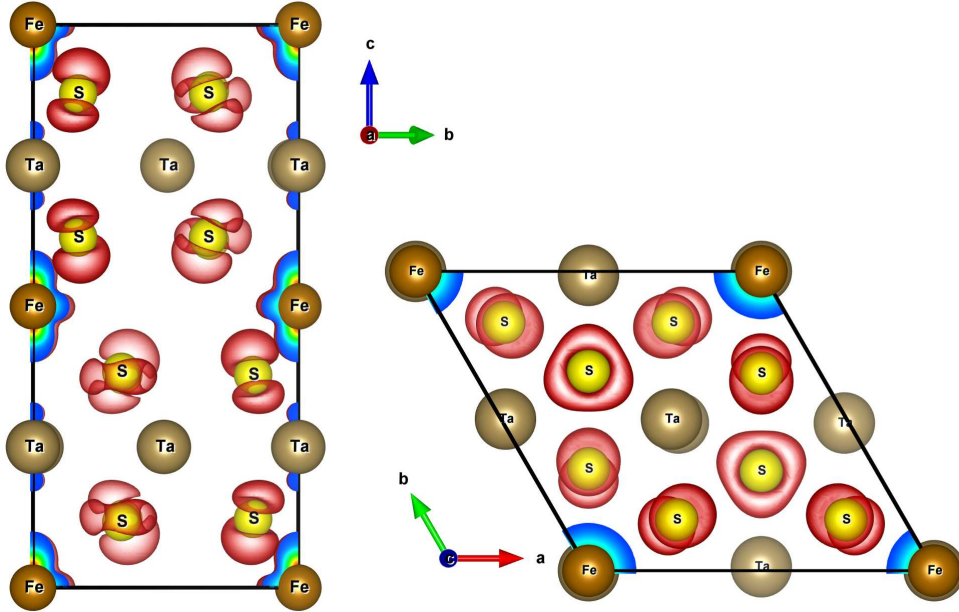


Figure 6.4: Charge density for the states close to 1.5 eV below the Fermi energy in the minority spin channel.

Examining the TaS₂ layer, we find that the charge density close to the Fermi energy as presented in the Figure 6.3, is confined within the TaS₂ layer. Significant contribution from d_{z^2} orbitals on Ta and p_z orbitals on S have been found. The separation between Fe and S atoms is 2.43 Å and that between Fe and Ta atoms is 3.04 Å, so it is not unusual to expect an interaction between the intercalated Fe atoms and the TaS₂ layer. Indeed we examine the charge density corresponding to states mainly coming from Fe d_{z^2} levels, close to 1.5 eV below the Fermi energy for the minority spin states. We

find significant interaction between the Fe and TaS₂ layers (Figure 6.4) and a spin-only description of the Fe atoms is not valid here. This is also evident from the orbital projected density of states shown in Figure 6.5. The Fe *d* states are shown in the left panel while the Ta *d* states are shown in the right panel. In the majority spin channel we find that the Fe *d* states are around 4 to 6 eV below the fermi energy and are completely occupied. In the minority spin channel, one finds that only the Fe *d*_{z²} states are occupied while all other states are empty. On the other hand, Ta *d*_{xy}, *d*_{x²-y²} and *d*_{z²} states contribute at the fermi energy while the *d*_{xz} and *d*_{yz} states are unoccupied.

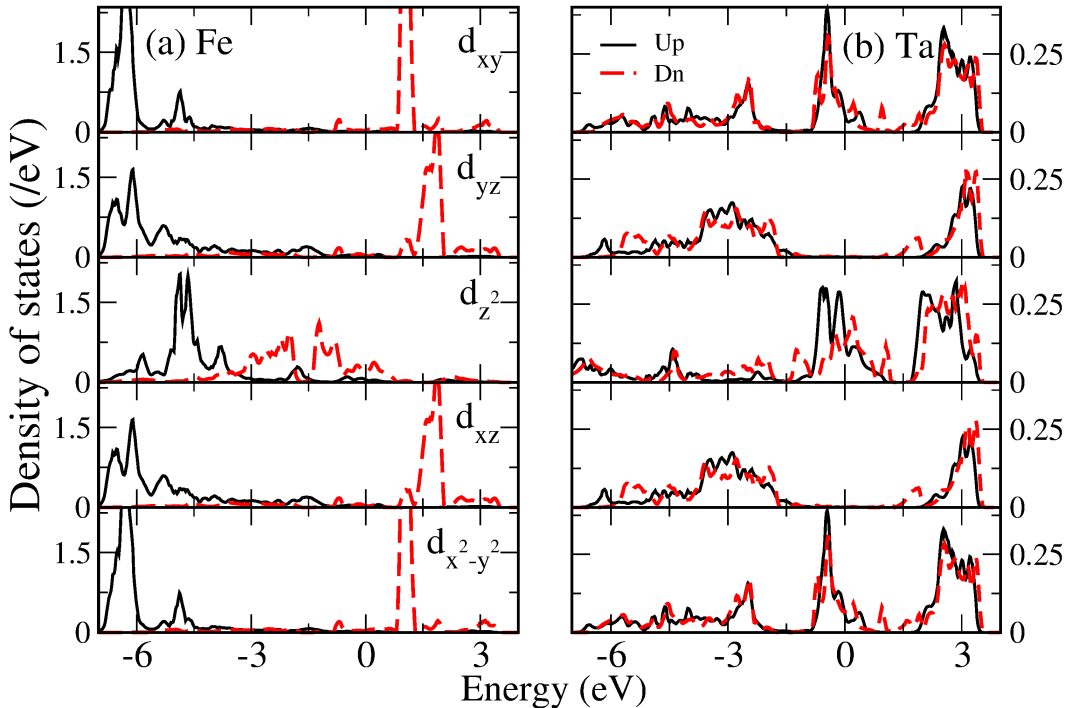


Figure 6.5: (a)Fe and (b)Ta *d* orbital projected density of states for ferromagnetic Fe_{0.25}TaS₂ calculated for U=4 eV.

S *p* orbital projected density of states are shown separately in Figure 6.6. Both the majority and the minority spin channels corresponding to S *p* states are found to be occupied leading to a p⁶ configuration. The Ta states hy-

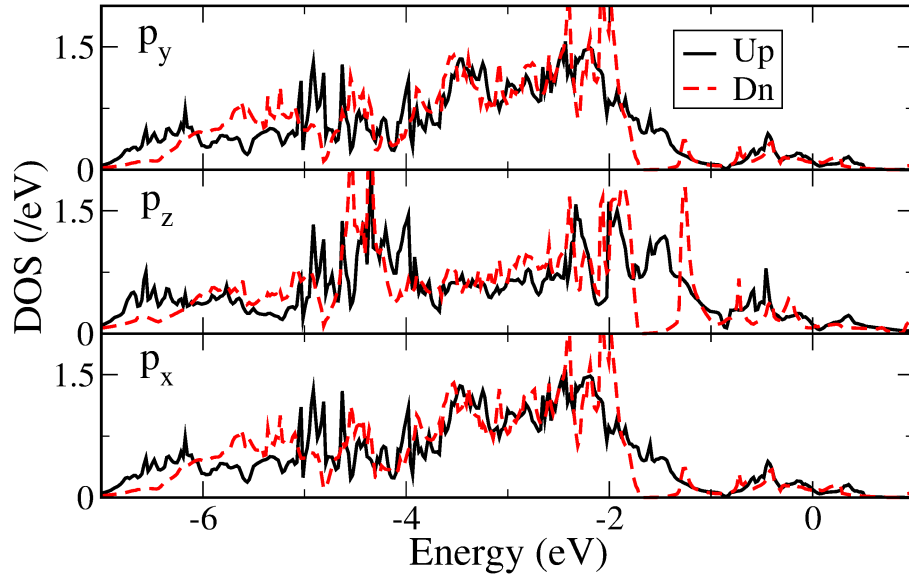


Figure 6.6: S p orbital projected density of states for ferromagnetic $\text{Fe}_{0.25}\text{TaS}_2$ calculated for $U=4$ eV.

bridize with the S p states and in the energy window from 2 eV below the fermi energy to around 7 eV below and we have the states with predominantly S p character with Ta admixture. The Ta d_{xy} , $d_{x^2-y^2}$ and the d_{z^2} interact in the xy plane, resulting in the two distinct sets of features we see around 0 eV and 3 eV in the density of states. Additionally we also have significant interaction between the minority Ta d_{z^2} states and the Fe d_{z^2} states near around 1.5 eV below the fermi level. This results in a significant polarization of the Ta d_{z^2} states. Induced magnetic moment on Ta closest to Fe are found to be $0.1 \mu_B$ per Ta and they are ferromagnetically coupled with Fe. Consistent with this observation, we find that the dispersion width of all the minority Fe d orbitals is just 0.5 eV except the Fe d_{z^2} orbitals which have a larger dispersion width associated with them. A point to note that there are two non-lattice intercalant symmetric positions available for the Fe to occupy at 25% doping concentration. Figure 6.7 shows two different

doping positions from the top. In Structure 1, Fe is doped on top of one of the Ta channels along c direction and thus forms trigonal prismatic network with nearest S atoms. Whereas for Structure 2, Fe is doped at the center of one of the hexagonal network formed by Ta and S and forms tetrahedron network with nearest S atoms. Ground state energies for these two configurations have been calculated and Structure 1 has been found to be favoured over the other one. Broken Fe-Ta network along the c direction in Structure 2 should weaken the coupling between Fe and Ta d_z^2 and magnetism should not sustain in such structure and indeed when we looked at the magnetic configuration of the resulting structure, we found it to be non-magnetic. As Fe is at an intercalant position, the immediate question that follows is what is the valence state that is favoured. Examining the Fe d density of states one finds that Fe has a d^6 configuration. This suggests a $2+$ valency, consistent with the experimental observations, associated with the Fe site. The electrons donated by the Fe atoms go on to occupy the Ta states and the electron count of Ta d states increase with the doping.

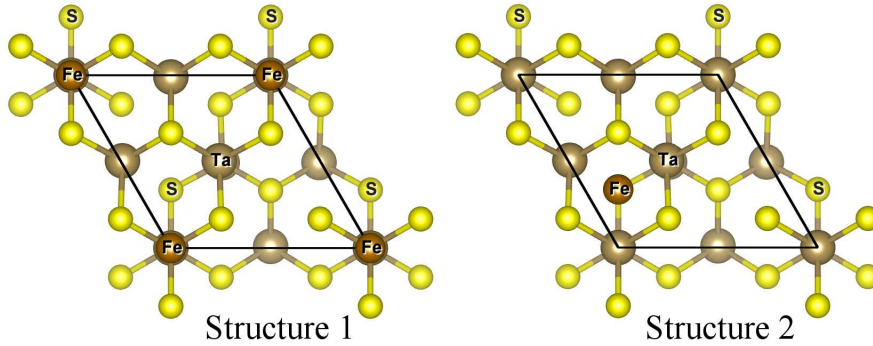


Figure 6.7: Two different doping sites for $\text{Fe}_{0.25}\text{TaS}_2$.

After examining the electronic structure at 25% Fe intercalation, we went on to explore the role of increased Fe intercalation by considering the case of 50%

intercalation. $\text{Fe}_{0.5}\text{TaS}_2$ is found to be anti-ferromagnetic. To understand the anti-ferromagnetic behaviour at this doping concentration we have plotted the orbital projected density of states. The Fe d orbital projected partial density of states are shown in Figure 6.8. Here again we find the Fe d states are completely filled in the majority spin channel. In the minority spin channel, however, in contrast to earlier, we find that the sixth electron occupies the $d_{x^2-y^2}$ orbitals. The minority spin d_{z^2} orbitals are empty at this concentration. This reordering of orbitals occurs because the Ta d states get filled up with increased Fe concentration. As a result they move below the Fe d_{z^2} states with which they interact. The hopping interaction between Fe and Ta d_{z^2} states now pushes the Fe d_{z^2} states deeper into the conduction band. Consequently, the sixth electron on Fe occupies the $d_{x^2-y^2}$ orbitals. This mechanism is shown in the Figure 6.9 with the help of two state level diagram. At low Fe concentration, interaction between Fe d_z^2 with Ta d_z^2 leads to a bonding state mainly contributed by Fe states. Whereas the same interaction at higher Fe concentration leads to anti-bonding state contributed by Fe d . Again with increased Fe intercalation, as they occupy in-plane positions, we now have the shortest Fe-Fe separation to be 3.31 Å. This leads to strong interaction between Fe atoms mediated by the S atoms resulting in wider Fe bands than seen in Figure 6.5 for 25% Fe intercalation. In-plane interaction in between two minority Fe d_{xy} orbitals via occupied S p states leads to an anti-ferromagnetic ground state.

Having understood the evolution of the electronic structure with Fe intercalation concentration, we went on to examine the magnetic stability at different concentrations. Different magnetic configurations are shown in Figure 6.1. As tabulated in Table 6.1 for the case of 25% Fe intercalation, we find the ferromagnetic configuration to have the lowest energy while AFM1, AFM2 and AFM3 are found to be 29, 213 and 30 meV higher respectively. This is

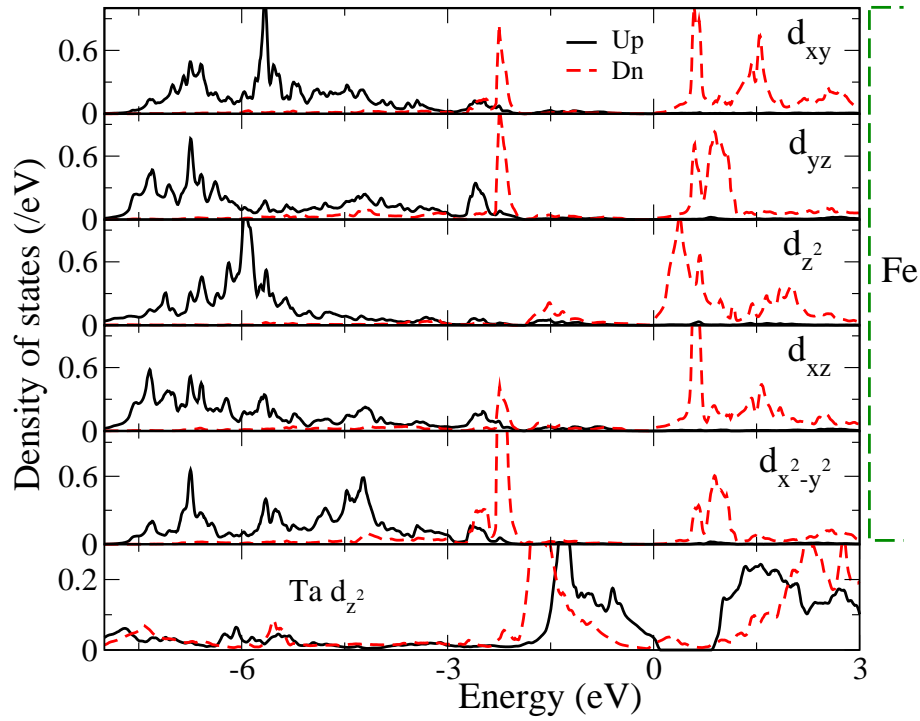


Figure 6.8: Fe d orbital projected partial density of states for AFM1 structure of $\text{Fe}_{0.50}\text{TaS}_2$ calculated for $U=4$ eV on Fe. The Ta d_z^2 projected contribution is shown in the bottom most panel.

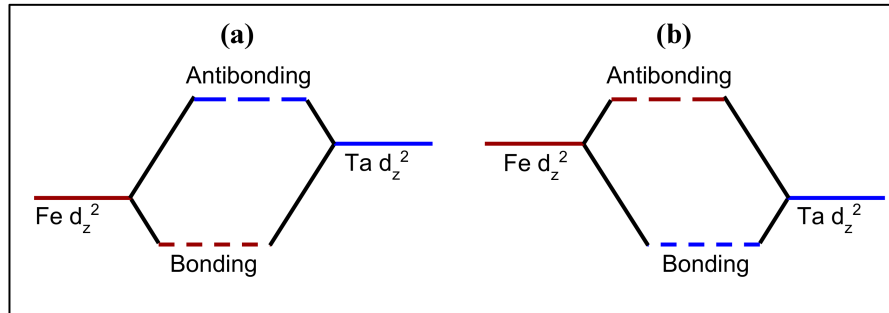


Figure 6.9: Bonding and antibonding levels originating from interaction between $\text{Fe } d_z^2$ and $\text{Ta } d_z^2$ at (a) low Fe doping and at (b) high Fe doping concentration.

consistent with the experimental observation of a ferromagnetic ground state in the system. This is easy to understand as the typical Fe-Fe separations in the ab-plane are 6.61 Å which results in a weak coupling between the Fe atoms. On the other hand, the channel of hopping through the Ta sites in the c-direction leads to a strong coupling of the Fe spins in the c-direction. Examining various magnetic configurations at 50% Fe intercalation, we find that AFM1 and AFM2 have the lowest energy, consistent with experiment. Here as the Fe-Fe separations in the ab-plane is 3.31 Å, and all the d orbitals in the majority spin channel are occupied, we have a strong antiferromagnetic coupling between the spins in the ab-plane. The removal of the channel of hopping in the c-direction for Fe sites through Ta results in a weak coupling in the c-direction.

While the calculations were able to obtain ferromagnetism at $x=25\%$ and antiferromagnetism at $x=50\%$, the question that followed was what is the role of the electronic structure in bringing about the changes in the favored magnetic ground state. At low Fe concentrations, we find that there is a pathway for an electron in the minority spin d_{z^2} orbital on Fe to hop to on Ta and couple to a ferromagnetically aligned Fe site in the c-direction. As the Ta d_{z^2} states are filled up, this channel of hopping which favored a ferromagnetic coupling between Fe spins in the c-direction is removed. Further, with increasing Fe concentration, we have the separation between in-plane Fe atoms decreasing. This also allows them to interact with each other in the ab-plane. As this channel of hopping is from the occupied majority spin states on Fe, the spin on nearest neighbor Fe sites have to be antiferromagnetically arranged for the superexchange to be possible. Hence antiferromagnetism wins over at higher Fe intercalation concentrations.

U(eV)	AFM1	AFM2	AFM3	FM
25% doping				
2	-45	5	-46	0
4	29	213	30	0
50% doping				
4	-63	-62	-34	0

Table 6.1: Relative energy of different magnetic configurations in meV as a function of Coulomb interaction strength for $\text{Fe}_{0.25}\text{TaS}_2$ as well as $\text{Fe}_{0.50}\text{TaS}_2$.

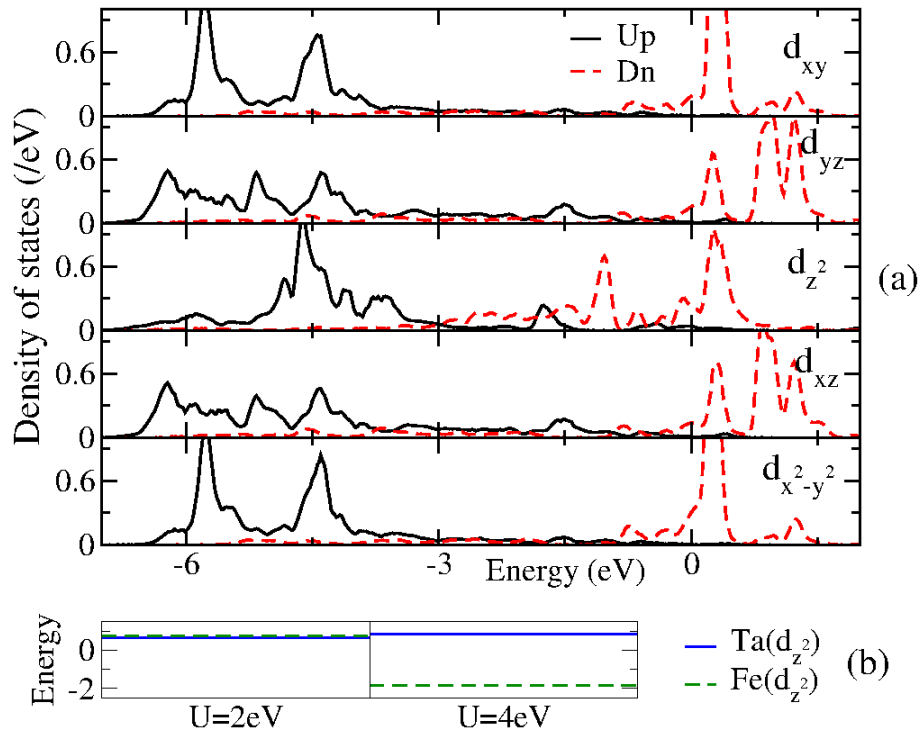


Figure 6.10: (a) Fe d orbital projected partial density of states for $\text{Fe}_{0.25}\text{TaS}_2$ calculated for $U=2$ eV. (b) Onsite energies for Fe d_{z^2} and Ta d_{z^2} levels for $U=2$ eV and 4 eV.

Applying a U on the Fe d states allows us to vary the position of the Fe d states vis-a-vis the Ta states artificially. We did exactly that considering the 25% Fe intercalated case. The Fe d orbital projected density of states for $U=2$ eV are shown in Figure 6.10(a). Again here, all the majority spin Fe d states are completely occupied. In the minority spin channel we find that the Fe d_{z^2} as well as Fe $d_{x^2-y^2}$ states are partially occupied. Analyzing the ab-initio band dispersion along various symmetry directions in terms of a tight binding model with the radial parts being given by maximally localized Wannier functions, we find that the Ta d_{z^2} are slightly below the Fe d_{z^2} levels at $U=2$ eV. However at $U=4$ eV we have the Fe d_{z^2} levels below the Ta d_{z^2} levels. This ordering has also been shown in the Figure 6.10(b). As a result of this ordering of Fe and Ta levels we have the Fe d_{z^2} levels almost empty for $U=2$ eV. By the arguments for hopping pathways presented earlier, this should result in a decreased gain for ferromagnetically aligned Fe spins. Indeed this is what we find. Calculating the magnetic stability at $U=2$ eV as shown in Table 6.1 we find that AFM1 is lower in energy than the ferromagnetic configurations by 45 meV.

6.4 Conclusion

The nature of the magnetic ground state for Fe_xTaS_2 has been examined within ab-initio electronic structure calculations. A spin only model of the interaction between Fe and the conduction electrons of the TaS_2 layer is found to be invalid. Instead one finds a strong coupling between the electronic structure and the magnetism. At low concentrations the Fe d_{z^2} levels are partially occupied while the Ta d_{z^2} levels are empty. Hence a channel of hopping through the Ta states facilitates a ferromagnetic alignment of Fe

spins. Fe favours a +2 valency, donating electrons to the fermi energy. Consequently with increasing Fe concentration, the Ta d_{z^2} states get occupied, removing the ferromagnetic channel for Fe spins. Further one also has a decreased separation of Fe spins in the ab-plane. This results in antiferromagnetism being favoured.

Bibliography

- [1] K. S. Novoselov, A. K. Geim, S. V. Morozov, D. Jiang, Y. Zhang, S. V. Dubonos, I. V. Grigorieva, and A. A. Firsov, *Science* **306**, 666 (2004).
- [2] B. Radisavljevic, A. Radenovic, J. Brivio, V. Giacometti, and A. Kis, *Nat. Nanotechnol.* **6**, 147 (2011).
- [3] Y. Zhang, J. Ye, Y. Matsushashi, and Y. Iwasa, *Nano Lett.* **12**, 1136 (2012).
- [4] Z. Yin, Hai Li, Hong Li, L. Jiang, Y. Shi, Y. Sun, G. Lu, Q. Zhang, X. Chen, and H. Zhang, *ACS Nano* **6**, 74 (2012).
- [5] H. Fang, S. Chuang, T. C. Chang, K. Takei, T. Takahashi, and A. Javey, *Nano Lett.* **12**, 3788 (2012).
- [6] A. Nag, K. Raidongia, K. P. S. S. Hembram, R. Datta, U. V. Waghmare, and C. N. R. Rao, *ACS Nano* **4**, 1539 (2010).
- [7] J. Dijkstra, P. J. Zijlema, C. F. van Bruggen, C. Hass and R. A. de Groot, *J. Phys. Cond. Matt.* **1**, 6363 (1989).
- [8] E. Morosan, H. W. Zandbergen, Lu Li, Minhyea Lee, J. G. Checkelsky, M. Heinrich, T. Siegrist, N. P. Ong, and R. J. Cava, *Phys. Rev. B* **75**, 104401 (2007).

- [9] M. D. Vannette, S. Yeninas, E. Morosan, R. J. Cava, and R. Prozorov, *Phys. Rev. B* **80**, 024421 (2009).
- [10] Y. J. Choi, S. B. Kim, T. Asada, S. Park, Weida Wu, Y. Horibe, and S-W. Cheong, *EPL* **86**, 37012 (2009).
- [11] M. Eibshutz, S. Mahajan, F. J. DiSalvo, G. W. Hull, and J. V. Waszczak, *J. Appl. Phys.* **52**, 2098 (1981).
- [12] H. Narita, H. Ikuta, H. Hinode, T. Uchida, T. Ohtani, and M. Wakihara, *J. Solid State Chem.* **108**, 148 (1994).
- [13] K. T. Ko, Kyoo Kim, Sung Baek Kim, H. D. Kim, J. Y. Kim, B. I. Min, J.H. Park, F.H. Chang, H. J. Lin, A. Tanaka, and S. W. Cheong, *Phys. Rev. Lett.* **107**, 247201 (2011).
- [14] S. S. P. Parkin, R. Bhadra, and K. P. Roche, *Phys. Rev. Lett.* **66**, 2152 (1991).
- [15] G. Kresse and J. Furthmüller, *Phys. Rev. B* **54**, 11169 (1996).
- [16] G. Kresse and D. Joubert, *Phys. Rev. B* **59**, 1758 (1999).
- [17] P. E Blöchl, *Phys. Rev.* **50**, 17953 (1994).
- [18] J.P. Perdew, J.A. Chevary, S.H. Vosko, K.A. Jackson, M.R. Pederson, D.J. Singh, and C. Fiolhais. *Phys. Rev. B* **46**, 6671 (1992).
- [19] J.P. Perdew, J.A. Chevary, S.H. Vosko, K.A. Jackson, M.R. Pederson, D.J. Singh, and C. Fiolhais. *Phys. Rev. B* **48**, 4978 (1993).
- [20] S. L. Dudarev, G. A. Botton, S. Y. Savrasov, C. J. Humphreys and A. P. Sutton, *Phys. Rev. B* **57**, 1505 (1998).

- [21] A. A. Mostofi, J. R. Yates, Y.-S. Lee, I. Souza, D. Vanderbilt and N. Marzari, *Comput. Phys. Commun.* **178**, 685 (2008).
- [22] C. Franchini, R. Kovacik, M. Marsman, S. Sathyanarayana Murthy, J. He, C. Ederer and G. Kresse, *J. Phys. Cond. Matt.* **24**, 235602 (2012).

Chapter 7

Engineering Polar Distortion in SrTcO_3

7.1 Introduction

The interest in multiferroics has grown enormously in recent years as concept devices are envisaged in which the strong coupling between the electric and magnetic degrees of freedom allows one to interchangeably use an electric field or a magnetic field to manipulate either degree of freedom [1,2]. One of the prerequisites for such a device is that one has a sizable polarization as well as a high magnetic ordering temperature in the material. Usually the route to a strong coupling between the two degrees of freedom has been that magnetism and ferroelectricity are both associated with the same atom. This is difficult to realize as among the transition metal (TM) compounds those materials that have a large value of polarization are those that have a d^0 electron configuration [3], and hence have no associated magnetism which requires partial d electron filling. Recently Bhattacharjee *et al.* [4]

pointed out that even in a d^3 system, which is a band insulator, one could stabilize ferroelectric distortions by expanding the lattice. The short-ranged coulomb repulsion decrease in this case, and this is believed to be the reason that the energy of the ferroelectric mode decreases with an increase in volume. Considering the case of CaMnO_3 , they examined various phonon modes, and found that while the energy of the antiferrodistortive mode remained volume-independent, the energy of the ferroelectric mode decreased with an increase in volume, becoming soft, and became comparable with that of the antiferrodistortive mode at a volume expansion of 2%. The ferroelectric structures stabilized at larger volumes were found to have large polarization, $\sim 4 \mu\text{ C/cm}^2$, comparable to that found in displacive ferroelectrics. They also indicated that similar behavior can be observed in other $\text{A}(\text{Sr},\text{Ba})\text{MnO}_3$ perovskites. First principles studies have been carried out for SrMnO_3 [5] and BaMnO_3 [6] with similar conclusions. Recent experiments by Sakai *et al.* [7] corresponded to the first experimental validation of the existence of *B-site driven* displacive multiferroism in $\text{Sr}_{1-x}\text{Ba}_x\text{MnO}_3$ through chemical engineering. This has also been demonstrated by Günter *et al.* [8] where they found incipient ferroelectric behavior in CaMnO_3 films with 2.3% strain. A basic route to high polarization materials has emerged from this approach, which was to choose band insulators. Distortions arising from first order Jahn-Teller effects are often found to be centrosymmetric and therefore these materials are not suitable for systems where one tries to explore polar distortions. However first order Jahn-Teller effects are not operative in band insulators and the lowest order distortions that are operative are second order in nature. These distortions could result in inversion symmetry being broken. In the present work we look at another member of this class of materials.

Magnetic members are rare among the compounds formed by $4d$ and $5d$ transition metal atoms. Even if some members are found to be magnetic, the typical ordering temperatures are low. Recently unusually high magnetic ordering temperatures were reported in few Tc-based transition metal oxides, far higher than their $3d$ counterpart. SrTcO_3 was found to have a Neel temperature of 1023 K [9] while CaTcO_3 was found to have a Neel temperature of ~ 800 K [10]. This was found to arise from the half-filling of the t_{2g} bands in these oxides. A model was proposed [11] that this was a generic feature of $4d$ and $5d$ oxides at half filling of the t_{2g} bands, and high magnetic ordering temperatures were to be expected for more examples among this class of materials. These $4d$ and $5d$ oxides also come into the category of band insulators and could be explored for ferroelectricity. In the present work we focus on SrTcO_3 which is an example of a $4d$ oxide with a Neel temperatures equal to 1023 K [9] and examined if the mechanism of considering band insulators [4] could drive the system ferroelectric. For the applicability of the idea presented earlier, we took experimental lattice parameters instead of idealized cubic structural parameters and subjected the system to bi-axial tensile as well as compressive strain. Within the strain range explored, we did not find any signature of polar distortions.

Recent theoretical work by Gupta et. al. [12] have shown that for the case of $\text{BaVO}_3/\text{BaTiO}_3$ two dimensional heterostructures(HS), one can stabilize polar distortions in apparently non-ferroelectric BaVO_3 layers. Here also we have investigated the scenario where one forms a HS with intrinsically ferroelectric substrate of BaTiO_3 . In both the cases of monolayer and bilayer HS, we are able to stabilize out of plane polar distortions within the SrTcO_3 layers. We then ask the question, what are the microscopic considerations which allow polar distortions to be stabilized. Within our calculations we have explored the possible role of quantum confinement, Born-effective charges

and breaking of the inversion symmetry to stabilize the polar distortions in monolayer HS. Additionally the role of asymmetry in the hopping strength to stabilize the polar distortions in bilayer HS have been discussed.

7.2 Methodology

First principle electronic structure calculation have been performed within a plane wave implementation of density functional theory using projector augmented wave potentials [13] as implemented in the Vienna *ab initio* simulation package (VASP) [15]. Perdew-Burke-Ernzerhof (PBE) [15] forms of the generalized gradient approximations to the exchange correlation functional were used. Monkhorst-Pack grid of $8 \times 8 \times 8$ k-points mesh were chosen for the self-consistent calculation of the bulk structures. The wave function taken in the basis set consists of plane waves with kinetic energies less than or equal to 500 eV. Bulk SrTcO₃ favours G-type anti-ferromagnetic structure as the magnetic ground state. We maintained the same magnetic configuration in the bulk calculations. The polarization were calculated using the Berry phase method [16]. The Born effective charges have been computed using the DFPT method as implemented in VASP [17,18] which involves the computation of change in Hellmann-Feynman forces due to the change in wave function.

Multilayer HS of SrTcO₃ with BaTiO₃ as the substrate have been generated from the bulk super-cell of BaTiO₃ grown along c direction. We have started with sixteen monolayers of bulk BaTiO₃ and have substituted one BaO and TiO₂ layers with SrO and TcO₂ layers while maintaining experimental bulk lattice constant of BaTiO₃ to generate the first type of HS. We call this monolayer HS throughout the discussion. Similarly one BaO and two symmetric

TiO₂ layers have been substituted with SrO and TcO₂ layers respectively to generate bilayer HS. Monolayer and bilayer HS have been shown in Figure 7.1. In the experimental bulk structure, SrTcO₃ shows rotation ($a^- a^- c^0$) and tilts ($a^- a^- c^+$) of the octahedra. We also have taken care of such tilts and rotations while constructing HS. Monkhorst-Pack k points grid of $8 \times 8 \times 2$ have been chosen to span the Brillouin zone. Antiferromagnetic configuration for the in-plane magnetic ions in monolayer HS and G-type antiferromagnetic structure in bilayer HS have been maintained. Other calculation details including energy cut-off for the plane waves in the basis set and GGA for the exchange correlation functional are identical to the bulk calculations.

7.3 Results and Discussions

Earlier work [4] showed that band insulators showed a tendency to off-center. As a measure of the tendency of a material to exhibit polar distortions, we calculated the Born effective charges(BEC) for Sr, Tc and O. The z-component of the BEC's are given in Table 7.1. The in-plane oxygens have been denoted as O_⊥ and the apical oxygens have been denoted as O_∥. Examining the BEC's for the theoretically optimized pseudo-cubic structure, we find values of 2.7, 6.42, -5.79 and -1.66 associated with Sr, Tc, O_∥ and O_⊥ respectively. Now the formal valencies associated with these atoms are +2, +4, -2 and -2 respectively. The value for Sr here is similar to the value found for other alkaline earth metal atoms such as Ca in CaMnO₃ and Ba in BaMnO₃ [6] and is close to the formal valency of the system. However the values for Tc and O_∥ are found to be significantly enhanced from the formal valencies expected. Enhanced values of the BEC's have always been seen in systems which are incipient ferroelectrics or are ferroelectrics. In the case of

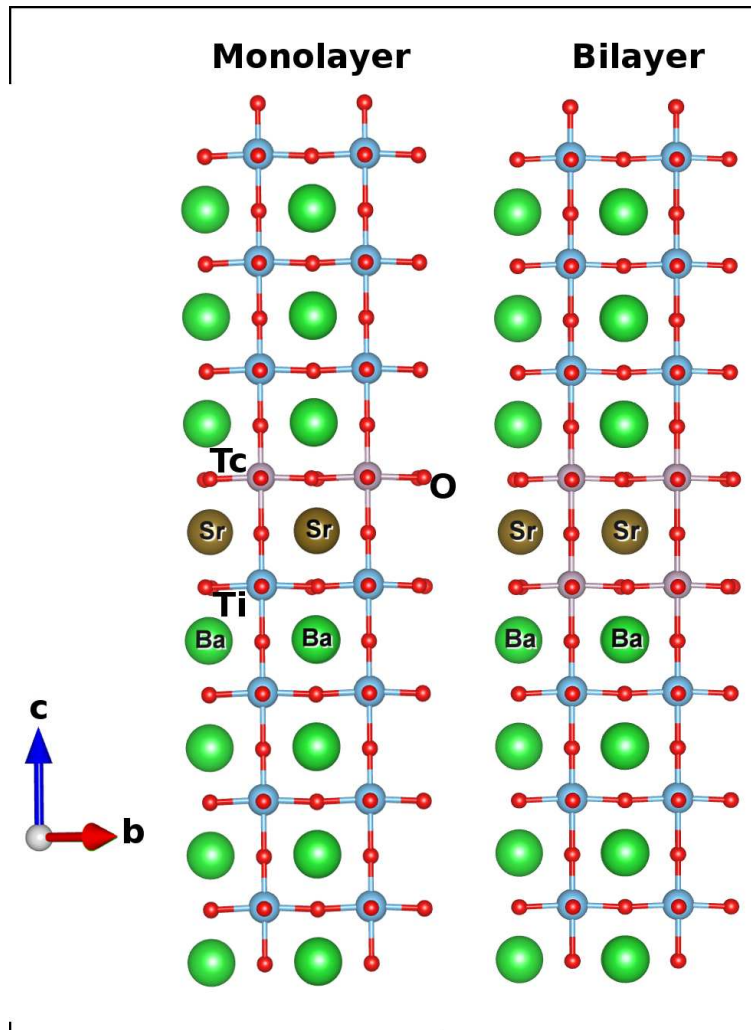


Figure 7.1: Monolayer and bilayer heterostructures of $\text{SrTcO}_3/\text{BaTiO}_3$ have been generated from the bulk supercell of BaTiO_3 grown along the c direction

the classic ferroelectric, BaTiO_3 one finds that Ti and O_{\parallel} have BEC's which are equal to 7.29 and -5.75 [19], and similar enhancements have also been seen in the recently predicted multiferroics, SrMnO_3 and CaMnO_3 . These results therefore suggest that the present system could also be a potential multiferroic.

Site index	Volume reduced	Optimized volume	Volume enhanced
index	by -2%	($a_o=3.942\text{\AA}$)	by +2%
Z_{Sr}^*	2.73	2.70	2.66
Z_{Tc}^*	6.22	6.42	6.64
$Z_{O_{\parallel}}^*$	-5.61	-5.79	-5.97
$Z_{O_{\perp}}^*$	-1.66	-1.66	-1.66

Table 7.1: Born effective charges of different atoms calculated for a cubic unit cell of SrTcO₃ as a function of volume.

The next question we asked was whether one can stabilize polar distortions in SrTcO₃. The experimentally reported structure for SrTcO₃ does not have ferroelectric distortions. In order to check whether it develops any polar distortions under strain we have considered the situations where the bulk structure is subjected to bi-axial tensile as well as compressive strain. We have explored strain in the regime of 2% or less as SrTcO₃ becomes metallic beyond this tensile strain regime. Within our calculations we were not able to find the stability of any polar distortions.

An alternate route in this context could be the HS formed by sandwiching transition metal oxide layers between a conventional ferroelectric. BaTiO₃ is one such example where the Ti off-centering results in Ti-O bond lengths equal to 1.88 Å and 2.12 Å. Recently in a theoretical study [12], Gupta et al. have sandwiched BaVO₃ in between BaTiO₃. BaVO₃ has V in d¹ configuration and is a Jahn-Teller active ion. Usually one expects symmetric distortions which lift the degeneracy of the d orbitals. One thus does not expect polar distortions to survive. Nevertheless they were able to stabilize polar distortions along the growth direction while first order Jahn-Teller distortions were found in the ab plane of the optimized structure. The question

that followed was whether moving from a formal occupation of d^1 at the transition metal site to d^3 would still allow the off-centering. While the d^3 case, as discussed earlier would not have first order Jahn-Teller effects, the increased electron count at the transition metal site would increase the Coulomb repulsion between electrons on the transition metal and oxygen. Monolayer HS as discussed in the methodology section have been generated with two layers of SrTcO_3 sandwiched between fourteen layers of BaTiO_3 . After complete structural relaxations we arrive at a structure where polar distortions are stabilized in the sandwiched layer. The out of plane Tc-O bond lengths are found to be 1.99 and 2.05 Å while the in-plane bond lengths remain fixed at 2.00 Å and the direction of polar distortions is the same as that of the substrate BaTiO_3 layer. Moreover we did not observe any tilt or rotation of the TcO_6 octahedra originally present in the starting structure.

In order to understand the origin of polar distortions in the sandwiched layer, we have calculated the the density of states(DOS). Figure 7.2 shows the spin and orbital projected DOS for Tc d orbitals in monolayer HS. In the octahedral environment of the oxygens the five d orbitals split into t_{2g} and e_g symmetry. Tc is in +4 oxidation state and the majority spin t_{2g} orbitals are occupied at a Tc site. We further noticed that there is a distinct difference between the bandwidth of the occupied DOS coming from three different orbitals. While the d_{xy} orbital is pretty delocalized and spreads over around 1.5 eV energy window, other two orbitals are localized with a dispersion width of around 0.5 eV only. To compare our results with the bulk DOS, we have plotted Tc t_{2g} orbital projected DOS in the Figure 7.3. The main difference between two DOS is very evident. In bulk SrTcO_3 all of the Tc t_{2g} majority spin channels are completely occupied and the width associated with each of these three orbitals are found to be around 2 eV. The significant hopping interaction between Tc t_{2g} and O p is responsible for the bandwidth that we

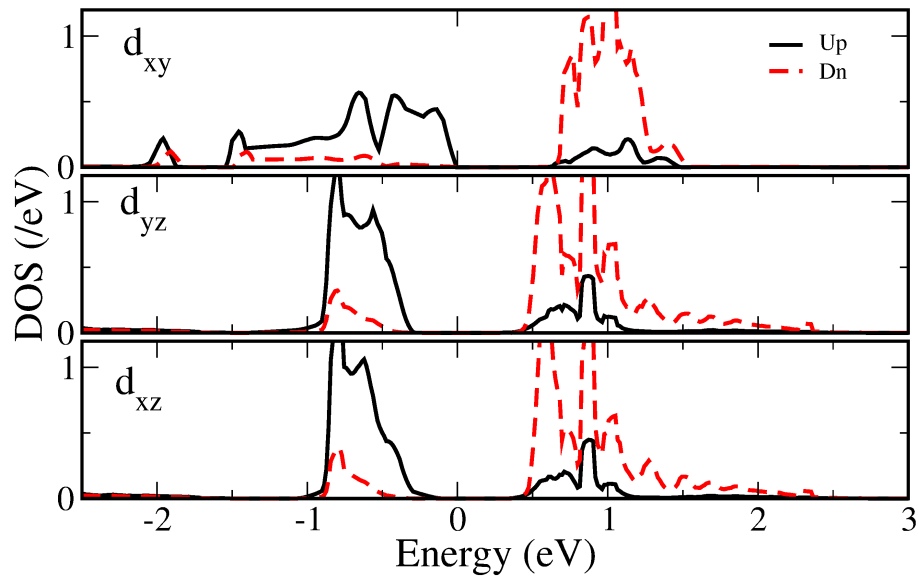


Figure 7.2: Spin and orbital projected DOS of Tc d states with t_{2g} symmetry in monolayer heterostructure of $\text{BaTiO}_3/\text{SrTcO}_3$.

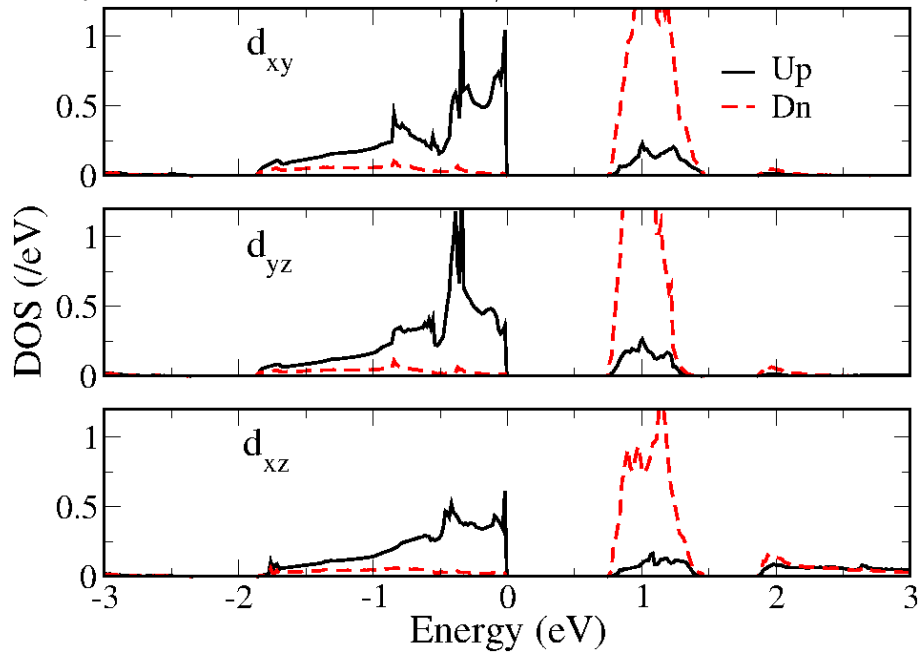


Figure 7.3: Spin and orbital projected DOS of Tc d states with t_{2g} symmetry in bulk structure.

find. However in the monolayer HS, dispersion width is reduced significantly for both d_{yz} and d_{xz} orbitals. This immediately points out that the hopping interactions between Tc d_{yz} or d_{xz} and apical O p orbitals are limited in the HS. The presence of TiO_2 layer along the growth direction thus have limited the hopping of electrons within the sandwiched layers. However this is not the situation in the basal plane where an electron from Tc t_{2g} orbitals is allowed to hop without any constraint. This confinement of electrons along the growth direction can be compared to the situation of a particle in a box and is often discussed in terms of quantum confinement effect. Looking at the occupied DOS peaks corresponding to the majority Tc d_{yz} and d_{xz} orbitals we found that they are pushed down around 0.75 eV below the Fermi level again for the same reason.

Discussion mentioned above clarifies the role of host layers to limit the electronic hopping and thus promoting quantum confinement effect. But does it play any role to stabilize polar distortions in the sandwiched layer? In order to find that we have looked at the distortions in the host layers also. Polar distortions are found to survive within the host layer though the magnitude has reduced from their bulk values and are found to be 2.07 and 1.94 Å. Usually whenever one grows layers of non polar material within a polar structure, there is a competition between the polar and non-polar structure at the interface and the host layer loses some of its polarization in the process. To check whether the polarization in the sandwiched layer have been induced directly by the substrate layer, we explored the scenario where the polarization in the substrate is expected to vanish. Under the bi-axial tensile strain bulk BaTiO_3 is known to lose ferroelectricity. A shorter Tc-O bond length significantly enhances the Coulomb repulsion between electron clouds on Tc and O and the short range repulsion becomes strong enough to destabilize polar distortions [20] in the structure. We then examined the case where the sub-

strate was subjected to 2% biaxial tensile strain. The atomic positions were relaxed again and one found that the polar distortions associated with the substrate vanished while they remained in the sandwiched layer. It is worth mentioning that the lattice parameters along the growth direction have been reduced to satisfy the Poisson's ratio. This result of sustainable polarization in the sandwiched layer while it vanishes in the host clearly eliminates the speculation of polarization directly being induced by the host layers and one should think of other mechanisms to be operative.

There are two other factors that could lead to the polar distortions in such a HS. One is the inversion symmetry being broken by the nature of the structure and another is the tendency to off-center as evident from the enhanced Born effective charges. As presented in Table 7.1, BEC associated with Tc and O_{\parallel} are fairly enhanced from their formal valencies and could lead to polar structures. If the enhanced BECs were the only origin, then one expects the off-centering to take place even when one has no inversion symmetry breaking. Indeed we checked the effect of breaking the inversion symmetry by replacing the SrO layer with BaO. The polar distortions were found to vanish in such a situation. This implies that there is an important role being played by the breaking of inversion symmetry to stabilize the polar distortions in monolayer HS.

After understanding the origin of polar distortions in monolayer HS, we move to investigate the scenario where another layer of TiO_2 has been substituted with a TcO_2 layer. The TiO_2 layer is chosen so that the two TcO_2 layers are symmetrically placed with respect to the SrO layer. We call this a bilayer HS. Full structural relaxations lead to a structure where the out-of-plane Tc ions come closer to each other. This results in two short Tc-O bonds of length 1.99 Å while the other out-of-plane Tc-O bond lengths are 2.05 Å. These

Monolayer		Bilayer	
No Strain	2% biaxial	No Strain	2% biaxial
2.05Å	1.98Å	2.05Å	1.98Å
1.99Å	1.92Å	1.99Å	1.92Å
		1.99Å	1.98Å
		2.05Å	1.92Å

Table 7.2: Polar distortions in BaTiO₃/SrTcO₃ heterostructure. Tc-O bond lengths along c direction have been tabulated for monolayer as well as bilayer structure.

bond lengths have been given in Table 7.2. According to our nomenclature we call this AFE1 bilayer HS. It is clear from the table that though the magnitude of displacement corresponding to each Tc ion has not changed from the monolayer structure, the direction of out of plane displacements are opposite. Moreover the host layers are found to be non-polar even without any strain. An additional biaxial strain retains the AFE1 distortions within the dopant layer and the polar distortions remain absent in the host layers.

To understand the mechanism involved in stabilizing polar distortions in the bilayer HS we have plotted spin and orbital projected DOS corresponding to Tc d states in the Figure 7.4. The main feature of the DOS is the resurrection of the dispersion width corresponding to d_{yz} and d_{xz} states, whereas the width associated with Tc d_{xy} orbital remains unchanged when compared to the monolayer environment. The only reason that could be responsible for this change in the DOS is the introduction of second TcO₂ layers symmetric to the SrO layers which enhances the out-of-plane hopping interactions and an electron from Tc now can hop to intermediate apical O and then to the next out of plane Tc ion. There is no such change within the basal

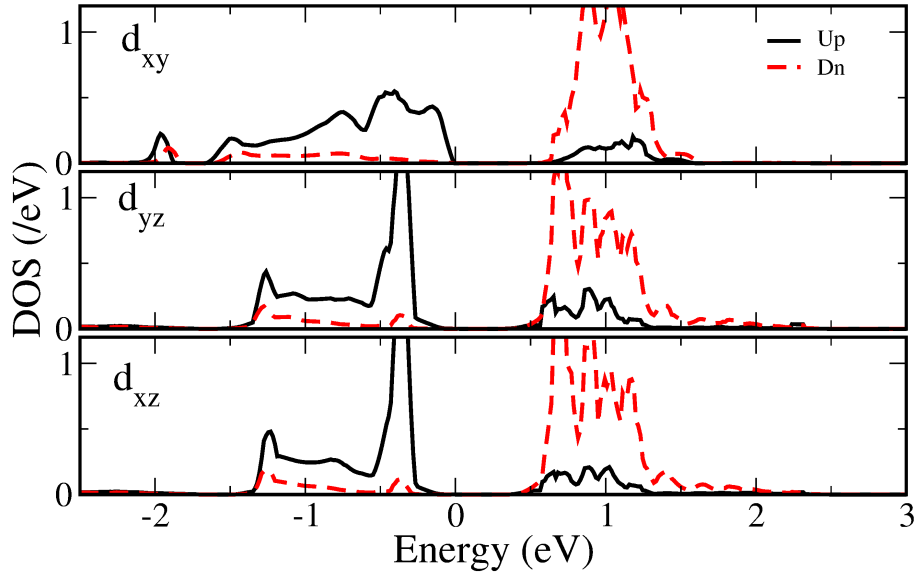


Figure 7.4: Spin and orbital projected DOS of Tc d states with t_{2g} symmetry in bilayer heterostructure of BaTiO₃/SrTcO₃.

plane which is reflected from the character of Tc d_{xy} DOS. In contrast to the monolayer situation where the hopping possibilities along the growth direction was very weak and the Coulombic repulsive force was effectively operative, here we have a competition between these two energetics. A slight displacement of Tc ions towards the intermediate apical oxygen enhances both the hopping possibilities as well as the Coulombic repulsion. But the amount of energy gain from the enhancement of hopping surpass the loss due to the Coulomb repulsion. At this juncture one should remember that the hopping strengths between Tc and O towards the TiO₂ layers remain limited. Any displacement of Tc ions towards that direction should cost in energy thus is not favoured. Consequently, the asymmetry associated with the hopping promotes a structure where both Tc ions move towards the intermediate apical oxygen. In Figure 7.5 we have shown the asymmetry

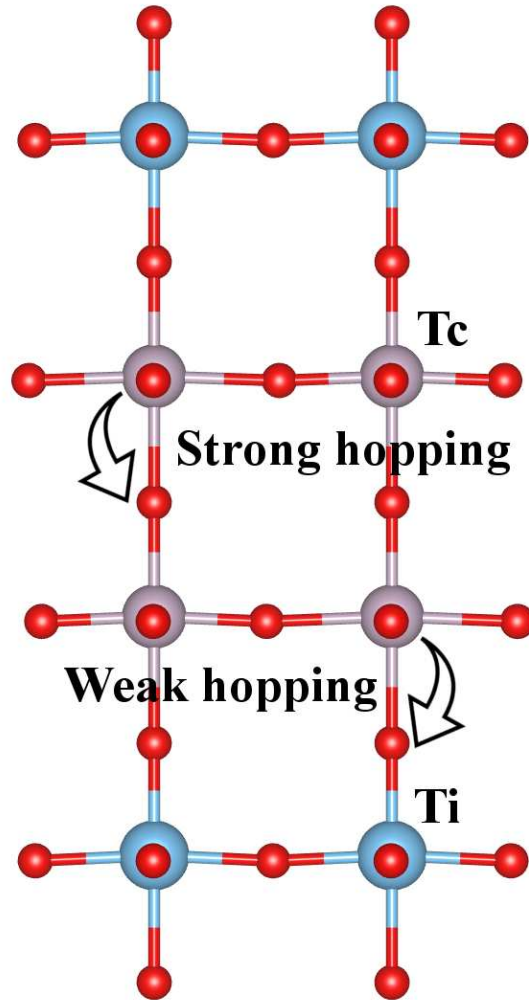


Figure 7.5: Different hopping strengths in different directions lead to an AFE1 structure.

in hopping along two different directions which is responsible for the AFE1 structure.

To further establish the validity of the mechanism presented above, we have performed total energy calculations corresponding to different types of distortions that one can have in a bilayer HS. There are three such possibilities. The first one is ferroelectric(FE) distortions where both out of plane Tc ions

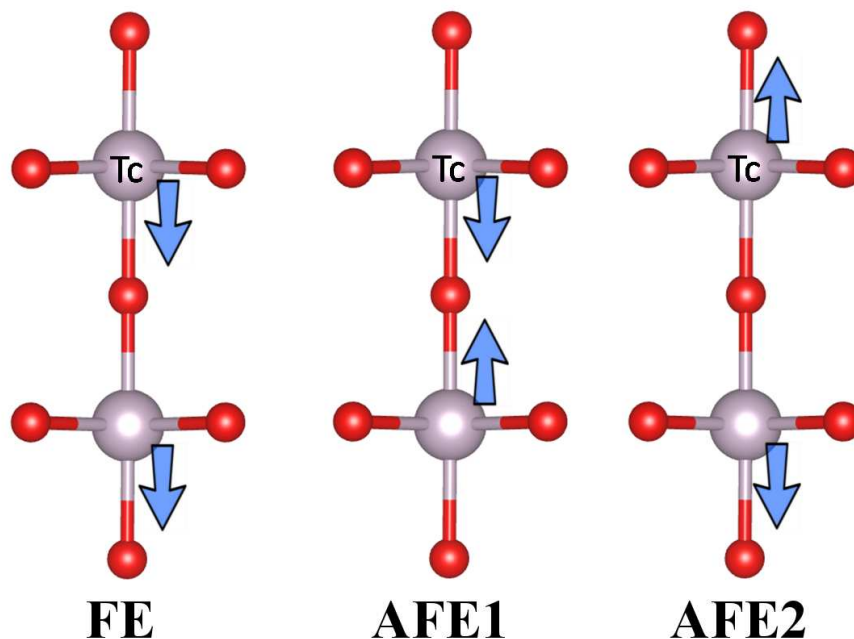


Figure 7.6: Different types of distortions in bilayer HS. Movement of Tc ions from the ideal position has been indicated with arrows.

move towards one of the interface. This results in a long-short-long-short arrangement of out of plane Tc-O bond lengths. Next one is AFE1 distortions. The third one is AFE2 distortions where both the Tc ions move towards the nearest interface. Figure 7.6 shows the movement of out of plane Tc ions in three different bilayer HS. To compare the ground state energies corresponding to a specific magnitude of displacement we have kept the out-of-plane Tc displacement fixed to 0.05 \AA while all other position coordinates are set free to relax. One should note that the displacement applied in different model structures is chosen such that it matches closely the displacement noticed in the relaxed AFE1 HS. A comparison between these three ground state energies shows that the structure with AFE1 type of distortions is the most favourable one with the gain of 101 meV compared to the least favoured

AFE2 structure. FE structure is also favoured by 42 meV when compared to AFE2 structure. Considering the fact that there is a gain from the enhanced hopping by the movement of Tc ions towards the intermediate apical O, AFE1 type of distortions gains the most. In AFE2 distortions, both Tc ions move in opposite directions to the movement of Tc in AFE1 and so the loss corresponding to such movement is the most. In the FE structure while we have gain from the movement of one of Tc ion towards the intermediate apical O, movement of other one decreases the energy and thus have intermediate total energy.

7.4 Conclusion

In this chapter, we have explored $4d$ transition metal oxide SrTcO_3 for magneto-electric applications. Despite of having enhanced BEC, bulk structure did not show any ferroelectric distortions. Biaxial tensile and compressive strain are also found to be incapable of introducing such distortions. However HS with BaTiO_3 as substrate layers have been found to be very promising route. In monolayer HS we are able to stabilize polar distortions. Host layers are found to limit the electronic hopping within the sandwiched layer resulting in quantum confinement effect along the growth direction. Additionally, symmetry breaking mechanism associated with the structure stabilizes polar distortions along the same direction that one have in the host layers. In bilayer HS, ground state is found to have polar distortions designated as AFE1. This emerges from the asymmetry in hopping along two opposite directions. Considering total energy calculations for three different types of distortions that one can have in bilayer HS, we further have established the validity of our proposed mechanism.

Bibliography

- [1] N. A. Spaldin and M. Fiebig, *Science*, **309**, 391 (2005).
- [2] J. F. Scott, *Nat. Mater.*, **6**, 256 (2007).
- [3] N. A. Hill, *J. Phys. Chem. B*, **104**, 6694, (2000).
- [4] S. Bhattacharjee, E. Bousquet and P Ghosez, *Phys. Rev. Lett.*, **102**, 117602 (2009).
- [5] J. H. Lee and K. M. Rabe, *Phys. Rev. Lett.*, **104**, 207204 (2010).
- [6] J. M. Rondinelli, A. S. Eidelson and N. A. Spaldin, *Phys. Rev. B*, **79**, 205119 (2009).
- [7] H. Sakai, *Phys. Rev. Lett.*, **107**, 137601 (2011).
- [8] T. Günter, E. Bousquet, A. David, Ph. Boullay, Ph. Ghosez, W. Prellier and M. Fiebig, *Phys. Rev. B*, **85**, 214120 (2012).
- [9] E. E. Rodriguez, *Phys. Rev. Lett.*, **106**, 067201 (2011).
- [10] M. Avdeev, G. J. Thorogood, M. L. Carter, B. J. Kennedy, J. Ting, D. J. Singh and K. S. Wallwork, *J. Am. Chem. Soc.*, **133**, 1654 (2011).
- [11] S. Middey, A. K. Nandy, S. K. Pandey, P. Mahadevan and D. D. Sarma, *Phys. Rev. B*, **86**, 104406 (2012).

- [12] K. Gupta, *Electronic, Magnetic and Structural Properties of Transition Metal Oxides*, (2012).
- [13] P. E. Blöchl, *Phy. Rev. B*, **50**, 17953 (1994); G. Kresse and D. Joubert, *Phys. Rev. B*, **59**, 1758 (1999).
- [14] G. Kresse and J. Furthmuller, *Phys. Rev. B*, **54**, 11169 (1996).
- [15] J. P. Perdew, K. Burke and M. Ernzerhof, *Phys. Rev. Lett.*, **77**, 3865 (1996).
- [16] R.D. King-Smith and D. Vanderbilt, *Phys. Rev. B*, **47**, 1651 (1993).
- [17] S. Baroni and R. Resta, *Phys. Rev. B*, **33**, 7017, (1986).
- [18] M. Gajdos, K. Hummer, G. Kresse, J. Furthmuller and F. Bechstedt, *Phys. Rev. B*, **73**, 045112 (2006).
- [19] P. Ghosez, X. Gonze, P. Lambin, and J. P. Michenaud, *Phys. Rev. B*, **51**, 6765-6768 (1995).
- [20] R. E. Cohen, *Nature* **358**, 136 (1992).

Chapter 8

Metallic Antiferromagnetic State in Electron Doped NaOsO_3

8.1 Introduction

The microscopic origin of metal insulator transitions(MIT) in strongly correlated systems remains one of the standing problems within condensed matter physics [1]. MIT in these materials have been often understood within the Hubbard model. In such model a competition between the localizing effect dictated by the on-site Coulomb energies(U) and the delocalization effect controlled by the bandwidth W determines the metallicity of the material. While the system is insulating for high values of U/W , it becomes metallic when the ratio drops below a critical limit. There are lot of example exists for 3d transition metal compounds which are insulating in nature but this numbers

Part of this chapter is based on Phys. Rev. B, **89**, 134416 (2014).

decreases drastically for the 4d and 5d compounds. The larger spatial extent and additional screening effects present in 4d/5d metals leads to a larger bandwidth and reduced Coulomb correlation strengths. Thus one expects a smaller value of U/W for these materials resulting in them being metallic. Simplicity of this model does not take into account magnetic correlations. Slater in his seminal paper [2] on the other hand had proposed a completely different route of magnetically driven MIT. According to Slater's description, commensurate anti-ferromagnetic (AFM) order with every neighboring spin oppositely aligned, occurs at the MIT temperature. This creates an opposite periodic potential on each nearest neighbour resulting in an energy gap in the modified magnetic Brillouin zone.

Slater insulators have been studied for more than fifty years as insulators with special properties. Despite having theoretical and experimental search of Slater mechanism driven MIT in cuprates [3], pyrochlores [4] there was no definitive evidence of such material. Theoretical investigation of Weber et. al. [3] has shown that long range magnetic order results in a MIT in case of NdCuO_4 . Experimental observation [5–7] showed that Na_2IrO_3 has an AFM insulating ground state with a zigzag spin alignment below the Neel temperature. Though there is no direct evidence of Slater mechanism in Na_2IrO_3 , recent theoretical studies [8] have predicted it to be a Slater insulator below MIT temperature. Recently MIT have been found in 5d transition metal oxide NaOsO_3 [9]. It was a surprise that the magnetic transition temperature associated with NaOsO_3 was very high (410 K) as the local magnetic moments in such oxide were expected to be very small because of the wide bands that they form. Recent neutron and x-ray scattering results [9, 10] have probed long range magnetic order at the MIT and determined the nature of that order on a microscopic level. NaOsO_3 thus has been presented as the first definitive experimental example of a Slater insulator. The basic

electronic structure of NaOsO_3 has been calculated before [11–13]. Despite a 5d transition metal compound, the effect of spin-orbit coupling strength has been found to be insignificant. The states near the Fermi level seem to be strongly itinerant with a strong admixture of Os d and O p thus suggesting an itinerant model for magnetism. The effect of on-site Coulomb repulsion force (U) on the band structure found to be significant but a reasonable U alone has been found to be incapable of opening the gap [12]. Work by Jung et al. [13] showed that for an idealized cubic perovskite structure of NaOsO_3 a small rotation of OsO_6 octahedra leads to the stabilization of insulating state as well as G-type antiferromagnetism. Thus the microscopic driving force for the magnetic ordering and the accompanying MIT remains unclear. The recent model [14] for magnetism in NaOsO_3 analyzed the variation of effective exchange interaction strength J_0 as a function of U . Under the formalism of multiband Hubbard model [14] it has been shown that in the U - J_0 parameter space, NaOsO_3 lies in the rising part of the curve and there is scope of finding a different 5d oxide with higher Neel temperature. The half filling implies that a nesting mechanism is operative which drives the system AFM and insulating. This has been shown within the model calculations for NaOsO_3 . In this chapter we have examined the scenario away from the half filling where the nesting mechanism is not expected to be operative. With a slight amount of electron doping, a rare G-AFM metallic state has been realized. This G-AFM state is found to be very robust with the increment of dopant and we are able to stabilize G-AFM metallic state even at the 50% doping concentration. Magnetism in such structures have been described with the help of Heisenberg model and the contribution from different exchange pathways have been analyzed to understand the stability of magnetic ordering away from the half filling.

8.2 Methodology

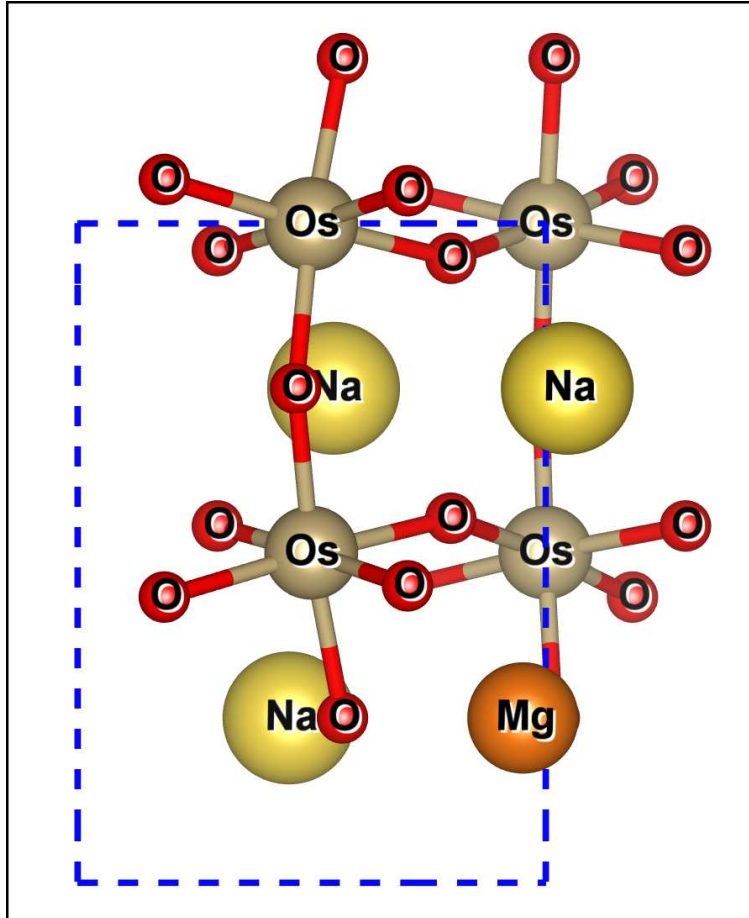


Figure 8.1: Structure of $Mg_{0.25}Na_{0.75}OsO_3$.

First principle electronic and magnetic structures of $NaOsO_3$ and electron doped $NaOsO_3$ have been calculated within a plane wave implementation of Density Functional Theory (DFT) using projector augmented wave (PAW) potentials as implemented in VASP [15]. Perdew-Burke-Ernzerhof (PBE) [16] forms of the generalized gradient approximations to the exchange correlation functional were used. In addition to the PBE form for the exchange correlation functional orbital-dependent potentials on Os within the GGA+U framework using the Dudarev implementation [17] have been used. Monkhorst-

Pack grid [18] of $6 \times 6 \times 6$ k-points mesh were chosen for the self-consistent calculations of the bulk structures. The wave function taken in the basis set consists of plane waves with kinetic energies less than or equal to 450 eV. Lattice constants were kept fixed at the experimental orthorhombic structural parameters of NaOsO_3 , while the internal coordinates were optimized until an energy convergence of 10^{-5} eV along with the force convergence of 5 meV/Å were met. Figure 8.1 shows the experimental structure of NaOsO_3 .

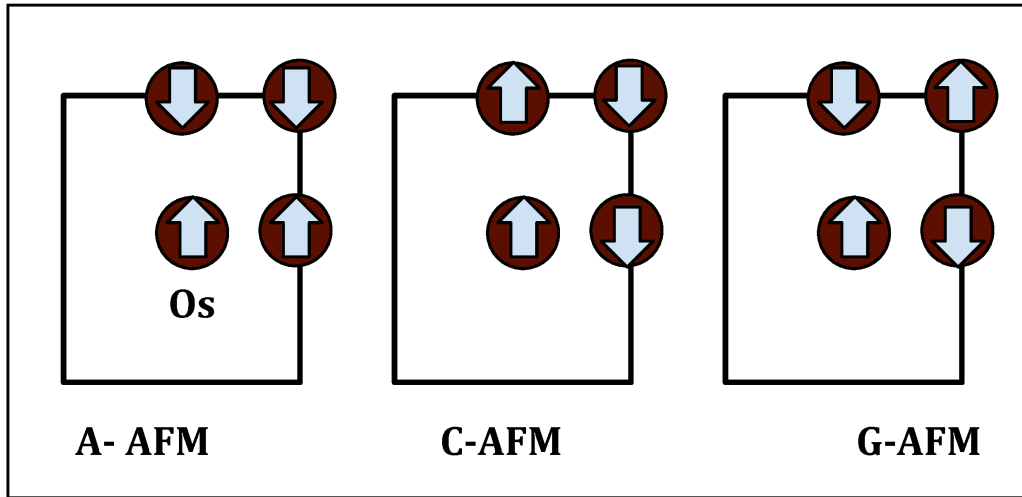


Figure 8.2: Different collinear AFM configurations.

The robustness of the magnetic stability with electron doping have been examined by considering supercells of NaOsO_3 and substituting monovalent Na atoms by bivalent Mg. This doping corresponds to an enhanced electron occupancy at the Os site. Considering the example of 20 atoms supercell, substitution of one of the Na ion with one Mg results in an average of 3.25 electrons per Os site. Various collinear magnetic configurations have been considered to analyze the stability of G-type antiferromagnetism as a function of doping concentration. In Figure 8.2 we have shown various magnetic configurations schematically. Spin-orbit interaction strengths are expected

to be large for the 5d transition metal compounds and so have been included while calculating the stability. Magnetic structures of NaOsO₃ and Mg doped NaOsO₃ have been analyzed with the help of classical Heisenberg spin model. Magnetic energies for such model is given by $-\frac{1}{2} \sum_{ij} J_{ij} \mathbf{s}_i \cdot \mathbf{s}_j$, where J_{ij} is the exchange interaction strength corresponding to the spin state \mathbf{s}_i and \mathbf{s}_j at lattice site i and j respectively. A +ve/-ve exchange interaction strength corresponds to FM/AFM interactions between interacting sites. We have employed the frozen magnon approximation to find out exchange interaction strengths. In such approach, the energy corresponding to each spin spiral state \mathbf{q} is equivalent to a magnetic configuration represented by the unit vector given by $(\sin(\theta) \cdot \cos(q \cdot R_i), \sin(\theta) \cdot \sin(q \cdot R_i), \cos(\theta))$. R_i is the position vector w.r.t the chosen origin and θ is the spin angle made with z axis. In reciprocal space it can be shown that the magnetic energy is given by $E(\theta, q) = E_0(\theta) - \text{Sin}^2\theta J(q)$. Magnetic energies at various q points are calculated from the total energy calculations to map out the spin wave dispersion. For the sake of simplicity all calculations are constrained in the $\theta = \pi/2$ plane only. An inverse Fourier transformation is then applied to find out real space exchange interaction strengths. Exchange parameters calculated such way then undergo a least square error minimization subroutine to estimate the best set entering into the Heisenberg model with the least number of parameters. A comparison between exchange interaction strengths extracted from our model have been discussed to analyze the effect of doping.

8.3 Results and Discussions

8.3.1 Electronic Structure Analysis

In recent studies [10] NaOsO₃ have been found to be the first example of Slater insulator. According to Slater's description of magnetically driven MIT, AFM ordering with oppositely aligned spin neighbours occurs at the MIT temperature. This spin alignment creates an opposite periodic potential on each nearest neighbour resulting in an energy gap in the magnetic Brillouin zone boundary. Thus the AFM ordering driven by such nesting of the Fermi surface plays an important role in the gap opening in such insulators. Nevertheless one should remember that the mechanism described is strictly operative at the half-filling of the orbitals. In NaOsO₃, Os is in +5 oxidation state which corresponds to the half filling of the d orbitals with t_{2g} symmetry. In Figure 8.3 we have shown Os d partial density of state for G-type AFM structure obtained from our ab initio calculations for U=1 eV on Os site. Main contribution from t_{2g}/e_g majority and minority spin channels have been labeled for the ease of understanding. As evident from the DOS that t_{2g} majority channels are completely occupied, whereas minority channels are empty. States corresponding to e_g symmetry are higher in energy and does not contribute near the Fermi energy. The band gap is in between t_{2g} majority and minority spin channels.

Orbital filling should be important in a model where the magnetism is nesting driven. In order to check the scenario away from the half filling we started doping electrons into the system. To do so, monovalent Na ions have been substituted with bivalent Mg ions. Thus corresponding to each substitution of Na ion, we dope one electron into the system. The most diluted doping(2.8%) limit we considered is one electron in every thirty six Na ions. At

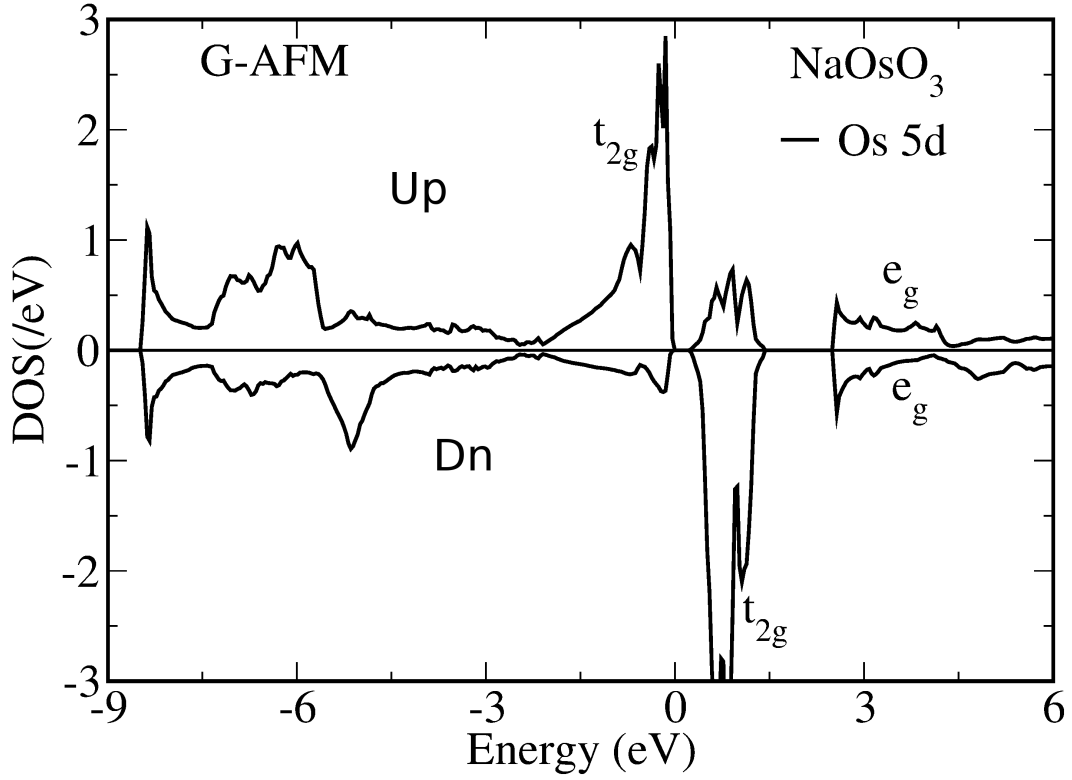


Figure 8.3: Os d orbital and spin projected DOS in NaOsO_3 within ab initio calculation with $U=1$ eV on Os.

this limit we stabilize a structure which is G-type AFM. Magnetic moment on Os is found to be $1.3 \mu_B$. This value is exactly the same as reported [14] for the magnetic moment of Os in NaOsO_3 . Atom projected partial DOS is presented in the Figure 8.4. In the majority spin channel we have the main contribution coming from Os t_{2g} orbitals. There are finite states in the Fermi level contributed by the minority Os d orbitals with t_{2g} symmetry and thus the structure is metallic in nature. There is a significant admixture between Os d and O p states near the Fermi level but the main contribution from the O p states are nearly 3 eV deeper to the Fermi level. We went on enhancing the doping concentrations and analyzed the stability of such magnetic ordering. The magnetic stabilization energies for the G-Type AFM configurations

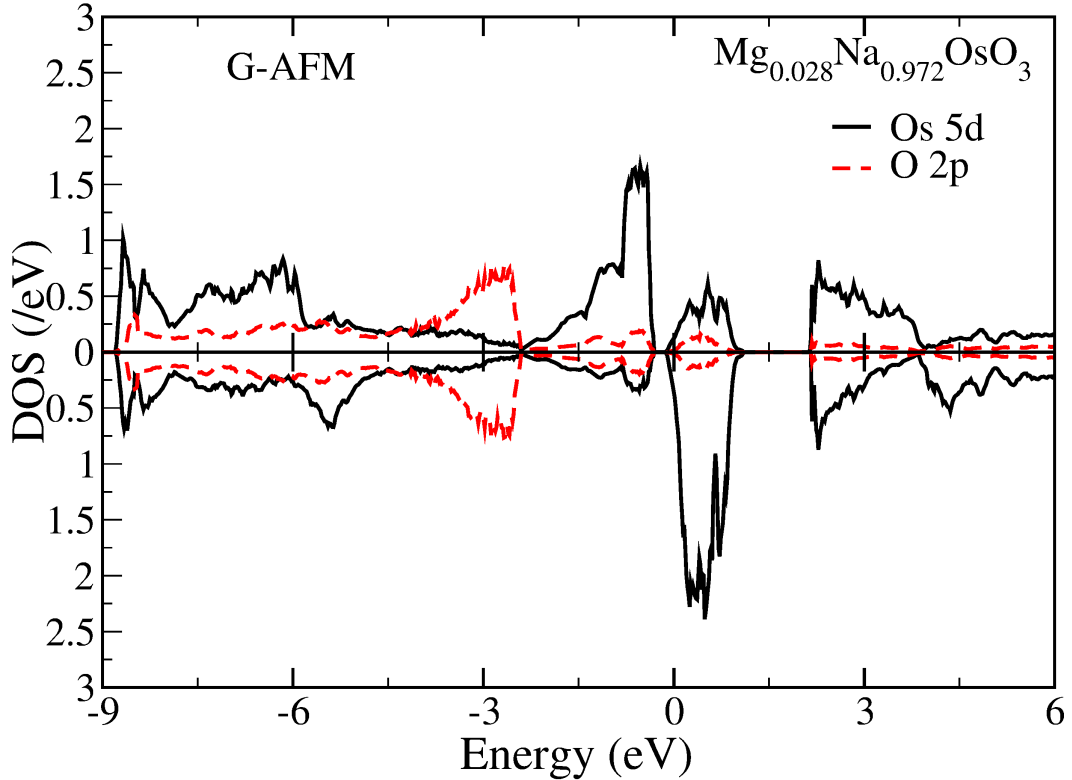


Figure 8.4: Spin polarized atom projected partial DOS for $Mg_{0.028}Na_{0.972}OsO_3$ within the ab initio calculation with $U=1$ eV on Os.

at 25% and 50% doping concentrations calculated from our ab initio calculations are given in the Figure 8.5. In each case energies are referenced to the other AFM configurations. G-AFM is found to be the magnetic ground state for both doping concentrations. We further find an almost linear variation of stabilization energy with the doping. With an increase in electron doping, the difference in energy between magnetic configurations decreases and for 50% doping C-type and G-type AFM configurations are almost degenerate. Spin-orbit interactions are believed to be significant in 5d transition metal oxides and could be of the same strength as the intra-atomic exchange interaction strength. Consequently we went on to examine if the inclusion of

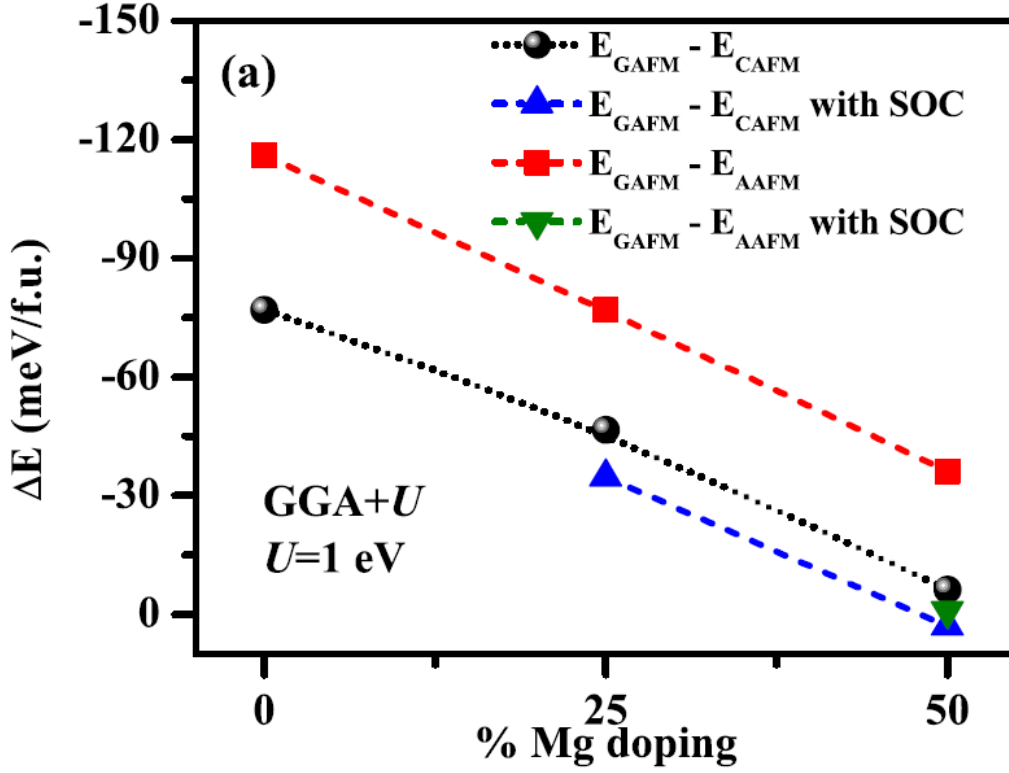


Figure 8.5: Variation of magnetic stabilization energy of G-AFM with different doping concentrations.

spin-orbit interaction strength modifies the trend we had in the absence of it. A similar trend in the magnetic stabilization energies was found with the G-AFM spin configuration as the ground state. Magnetic moment on Os has also been calculated and again found to be identical as reported for the case of NaOsO_3 [14].

To show how the density of states change with the doping concentrations we have compared the Os d partial density of states within the ab initio calculations for $U=1$ eV at Os site and have plotted in Figure 8.6 for NaOsO_3 as well as for doped cases with G-AFM magnetic ordering. In NaOsO_3 there is a

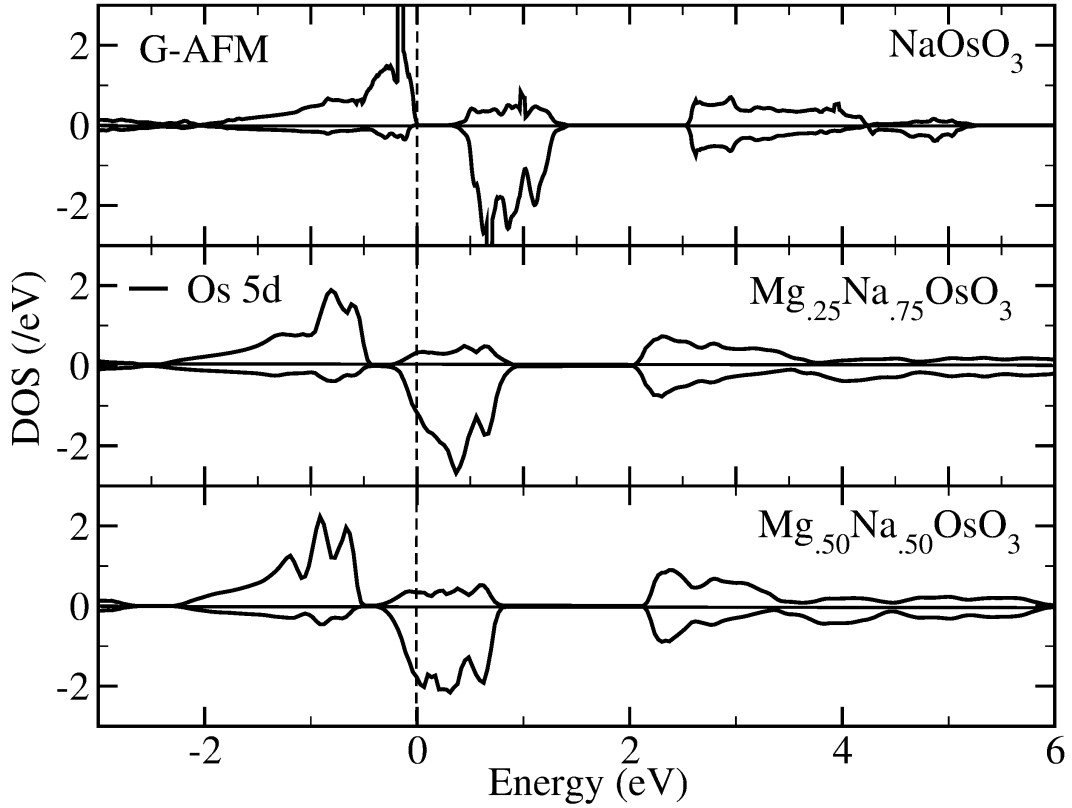


Figure 8.6: Os 5d orbital and spin projected DOS for NaOsO₃, Mg_{0.25}Na_{0.75}OsO₃ and Mg_{0.50}Na_{0.50}OsO₃. Fermi energy has been indicated with dashed line to clarify the rigid band shift with doping.

band gap in between t_{2g} majority and minority spin channels. A similar magnitude of the energy gap between the majority and minority spin t_{2g} states is found for the doped cases with all other aspects of the electronic structure remain the similar. Surprisingly, one finds an almost rigid band shift of the density of states in the doped system and the shift of the band enhances with the doping concentrations. This rigid band shift can be explained by considering increase in electron count with the increment in doping concentration. In NaOsO₃ Os ions are in $5d^3$ configuration corresponding to the complete filling of t_{2g} majority spin channels. Substitution of Na with bivalent Mg

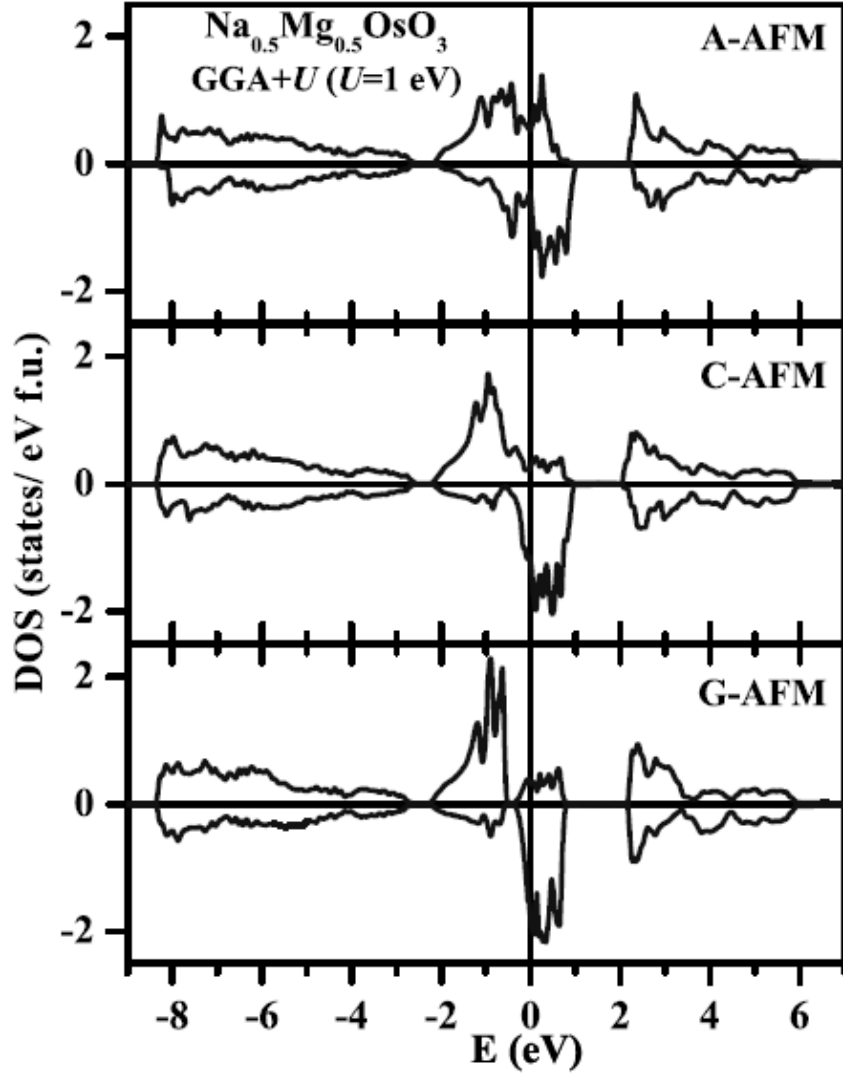


Figure 8.7: Os 5d orbital and spin projected DOS for $\text{Mg}_{0.50}\text{Na}_{0.50}\text{OsO}_3$ in various antiferromagnetic configurations.

leads to an extra electron per doping site. This electron now populates the Os 5d t_{2g} minority spin channels which was unoccupied earlier and we have a rare occurrence of an G-type AFM metallic state. Now with the increment in the doping concentrations, electronic filling in the t_{2g} bands also increases and one have Fermi level buried within the minority t_{2g} bands.

It is also noteworthy that while the t_{2g} bands show a large exchange splitting, the e_g states which are at higher energies show hardly any exchange splitting. This is because the intra-atomic exchange splitting in these systems is small and whatever exchange splitting one finds for the t_{2g} states, emerges from the super exchange interactions, primarily from nearest-neighbour Os atoms. This effect is even more evident in Figure 8.7 where we have plotted spin polarized Os d partial density of states for different AFM configurations (A-AFM, C-AFM, G-AFM) for 50% Mg doped NaOsO₃. In A-AFM all the in-plane magnetic neighbours are ferromagnetically aligned whereas out of plane neighbours are antiferromagnetically coupled. In C-AFM we have in-plane magnetic neighbours with AFM alignment, out of planes are ferromagnetically aligned and for G-AFM all neighbours are antiferromagnetically aligned. Thus the number of AFM neighbours increases from A-AFM to C-AFM and to G-AFM configurations. The exchange splitting is also found to increase with the number of AFM neighbours contributing to the super-exchange pathways. While there is no energy gap between the majority spin and the minority spin in t_{2g} states for both A-AFM and C-AFM configurations, a small gap exists for the G-AFM magnetic structure, again emerging from the same reason.

8.3.2 Magnetic Structure Analysis

Results shown in the Figure 8.5 compares the stabilization energy of different collinear magnetic configurations. The immediate question that arises is whether we have probed enough magnetic configurations as the doped system could have spin spiral configurations being favoured. We therefore have considered various spin spiral configurations characterized by the spin spiral vector \mathbf{q} and have plotted spin wave dispersion along various high symmetry

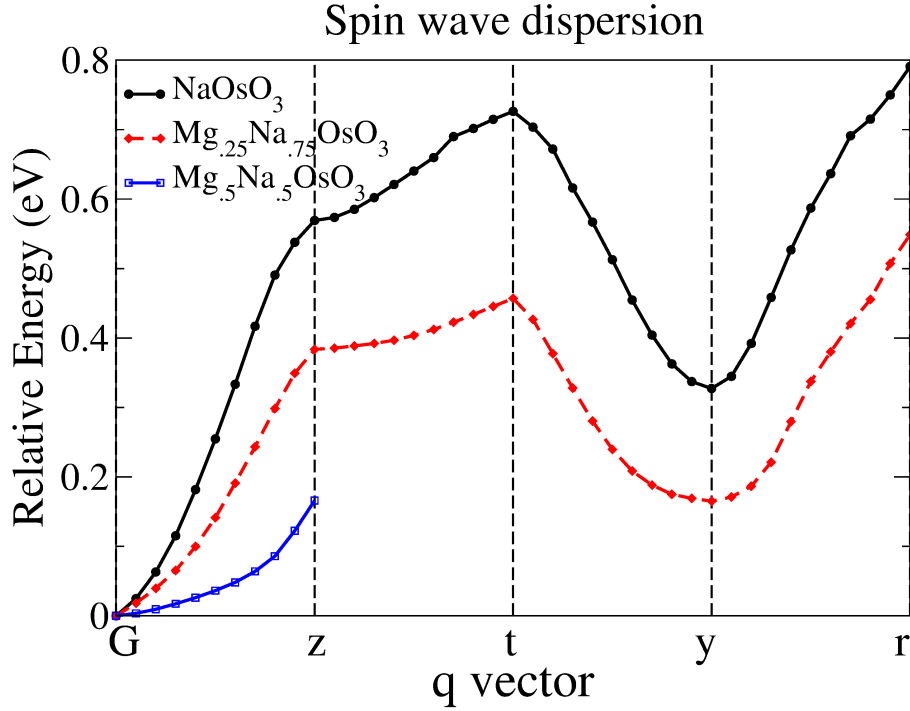


Figure 8.8: Spin wave dispersion of NaOsO₃, Mg_{0.25}Na_{0.75}OsO₃ and Mg_{0.50}Na_{0.50}OsO₃.

directions as shown in the Figure 8.8. The high symmetry points considered here are $\mathbf{G}(0.0,0.0,0.0)$, $\mathbf{z}(0.0,0.0,0.5)$, $\mathbf{t}(0.0,0.5,0.5)$, $\mathbf{y}(0.0,0.5,0.0)$ and $\mathbf{r}(0.5,0.5,0.5)$ where the coordinates are given in terms of reciprocal lattice vectors. Every \mathbf{q} corresponds to a definite magnetic configuration. As an example \mathbf{G} point corresponds to the G-type AFM configuration. Our calculations for Mg_{0.50}Na_{0.50}OsO₃ did not converge beyond \mathbf{z} and thus have not been shown in the figure. It is very evident from the dispersion that G-AFM is the ground state for all three structures reported though the stabilization energy reduces significantly with the enhancement of doping concentrations. Considering the \mathbf{z} point, we have stabilization energy of 574 meV for NaOsO₃ whereas it has reduced to 384 meV and 166 meV for Mg_{0.25}Na_{0.75}OsO₃ and Mg_{0.50}Na_{0.50}OsO₃ respectively.

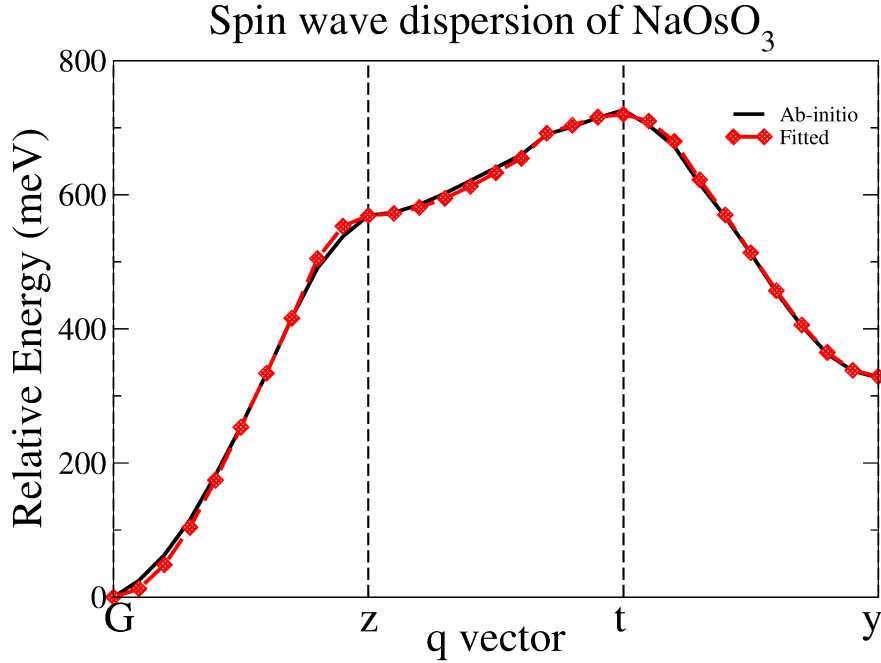


Figure 8.9: Spin wave dispersion of NaOsO₃ and results fitted with classical Heisenberg model.

We then have analyzed the spin wave dispersion of NaOsO₃ near the ground state G-AFM configurations by means of mapping our results onto a classical Heisenberg model with least number of parameters. Dispersion along **G-z-t-y** have been considered when extracting out the exchange parameters. Figure 8.9 shows the model energies fitted to our ab initio results. First four magnetic exchange interactions are given by J_1 , J_2 , J_3 and J_4 . In the left panel (a) of Figure 8.10, we have shown the nearest neighbour index and the corresponding exchange interaction parameters in a G-AFM structure. It is apparent from the figure that one should have AFM first and third neighbours whereas second and fourth neighbours are ferromagnetically coupled. We have extracted out different exchange parameters and have presented in Figure 8.10 (b). As one can see J_1 is found to be the most dominant and antiferromagnetic in nature. J_2 and J_3 are found to be predominantly negli-

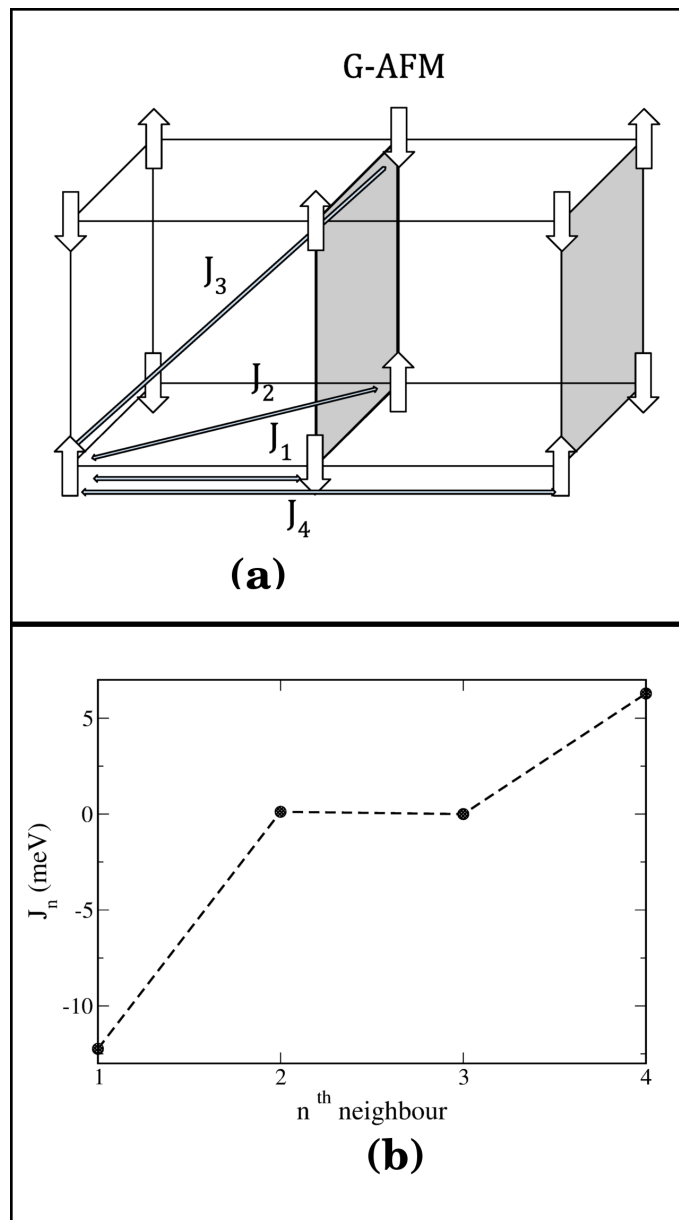


Figure 8.10: (a) Neighbours corresponding to first four exchange interaction terms. (b) Heisenberg exchange interaction parameters of NaOsO_3 as a function of nearest neighbours.

gible while J_4 between two ferromagnetically coupled spins are again found to be significant.

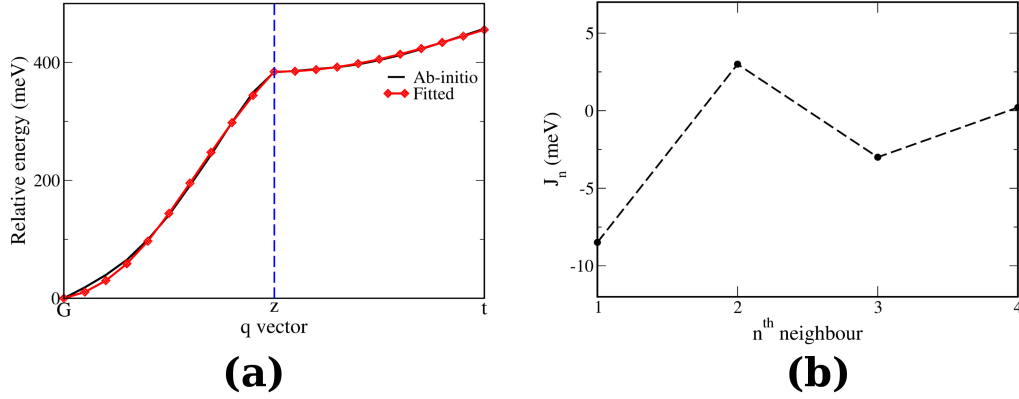


Figure 8.11: (a) Spin wave dispersion of $\text{Mg}_{0.25}\text{Na}_{0.75}\text{OsO}_3$ and results fitted with classical Heisenberg model. (b) Exchange interaction parameters of $\text{Mg}_{0.25}\text{Na}_{0.75}\text{OsO}_3$ as a function of nearest neighbours.

To understand the change in exchange pathways with doping concentrations, we have considered the case of $\text{Mg}_{0.25}\text{Na}_{0.75}\text{OsO}_3$ and extracted out the exchange parameters according to the method described above. Relatively smaller dispersion along **G-z-t** were considered as a subtle change in the magnetic moment were noticed beyond that, leading to a deviation from the Heisenberg model. Fitted dispersion spectrum is shown in the Figure 8.11 (a) along with the magnetic exchange interaction parameters shown in the panel (b). As it is reflected from the figure that there is a reduction in the strength of exchange parameters J_1 and J_4 . J_1 has reduced to -9 meV from the observed -12 meV in case of NaOsO_3 . J_4 is now negligibly small and can be considered as zero. Surprisingly one now have an enhancement of other two exchange parameters which were negligible prior to the doping. J_2 and J_3 are found to be 3 meV and -3meV respectively. To explain the enhancement and reduction of different exchange pathways, we have analyzed the orbital occupancy and the possible exchange mechanism involved in each case. It

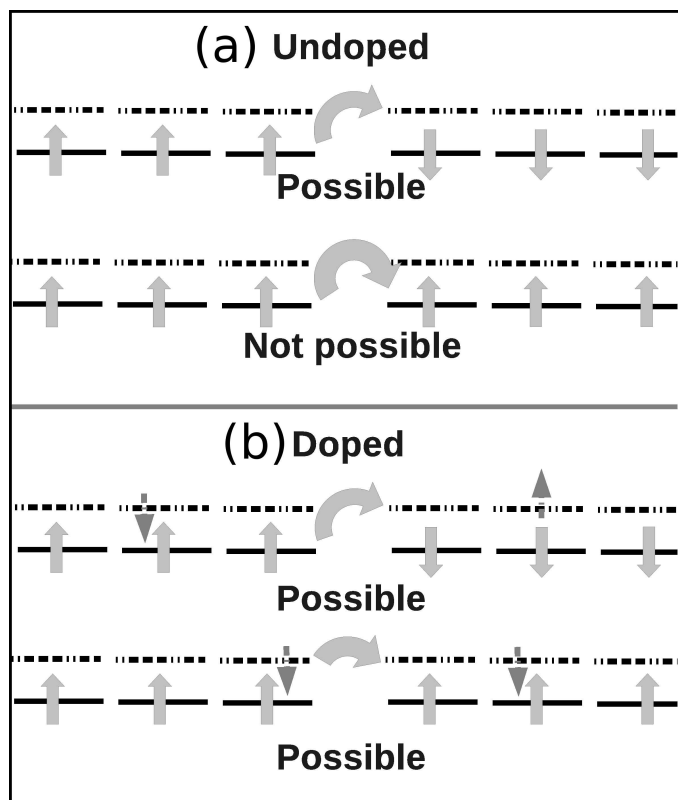


Figure 8.12: (a) Only AFM interaction possible in undoped NaOsO_3 whereas there are both FM and AFM component in (b) electron doped NaOsO_3 .

is noteworthy that the magnetic exchange interactions are via intermediate O ions and the only exchange mechanism to be operative is the super exchange. Now with doping one starts to populate minority spin channels with t_{2g} symmetry. This immediately opens up a minute ferromagnetic hopping channels between the first magnetic neighbours. Now an electron from the majority spin channel can hop to the partially occupied nearest neighbour minority channels and the effective first neighbour exchange interactions (J_1) which now can be assumed to be comprised of AFM and FM interactions reduces from its original value. The effect of electron doping on the J_1 has been shown in the Figure 8.12. This same mechanism of hopping between

majority and minority spin channels is again responsible for the modification of other exchange path-pathways that we have encountered.

8.4 Conclusion

In this chapter we have studied the electronic and magnetic structures of electron doped NaOsO_3 . NaOsO_3 is an example of Slater insulator characterized by the MIT at the Neel temperature. A slight electron doping turns the system to be metallic in nature but AFM ordering is found to be very robust irrespective of doping. We have analyzed the DOS and found a rigid evolution of the states with doping. Fermi energy in the doped system is contributed by the minority Os d states with t_{2g} symmetry. Magnetic structures have been analyzed with Heisenberg model and the effect of doping on different exchange pathways have been discussed.

Bibliography

- [1] M. Imada, A. Fujimori and Y. Tokura, Rev. Mod. Phys., **70**, 1039 (1998).
- [2] J. C. Slater, Phys. Rev., **82**, 538 (1951).
- [3] C. Weber, K. Haule and G. Kotliar, Nature Phys., **6**, 574 (2010).
- [4] W. J. Padilla, D. Mandrus and D. N. Basov, Phys. Rev. B, **66**, 035120 (2002).
- [5] R. Comin, G. Levy, B. Ludbrook, Z.-H. Zhu, C. N. Veenstra, J. A. Rosen, Yogesh Singh, P. Gegenwart, D. Stricker, J. N. Hancock, D. van der Marel, I. S. Elfimov, and A. Damascelli, Phys. Rev. Lett., **109**, 266406 (2012).
- [6] X. Liu, T. Berlijn, W.-G. Yin, W. Ku, A. Tsvelik, Young-June Kim, H. Gretarsson, Yogesh Singh, P. Gegenwart, and J. P. Hill, Phys. Rev. B, **83**, 220403 (2011).
- [7] Feng Ye, Songxue Chi, Huibo Cao, Bryan C. Chakoumakos, Jaime A. Fernandez-Baca, Radu Custelcean, T. F. Qi, O. B. Korneta, and G. Cao, Phys. Rev. B, **85**, 180403(R) (2012).
- [8] Hyun-Jung Kim, Jun-Ho Lee and Jun-Hyung Cho, Scientific Reports, **4**, 5253 (2014).

- [9] Y. G. Shi, Y. F. Guo, S. Yu, M. Arai, A. A. Belik, A. Sato, K. Yamaura, E. Takayama-Muromachi, H. F. Tian, H. X. Yang, J. Q. Li, T. Varga, J. F. Mitchell and S. Okamoto, *Phys. Rev. B(R)*, **80**, 161104 (2009).
- [10] S. Calder, V.O. Garlea, D.F. McMorrow, M.D. Lumsden, M.B. Stone, J.C. Lang, J.-W. Kim, J.A. Schlueter, Y.G. Shi, K. Yamaura, Y.S. Sun, Y. Tsujimoto and A.D. Christianson, *Phys. Rev. Lett.*, **108**, 257209 (2012).
- [11] Y.G.Shi, Y.F.Guo, S.Yu, M.Arai, A.A.Belik, A.Sato, K. Yamaura, E. Takayama-Muromachi, H. F. Tian, H. X. Yang, J.Q.Li, T.Varga, J.F.Mitchell and S.Okamoto, *Phys.Rev.B*, **80**, 161104 (2009).
- [12] Y. Du, X. Wan, L. Sheng, J. Dong and S. Y. Savrasov, *Phys.Rev. B*, **85**,174424 (2012).
- [13] M.-C. Jung, Y.-J. Song, K.-W. Lee, and W. E. Pickett, *Phys. Rev.B*, **87**, 115119 (2013).
- [14] S. Middey, S. Debnath, P. Mahadevan and D. D. Sarma, *Phys. Rev. B*, **89**, 134416 (2014).
- [15] G. Kresse and J. Furthmüller, *Phys. Rev. B*, **54**, 11169 (1996).
- [16] J. P. Perdew, K. Burke and M. Ernzerhof, *Phys. Rev. Lett.*, **77**, 3865 (1996).
- [17] S. L. Dudarev, G. A. Botton, S. Y. Savrasov, C. J. Humphreys, and A. P. Sutton, *Phys. Rev. B*, **57**, 1505 (1998).
- [18] H. J. Monkhorst and J. D. Pack, *Phys. Rev. B*, **13**, 5188 (1976).

List of Publications

1. The Role of Passivants on the Stoichiometry of CdSe and GaAs Nanocrystals, **S. Debnath**, R. Cherian, P. Mahadevan, The Journal of Physical Chemistry C, **117**, 21981 (2013).
2. NaOsO₃: A High Neel Temperature 5 d Oxide, S. Middey, **S. Debnath**, P. Mahadevan, D. D. Sarma, Physical Review B, **89** 134416 (2014).
3. Ultranarrow and Widely Tunable Mn²⁺ Induced Photoluminescence from Single Mn-Doped Nanocrystals of ZnS-CdS Alloys, A. Hazarika, A. Layek, S. De, A. Nag, **S. Debnath**, P. Mahadevan, A. Chowdhury and D. D. Sarma, Physical Review Letter, **110**, 267401 (2013).
4. Microscopic Model for the Strain-driven Direct to Indirect Band-gap Transition in Monolayer MoS₂ and ZnO, R. Das, B. Rakshit, **S. Debnath** and P. Mahadevan, Physical Review B, **89**, 115201 (2014).
5. Orbital Ordering Driven Magnetism in Fe Intercalated TaS₂, **S. Debnath**, P. Mahadevan, Communicated.
6. Ultrathin Films of CdS and the Polar Catastrophe Model, **S. Debnath**, P. Mahadevan and D. D. Sarma, Communicated.
7. Engineering Polar Distortion in SrTcO₃, **S. Debnath**, S. Bhattacharjee, B. Rakshit and P. Mahadevan, Under preparation.
8. Metallic Antiferromagnetic State in Mg Doped NaOsO₃, **S. Debnath**, P. Mahadevan, Under preparation.